DISSERTATION

DEVELOPMENTS IN LIGHTWAVE NANOELECTRONICS
(光波ナノエレクトロニクス)

ULTRAFAST SUB-CYCLE MANIPULATION OF ELECTRON TUNNELING IN METALLIC NANOSTRUCTURES
(金属ナノ構造体における電子トンネリングの超高速サブサイクル操作)

KATSUMASA YOSHIOKA

March, 2019

ADVISOR
PROFESSOR JUN TAKEDA

DEPARTMENT OF PHYSICS, ELECTRICAL AND COMPUTER ENGINEERING
YOKOHAMA NATIONAL UNIVERSITY

Abstract

Smaller and faster are the key requirements for the progress of modern nanoscience and nanotechnology. Indeed, modern information technology has advanced by finding ways to precisely control electrons on faster time scales and finer spatial scales. However, further advances will be difficult to achieve by means of conventional nanoelectronics. Therefore, the creation of a new platform for the ultrafast control of electrons on a nanoscale is indispensable. In this thesis, a comprehensive study of ultrafast sub-cycle manipulation of electron tunneling in metallic nanostructures is presented. Phase-controlled single-cycle intense THz pulses are used to drive real-space electron tunneling in metallic nanogap structures, paving the way for the development of "lightwave nanoelectronics".

First, the thesis investigates the possibility of lightwave driven electron tunneling using THz time-domain spectroscopy in an ultrathin gold (Au) film with randomly distributed nanogap structures. Both isolated and percolated Au nanostructures were fabricated on a Si substrate. By increasing the incident THz electric field strength, large opacity in the THz transmission takes place in the percolated nanostructures. We reveal that this nonlinear response is due to a nonthermal and nonlinear increase in conductivity of ultrathin Au films induced by field-driven electron tunneling.

Second, in order to better understand the THz-field-induced electron tunneling process, we developed a new technique called phase-controlled THz scanning tunneling microscopy (THz-STM). In particular, we demonstrated the direction of the electron tunneling between a metal nanotip and a sample can be coherently manipulated by tuning the carrier-envelope phase (CEP) of the incident THz electric fields through the Gouy phase shift. The field enhancement factor – approximately 100,000 – at the nanogap between the nanotip and sample was considerable. Furthermore, this spatially confined THz electric field in the tunnel junction enables nanoscale imaging of the Au nanostructures beyond the diffraction limit.

Finally, the thesis describes how the perfect CEP-controlled THz pulses and

dual-phase double-pulse scheme we developed is used for in-situ tailoring and reconstruction of THz near-fields formed at the tunnel junction. Measurements of the phase-resolved sub-cycle electron tunneling revealed an unexpected large CEP shift between far-field and near-field. We found that the phase shift stems from the wavelength-scale feature of the tip–sample configuration. By using a dual-phase double-pulse scheme, the electron tunneling was coherently manipulated over the femtosecond time scale. Our phase-controlled THz-STM with desirable near-fields will offer unprecedented control of electrons for ultrafast atomic-scale electronics and metrology.

Acknowledgement

First of all, I would like to express my greatest gratitude to my supervisor, Prof. Jun Takeda, for giving me the opportunity to join his team and perform my Ph.D. study. I am grateful for his widespread scientific knowledge and encouragement for pursuing what I was interested in. I sincerely thank him for the trust, the creative freedom and the high degree of independence he gave me. He was also very patient in improving my writing skills and teaching me physics, no matter how busy he was.

Second, I would like to thank my co-supervisor, Associate Prof. Ikufumi Katayama for his continuous support and many insightful physical discussions. His advice based on his outstanding broad viewpoint has led me to present many of the concepts proposed in this thesis.

I gratefully appreciate the academic staff for their overall support of my work. Dr. Yasuo Minami, worked as an Assistant Professor at the laboratory and now become an Associate Professor at Tokushima University, helped me in constructing the experimental setup. I learned from him how to operate the femtosecond laser system. Dr. Yusuke Arashida, worked as an Assistant Professor at the laboratory and now become an Assistant Professor at the University of Tsukuba, gave me a boost through daily discussions. I profited greatly from his great insights and understanding of physics. I would like to thank Dr. Masahiro Kitajima, Visiting Professor at the laboratory, for many helpful discussions and advice. In particular, he encouraged me to combine the ultrafast THz spectroscopy and the Scanning tunneling microscopy.

Let me express my gratitude to many people outside the laboratory. Associate Prof. Ken-ichi Shudo was kind enough to help me for fabricating Au nanostructures. I wish to thank Dr. Tadaaki Nagao and Dr. Thang Duy Dao at National Institute for Material Science for insightful discussions and teaching me the sample preparation techniques. I am grateful to Prof. Hidemi Shigekawa and Associate Prof. Shoji Yoshida at the University of Tsukuba for their great help for jumping into a new research area of surface science. Surprisingly, they decided to lend me a whole STM setup! The THz-STM

Contents

Chapter 1

Introduction and background

1.1   Modern information technology

The development of modern information technology has been accelerated by the ability to precisely control electrons on a faster time scale and a finer spatial scale. According to Moore's law, the prediction that has powered the revolution of information technology since the 1960s, the number of transistors in a microprocessor chip and resulting chip's performance will double every 2 years or so [1,2]. With the exponential improvement based on this guiding principle, nanofabrication technologies currently enable manufacturing of top-of-the-line microprocessors with circuit features around 10 nanometers. However, the semiconductor industry will soon abandon the pursuit of Moore's low because of the fundamental limitation on the size of integrated nanocircuits; the local heat problem and unintentional quantum behavior will appear when the semiconductor circuitry is jammed into the nanoscale area [3]. On the other hand, the clock speed of a microprocessor – the time it takes to switch on and off electrons in the circuit – is limited to the gigahertz frequency range (sub-nanosecond on a temporal scale) by means of conventional electronics. Therefore, the creation of a new technique for the ultrafast control of electrons on a nanoscale is indispensable, in addition to current technologies based on semiconductor physics.

1.2 Developments in ultrafast laser technology

A promising strategy for overcoming the limitations of conventional electronics described above is to utilize the fastest oscillating electromagnetic field in nature − the carrier wave of light. This fascinating concept, called "lightwave electronics" [4], has attracted considerable attention over the decades in the field of photonics.

Since the first laser was invented in 1960 [5], we have explored the new opportunities provided by this stable electromagnetic source that has perfect coherency in both space and time. In addition to the use of laser technology for real-life applications such as sensing, projecting, printing, recording, manipulating, and processing in diverse fields, scientists have pushed the boundaries of laser technology in order to generate highly intense and ultrashort laser pulses. Thanks to the invention of key technologies such as Q-switching [6], mode-locking [7], and chirp pulse amplification [8] techniques, it is possible, with a tabletop system in the laboratory, to generate laser pulses with femtosecond (1 fs = $1 \cdot 10^{-15}$ s) pulse duration and terawatt peak power. Using these ultrashort laser pulses, elementary dynamics of matter can be directly traced in the time domain to reveal and control its fundamental properties.

However, in conventional optical pump-probe spectroscopy, only cycle-averaged information such as intensity and frequency spectrum can be obtained, thus making it difficult to investigate interactions between the electric field of ultrashort laser pulses (the carrier wave of light) and electrons in matter. The reason is that the phase of ultrashort laser pulses differ from pulse to pulse due to the instability of the laser cavity. Despite the fact that Keldysh predicted strong laser-field induced tunneling ionization in atoms and solids in his seminal theoretical paper in 1965 [9], it took more than 30 years to develop a sufficiently sophisticated technique to trying out his framework. This technique, the generation of a phase-locked intense ultrashort laser field, was made possible by the development of the optical frequency comb [10], for which the Nobel prize in physics was awarded in 2005.

1.3 Lightwave electronics in gas and bulk solid state systems

Strong-field interactions of light with electrons in matter are governed by both quantum-mechanical and classical concepts: in the quantum regime, electrons experience light as photons; in the classical regime, however, electrons are driven by the optical field. These two possibilities are illustrated schematically in Figure 1.1.

Keldysh characterized the transition between the photon-driven regime and the field-driven regime using a simple equation, by introducing the ratio between the ionization potential I_P and the ponderomotive energy U_P [9]:

a Mutiphoton ionization ($\gamma > 1$)

b Tunnel ionization ($\gamma < 1$)

c photon-driven regime

d field-driven regime
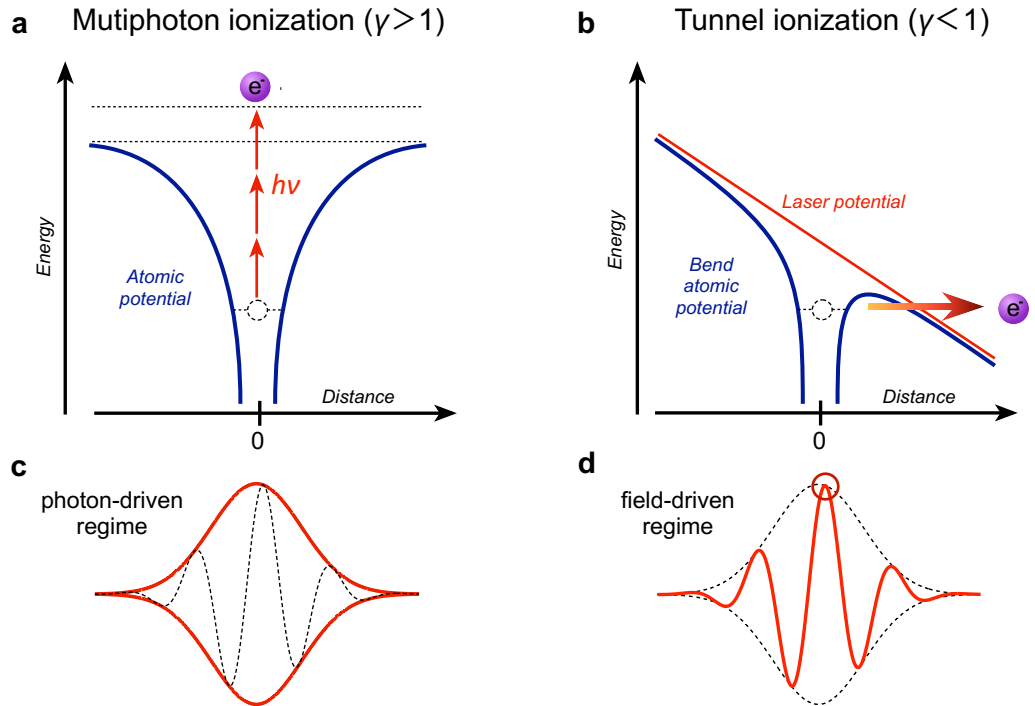
Figure 1.1 | Schematic of strong-field interaction in atomic potential. Two limiting cases for ionization, depending on the Keldysh parameter γ [9]. **(a)** In the case of $\gamma > 1$, photon-driven multiphoton ionization occurs, which is sensitive to the light intensity as highlighted by the red curve in (c). **(b)** In the case of $\gamma < 1$, field-driven tunnel ionization occurs, which is sensitive to the light field as highlighted by the red curve in **(d)**. In the latter case, ionization dominates at the peak of the laser field; thus the electron trajectory is highly sensitive to the optical phase (carrier-envelope phase).

$$\gamma = \sqrt{\frac{I_P}{2U_P}} = \frac{\omega\sqrt{2mI_P}}{eF}, \qquad (1.1)$$

where ω is the optical driving frequency, m is the mass of the electron, e is the electron charge, and F is the electric field. In order to precisely control electron trajectory at an ultrafast time scale using the light field ($\gamma < 1$), the driving laser pulse has to be sufficiently low frequency and/or highly intense.

Experimentally, the lightwave-driven phenomenon was first demonstrated in the tunnel ionization of Xe atoms using a CO_2 laser field [11]. The lightwave-driven transport of electrons was then extensively studied in atomic and molecular systems using intense few-cycle phase-controlled laser pulses, and has now become a versatile tool for the investigation of electron wave function with unprecedented time-resolution, notably high-order harmonic generation (HHG) – the conversion of near-infrared (NIR) or mid-infrared (MIR) field into extreme ultraviolet radiation (XUV) lasting less than 1 fs [12]. This peculiar observation can be explained by the lightwave-driven coherent motion of electrons resulting from light-field-induced tunnel ionization, excursion of the quasi-free electrons, and their recollision with the ion core. The emitted broadband radiation carries key information within its spectrum about the processes within and the structure of the target system. Furthermore, the use of a waveform-controlled laser pulse allows the creation of bursts of isolated attosecond (1 as = $1 \cdot 10^{-18}$ s) pulses which paves the way for the development of attosecond science [13–16].

Despite the successes achieved in the application of a strong laser-field to materials in the gas phase, this fascinating concept has only recently been applied to condensed matter systems, and the exploration of lightwave electronics in the development of next-generation ultrafast solid-state devices has just begun. In 2011, HHG was also realized in a solid state system with the harmonic spectra extending well beyond the bandgap [17]. Although the underlying mechanism is still under debate [18,19], a detailed understanding of the HHG process is expected to lead to the development of new spectroscopic techniques, such as all-optical reconstruction of crystal band structure [20].

A further important step towards ultrafast signal processing was reported very recently using amorphous silicon dioxide [21], where light-field-driven electron transport in the insulator was detected as electrical current using metallic electrodes. Because nonlinear polarization is induced by an adiabatic

process via interband Landau-Zener tunneling [22,23], electrical currents can be driven and switched by the instantaneous light field which may open up a new avenue for petahertz (1 PHz = $1 \cdot 10^{15}$ hertz) electronics.

This light-field-driven electrical current has also proved to be useful in semiconductors (gallium nitride [24]) and conductors (graphene [25]). This is especially true in graphene, where the light-field-driven regime can be achieved with modest field strength, owing to the peculiar characteristics of the Dirac-cone, which renders complex amplified laser systems dispensable [25]. In addition, because of laser-polarization-dependent behavior of electrons due to quantum interference during multiple Zener tunneling, transistor operation at optical clock rates may become feasible [25].

1.4 Lightwave electronics in nanoplasmonic systems

Recall that not only a faster time-scale but also a finer spatial-scale is crucial for the evolution of modern signal processing. However, the spot size of a focused laser beam is limited to the diffraction limit of the lightwave (hundreds of nanometers in optical frequency), and is therefore unable to achieve the desired nanoscale resolution. One way to overcome this major challenge is to use plasmonics, a rapidly developing field at the boundary of condensed matter physics and photonics. By tailoring plasmons—collective oscillations of the free electron gas—in metallic nanostructures, highly localized near-fields can be produced by concentrating laser pulses into dimensions far beyond the diffraction limit of the incident light. Indeed, strong-field photoemission has been realized in metallic nanoparticles [26] and nanotips [27–32].

In addition to the observation of absolute phase (carrier-envelope phase) effect and control in electron dynamics [27,29] (Figure 1.2a, b), a new effect – the nano-localized near-field – has been discovered, in which, owing to the nanoplasmonic field strongly localized at the nanotip apex, the photoemitted electrons can escape from near-field within a fraction of an optical half-cycle, thus effectively accelerating electrons [28], as illustrated in Figure 1.2c, d. Furthermore, as shown in Figure 1.2e, f, near-fields at the nanotip apex were successfully visualized by measuring photoelectron energy spectra using streaking spectroscopy [31,32].
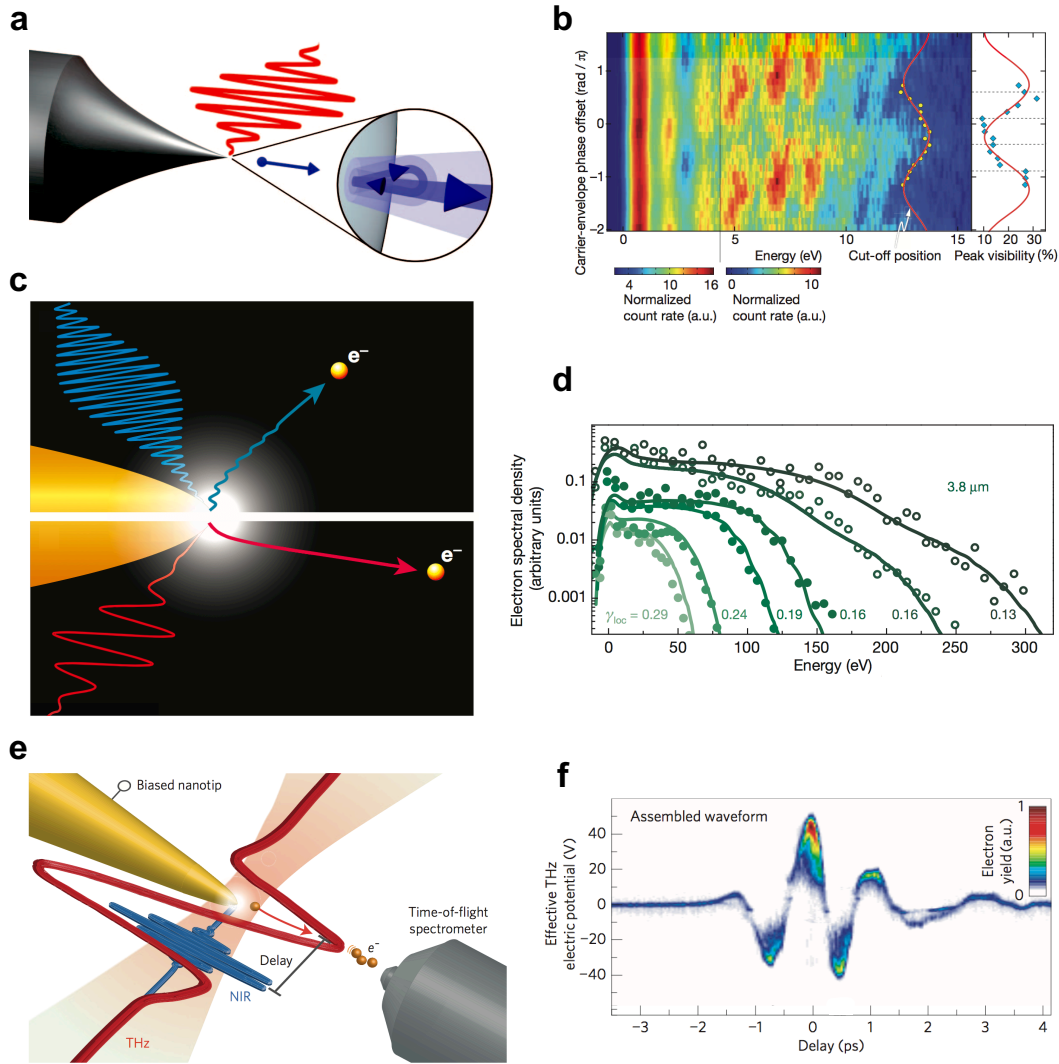
Figure 1.2 | Lightwave control of electrons in the metallic nanotip. (a)
Attosecond motion of electron emission is controlled by a carrier-envelope
phase (CEP) controlled few-cycle laser electric field. **(b)** The resulting
CEP-dependent photoelectron energy spectra manifest sub-cycle
interference of electron wave-packet at the tip apex. **(a)** and **(b)** are
adopted from ref [27]. **(c)** Trajectories of light-field-driven photoemission.
A quiver motion of the electron is suppressed in the long-wavelength
excitation. **(d)** Experimental (circle) and simulated (solid lines)
photoelectron energy spectra. Good agreement was obtained by taking
near-field decay at the tip apex into account. **(c)** and **(d)** are adopted from
ref [28]. **(e)** The photoemitted electrons initiated by a NIR pulse were
accelerated by a near-field of THz electric field with different time delays.
(f) THz near-field waveform derived from a streaking spectrogram. **(e)** and
(f) are adopted from ref [31].

1.5 Overview of motivation and results

The combination of intense ultrashort laser pulses and a metallic nanotip provides a new platform for strong-field physics. Furthermore, the excellent spatial and temporal coherence of locally accelerated photoelectrons is expected to provide a new source of ultrashort electron pulses. However, the role of the laser field employed in these studies [27–32] was limited to inducing photoemission and subsequent acceleration, because of its geometry. Therefore, developing the concept of "lightwave nanoelectronics" for a new nanoplasmonic platform will be highly beneficial for the advancement of next-generation devices by overcoming the limitations in both space and time of conventional signal processing. To this end, we focused on a tunnel junction – a quantum structure formed by placing two metal electrodes separated by a thin insulator – as the new platform. Using the tunnel junction, ultrafast currents can be controlled at even smaller scales. Furthermore, a range of functionality is expected to be realized on the nanoscale circuit, such as large field enhancement [33,34], optical rectification [33,35], and transistor operation [34,36].

In order to exploit the carrier wave of intense laser pulses in the tunnel junction, several requirements are imposed on the laser profile:

1. The electric field waveform has to be well-defined and reproducible, otherwise the light-field-driven effect will be smeared out by cycle averaging.
2. The number of cycles contained in a laser pulse should be minimized, in order to efficiently drive electrons due to the symmetry-breaking of the system.
3. The photon energy of the laser pulses has to be kept sufficiently low, in order to suppress thermal expansion and avoid permanent damage to the nanoscale metallic structures.

Fortunately, these requirements can be perfectly fulfilled using intense terahertz (1 THz = $1 \cdot 10^{12}$ hertz) pulses. In the THz spectral range, the so-called THz gap has long existed [37] because of the absence of powerful emitters and sensitive detectors. Nowadays, thanks to the advancement of novel efficient emitters [38–41], phase-locked intense single-cycle THz electric fields can be generated and detected with absolute resolution of amplitude and

phase [42–45]. Moreover, the low photon energy of a THz pulse permits the acceleration of electrons in the non-perturbative regime without heating the system with excess energy.

Exploiting these advantages, THz-field-induced nonlinear phenomena have been demonstrated in a variety of systems, such as anharmonic drive of ferroelectric soft mode of a quantum paraelectric thin film [46], orientation and alignment of molecules [47], impact ionization and Zener tunneling in semiconductors [48–50], THz-field-induced phase transition in strongly correlated electronic systems [51], and driving the Higgs mode in superconductors [52,53]. However, very few studies have been devoted to metallic systems.

In this thesis, a comprehensive study of ultrafast sub-cycle manipulation of electron tunneling in metallic nanostructures is presented. Phase-controlled single-cycle intense THz pulses are used to drive real-space electron tunneling
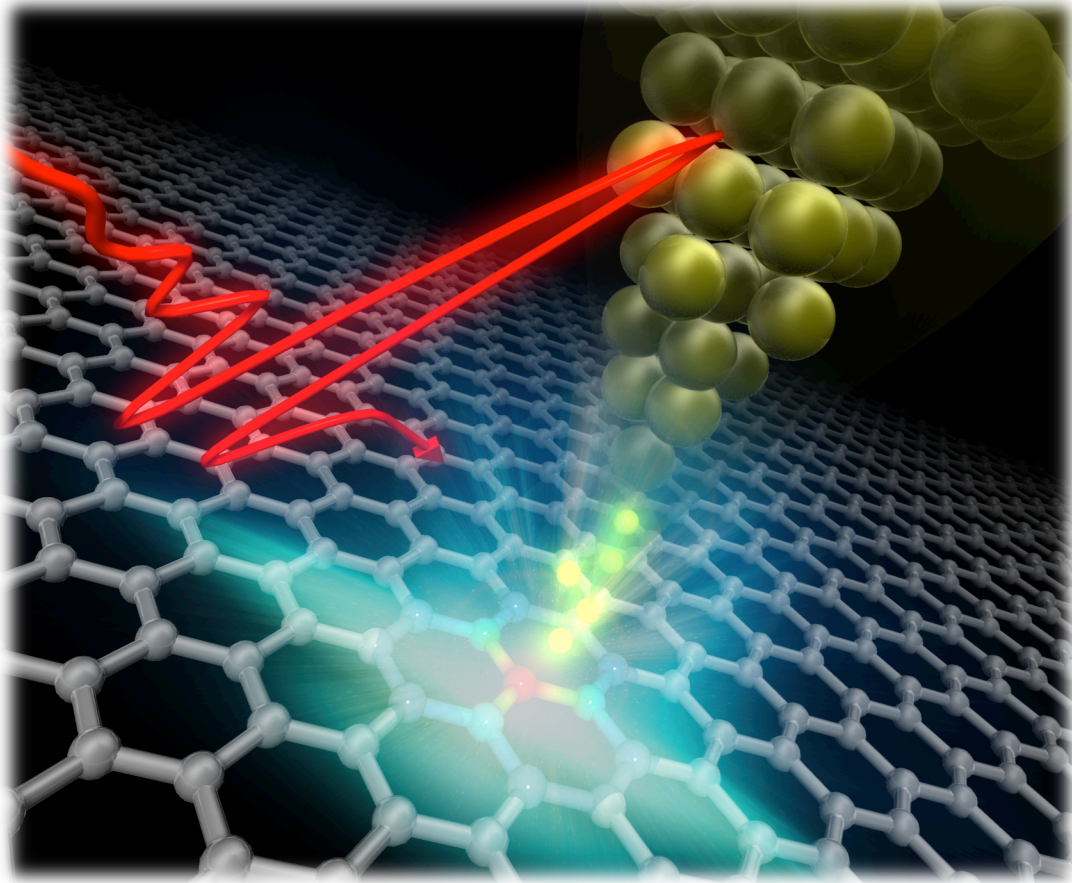
Figure 1.3 | Illustration of THz-field-driven electron tunneling in a single tunnel junction of the scanning tunneling microscope.

in metallic nanogap structures. We investigate the possibility of lightwave-driven electron tunneling using THz time-domain spectroscopy (THz-TDS) in an ultrathin gold (Au) film with random nanogap structures. By analyzing transmitted waveforms obtained using electro-optic sampling, we reveal nonthermal and nonlinear increase in the conductivity of an ultrathin Au films induced by field-driven electron tunneling. In order to directly detect THz-field-induced electron tunneling, we developed a novel technique called phase-controlled THz scanning tunneling microscopy (THz-STM [54]) (Figure 1.3). This has allowed us to understand the detailed mechanisms of electron tunneling as well as the ultrafast sub-cycle coherent control of electrons and nanoscale imaging. Furthermore, the development of tunable-phase THz pulses and dual-phase double-pulse schemes enables in-situ tailoring and reconstruction of THz near-fields formed at a tunnel junction. Our results show that the combination of single-cycle THz electric field and a tunnel junction achieves sub-picosecond coherent control of electrons with nanometer spatial resolution which surpasses what can be achieved with current information technology. We believe that the concept of "lightwave nanoelectronics" presented in this thesis, providing access to an unprecedented ultrafast and ultrasmall regime, paves the way for the development of next-generation ultrafast atomic-scale electronics and metrology.

Outline of this thesis

Chapter 2 first describes the properties of an ultrashort laser pulse, which is an essential tool for lightwave control of electrons. We then describe experimental methods for the generation and detection of phase-locked intense single-cycle THz pulses using an amplified femtosecond laser source. Based on this light source, we describe the calculation of optical constants for a sample, and control of the CEP of THz pulses through the Gouy phase shift and the CEP shifter. Finally, the principle and concept of STM are briefly introduced.

  Chapter 3 describes how we performed THz-TDS on an ultrathin Au film with random nanogap structures in order to investigate the interaction between high intensity THz pulses and metallic nanogap structures. Electrons in the percolated Au nanostructures (in the vicinity of the insulator-to-metal transition) are accelerated by the intense THz electric field, causing real-space tunneling of electrons. Therefore, the nonlinear increase in conductivity of the Au film can be controlled in sub-picosecond timescale without undesirable

thermal effects. The content of this chapter has been published as "Terahertz-field-induced nonlinear electron delocalization in Au nanostructures" [55].

In Chapter 4, in order to clarify the detailed mechanisms of THz-field-induced electron tunneling, we describe how we combined a scanning tunneling microscope and a phase-controlled single-cycle THz pulse, enabling the measurement of electron tunneling in a well-defined single tunnel junction. The motion of electrons in a tunnel junction was coherently controlled either from a nanotip to a sample or vice versa. Spatially confined huge THz electric fields strongly modulate the potential barrier at a nanogap and can steer a large number of electrons in an extremely nonlinear regime. Furthermore, nanoscale imaging of an Au nanostructure was demonstrated, which is far beyond the diffraction limit of THz pulses. The content of this chapter has been published as "Real-space coherent manipulation of electrons in a single tunnel junction by single-cycle terahertz electric fields" and "Nanoscale electron manipulation in metals with intense THz electric fields" [56,57].

In Chapter 5, we describe the development of a new single-cycle THz pulse, whose absolute phase can be controlled to a desired value, and the measurement of the sub-cycle response of electron tunneling in order to investigate the interactions between a broadband THz electric field and a tunnel junction. Phase-resolved measurements revealed an unexpected large phase shift between incident far-field and near-field single-cycle THz waveforms. With the aid of a finite integration simulation, we found that the resulting near-field and subsequent electron tunneling strongly depend on the wavelength-scale features of the nanotip because of the plasmonic response of the particular nanotip. Furthermore, by tailoring the single-cycle near-field with a dual-phase double-pulse scheme, electron tunneling was coherently manipulated and detected over the femtosecond time scale. The content of this chapter has been published as "Tailoring single-cycle near field in a tunnel junction with carrier-envelope phase-controlled terahertz electric fields" [58].

Finally, in Chapter 6, we summarize the results described in this thesis, and describe the opportunities and developments that can be expected in the future.

References in chapter 1

[1]   G.E. Moore, Cramming more components onto integrated circuits, Electronics. 38 (1965) 114-116.

[2]   G.E. Moore, Progress In Digital Integrated Electronics, IEDM Tech. Dig. 21 (1975) 11–13.

[3]   M.M. Waldrop, The chips are down for Moore's law, Nature. 530 (2016) 144–147.

[4]   E. Goulielmakis, V.S. Yakovlev, A.L. Cavalieri, M. Uiberacker, V. Pervak, A. Apolonski, R. Kienberger, U. Kleineberg, F. Krausz, Attosecond Control and Measurement: Lightwave Electronics, Science. 317 (2007) 769–775.

[5]   T.H. MAIMAN, Stimulated Optical Radiation in Ruby, Nature. 187 (1960) 493–494.

[6]   F.J. McClung, R.W. Hellwarth, Giant Optical Pulsations from Ruby, J. Appl. Phys. 33 (1962) 828–829.

[7]   L.E. Hargrove, R.L. Fork, M.A. Pollack, Locking of He-Ne Laser Modes Induced by Synchronous Intracavity Modulation, Appl. Phys. Lett. 5 (1964) 4–5.

[8]   D. Strickland, G. Mourou, Compression of amplified chirped optical pulses, Opt. Commun. 56 (1985) 219–221.

[9]   L. V. Keldysh, Ionization in the field of a strong electromagnetic wave, J. Exp. Theor. Phys. 20 (1965) 1307–1314.

[10]   T. Udem, R. Holzwarth, T.W. Hänsch, Optical frequency metrology, Nature. 416 (2002) 233–237.

[11]   S.L. Chin, F. Yergeau, P. Lavigne, Tunnel ionisation of Xe in an ultra-intense CO 2 laser field (10^{14} W cm^{-2}) with multiple charge creation, J. Phys. B At. Mol. Phys. 18 (1985) L213–L215.

[12]   M. Hentschel, R. Kienberger, C. Spielmann, G.A. Reider, N. Milosevic, T. Brabec, P. Corkum, U. Heinzmann, M. Drescher, F. Krausz, Attosecond metrology., Nature. 414 (2001) 509–513.

[13]   P.B. Corkum, F. Krausz, Attosecond science, Nat. Phys. 3 (2007) 381–387.

[14] F. Krausz, M. Ivanov, Attosecond physics, Rev. Mod. Phys. 81 (2009)

[15] F. Krausz, M.I. Stockman, Attosecond metrology: from electron capture to future signal processing, Nat. Photonics. 8 (2014) 205–213.

[16] S.Y. Kruchinin, F. Krausz, V.S. Yakovlev, Strong-field Phenomena in Periodic Systems, Rev. Mod. Phys. 90 (2017) 21002.

[17] S. Ghimire, A.D. Dichiara, E. Sistrunk, P. Agostini, L.F. Dimauro, D.A. Reis, Observation of high-order harmonic generation in a bulk crystal, Nat. Phys. 7 (2011) 138–141.

[18] S. Ghimire, G. Ndabashimiye, A.D. DiChiara, E. Sistrunk, M.I. Stockman, P. Agostini, L.F. DiMauro, D.A. Reis, Strong-field and attosecond physics in solids, J. Phys. B At. Mol. Opt. Phys. 47 (2014) 204030.

[19] T. Higuchi, M.I. Stockman, P. Hommelhoff, Strong-Field Perspective on High-Harmonic Radiation from Bulk Solids, Phys. Rev. Lett. 113 (2014) 213901.

[20] G. Vampa, T.J. Hammond, N. Thiré, B.E. Schmidt, F. Légaré, C.R. McDonald, T. Brabec, D.D. Klug, P.B. Corkum, All-Optical Reconstruction of Crystal Band Structure, Phys. Rev. Lett. 115 (2015) 1–5.

[21] A. Schiffrin, T. Paasch-Colberg, N. Karpowicz, V. Apalkov, D. Gerster, S. Mühlbrandt, M. Korbman, J. Reichert, M. Schultze, S. Holzner, J. V Barth, R. Kienberger, R. Ernstorfer, V.S. Yakovlev, M.I. Stockman, F. Krausz, Optical-field-induced current in dielectrics, Nature. 493 (2012) 70–74.

[22] L. D. Landau, Zur Theorie der Energieübertragung. II, Phys. Zeitschrift Der Sowjetunion. 2 (1932) 46–51.

[23] C. Zener, A Theory of the Electrical Breakdown of Solid Dielectrics, Proc. R. Soc. A Math. Phys. Eng. Sci. 145 (1934) 523–529.

[24] T. Paasch-Colberg, S.Y. Kruchinin, Ö. Sağlam, S. Kapser, S. Cabrini, S. Muehlbrandt, J. Reichert, J.V. Barth, R. Ernstorfer, R. Kienberger, V.S. Yakovlev, N. Karpowicz, A. Schiffrin, Sub-cycle optical control of current in a semiconductor: from the multiphoton to the tunneling regime, Optica. 3 (2016) 1358.

[25] T. Higuchi, C. Heide, K. Ullmann, H.B. Weber, P. Hommelhoff, Light-field-driven currents in graphene, Nature. 550 (2017) 224–228.

[26] P. Dombi, A. Hörl, P. Rácz, I. Márton, A. Trügler, J.R. Krenn, U. Hohenester, Ultrafast strong-field photoemission from plasmonic nanoparticles, Nano Lett. 13 (2013) 674–678.

[27] M. Krüger, M. Schenk, P. Hommelhoff, Attosecond control of electrons emitted from a nanoscale metal tip., Nature. 475 (2011) 78–81.

[28] G. Herink, D.R. Solli, M. Gulde, C. Ropers, Field-driven photoemission from nanostructures quenches the quiver motion., Nature. 483 (2012) 190–3.

[29] B. Piglosiewicz, S. Schmidt, D.J. Park, J. Vogelsang, P. Groß, C. Manzoni, P. Farinello, G. Cerullo, C. Lienau, Carrier-envelope phase effects on the strong-field photoemission of electrons from metallic nanostructures, Nat. Photonics. 8 (2014) 37–42.

[30] G. Herink, L. Wimmer, C. Ropers, Field emission at terahertz frequencies: AC-tunneling and ultrafast carrier dynamics, New J. Phys. 16 (2014) 123005.

[31] L. Wimmer, G. Herink, D.R. Solli, S. V. Yalunin, K.E. Echternkamp, C. Ropers, Terahertz control of nanotip photoemission, Nat. Phys. 10 (2014) 432–436.

[32] B. Förg, J. Schötz, F. Süßmann, M. Förster, M. Krüger, B. Ahn, W.A. Okell, K. Wintersperger, S. Zherebtsov, A. Guggenmos, V. Pervak, A. Kessel, S.A. Trushin, A.M. Azzeer, M.I. Stockman, D. Kim, F. Krausz, P. Hommelhoff, M.F. Kling, Attosecond nanoscale near-field sampling, Nat. Commun. 7 (2016) 11717.

[33] D.R. Ward, F. Hüser, F. Pauly, J.C. Cuevas, D. Natelson, Optical rectification and field enhancement in a plasmonic nanogap, Nat. Nanotechnol. 5 (2010) 732–736.

[34] K. Yoshida, K. Shibata, K. Hirakawa, Terahertz Field Enhancement and Photon-Assisted Tunneling in Single-Molecule Transistors, Phys. Rev. Lett. 115 (2015) 138302.

[35] A. Sharma, V. Singh, T.L. Bougher, B.A. Cola, A carbon nanotube optical rectenna., Nat. Nanotechnol. 10 (2015) 1027–1032.

[36] R. Vincent, S. Klyatskaya, M. Ruben, W. Wernsdorfer, F. Balestro, Electronic read-out of a single nuclear spin using a molecular spin transistor., Nature. 488 (2012) 357–60.

[37] M. Tonouchi, Cutting-edge terahertz technology, Nat. Photonics. 1 (2007) 97–105.

[38] T. Bartel, P. Gaal, K. Reimann, M. Woerner, T. Elsaesser, Generation of single-cycle THz transients with high electric-field amplitudes, Opt. Lett. 30 (2005) 2805.

[39] K.L. Yeh, M.C. Hoffmann, J. Hebling, K.A. Nelson, Generation of 10 μJ ultrashort terahertz pulses by optical rectification, Appl. Phys. Lett. 90 (2007).

[40] F. Junginger, A. Sell, O. Schubert, B. Mayer, D. Brida, M. Marangoni, G. Cerullo, A. Leitenstorfer, R. Huber, Single-cycle multiterahertz transients with peak fields above 10 MV/cm., Opt. Lett. 35 (2010) 2645–7.

[41] C.P. Hauri, C. Ruchert, C. Vicario, F. Ardana, Strong-field single-cycle THz pulses generated in an organic crystal, Appl. Phys. Lett. 99 (2011) 161116.

[42] Q. Wu, X.C. Zhang, Free-space electro-optic sampling of terahertz beams, Appl. Phys. Lett. 67 (1995) 3523.

[43] C. Kübler, R. Huber, S. Tübel, A. Leitenstorfer, Ultrabroadband detection of multi-terahertz field transients with GaSe electro-optic sensors: Approaching the near infrared, Appl. Phys. Lett. 85 (2004) 3360–3362.

[44] J. Dai, X. Xie, X.-C. Zhang, Detection of Broadband Terahertz Waves with a Laser-Induced Plasma in Gases, Phys. Rev. Lett. 97 (2006) 103903.

[45] Y. Minami, Y. Hayashi, J. Takeda, I. Katayama, Single-shot measurement of a terahertz electric-field waveform using a reflective echelon mirror, Appl. Phys. Lett. 103 (2013) 051103.

[46] I. Katayama, H. Aoki, J. Takeda, H. Shimosato, M. Ashida, R. Kinjo, I. Kawayama, M. Tonouchi, M. Nagai, K. Tanaka, Ferroelectric Soft Mode in a SrTiO3 Thin Film Impulsively Driven to the Anharmonic Regime Using Intense Picosecond Terahertz Pulses, Phys. Rev. Lett. 108 (2012) 097401.

[47] S. Fleischer, Y. Zhou, R.W. Field, K.A. Nelson, Molecular Orientation and Alignment by Intense Single-Cycle THz Pulses, Phys. Rev. Lett. 107 (2011) 163603.

[48] M.C. Hoffmann, J. Hebling, H.Y. Hwang, K.-L. Yeh, K.A. Nelson, Impact ionization in InSb probed by terahertz pump—terahertz probe spectroscopy, Phys. Rev. B. 79 (2009) 161201.

14

[49]   H. Hirori, K. Shinokita, M. Shirai, S. Tani, Y. Kadoya, K. Tanaka, Extraordinary carrier multiplication gated by a picosecond electric field pulse, Nat. Commun. 2 (2011) 594.

[50]   C. Lange, T. Maag, M. Hohenleutner, S. Baierl, O. Schubert, E.R.J. Edwards, D. Bougeard, G. Woltersdorf, R. Huber, Extremely Nonperturbative Nonlinearities in GaAs Driven by Atomically Strong Terahertz Fields in Gold Metamaterials, Phys. Rev. Lett. 113 (2014) 227401.

[51]   M. Liu, H.Y. Hwang, H. Tao, A.C. Strikwerda, K. Fan, G.R. Keiser, A.J. Sternbach, K.G. West, S. Kittiwatanakul, J. Lu, S.A. Wolf, F.G. Omenetto, X. Zhang, K.A. Nelson, R.D. Averitt, Terahertz-field-induced insulator-to-metal transition in vanadium dioxide metamaterial, Nature. 487 (2012) 345–348.

[52]   R. Matsunaga, Y.I. Hamada, K. Makise, Y. Uzawa, H. Terai, Z. Wang, R. Shimano, Higgs Amplitude Mode in the BCS Superconductors $Nb_{1-x}Ti_xN$ Induced by Terahertz Pulse Excitation, Phys. Rev. Lett. 111 (2013) 057002.

[53]   R. Matsunaga, N. Tsuji, H. Fujita, A. Sugioka, K. Makise, Y. Uzawa, H. Terai, Z. Wang, H. Aoki, R. Shimano, Light-induced collective pseudospin precession resonating with Higgs mode in a superconductor, Science. 345 (2014) 1145–1149.

[54]   T.L. Cocker, V. Jelic, M. Gupta, S.J. Molesky, J.A.J. Burgess, G.D.L. Reyes, L. V. Titova, Y.Y. Tsui, M.R. Freeman, F.A. Hegmann, An ultrafast terahertz scanning tunnelling microscope, Nat. Photonics. 7 (2013) 620–625.

[55]   K. Yoshioka, Y. Minami, K. Shudo, T.D. Dao, T. Nagao, M. Kitajima, J. Takeda, I. Katayama, Terahertz-Field-Induced Nonlinear Electron Delocalization in Au Nanostructures, Nano Lett. 15 (2015) 1036–1040.

[56]   K. Yoshioka, I. Katayama, Y. Minami, M. Kitajima, S. Yoshida, H. Shigekawa, J. Takeda, Real-space coherent manipulation of electrons in a single tunnel junction by single-cycle terahertz electric fields, Nat. Photonics. 10 (2016) 762–765.

[57]   J. Takeda, K. Yoshioka, Y. Minami, I. Katayama, Nanoscale electron manipulation in metals with intense THz electric fields, J. Phys. D. Appl. Phys. 51 (2018) 103001.

[58] K. Yoshioka, I. Katayama, Y. Arashida, A. Ban, Y. Kawada, K. Konishi, H. Takahashi, J. Takeda, Tailoring Single-Cycle Near Field in a Tunnel Junction with Carrier-Envelope Phase-Controlled Terahertz Electric Fields, Nano Lett. 18 (2018) 5198–5204.

Chapter 2

Experimental Methods and Concepts

In this chapter, we will introduce the experimental methods and concepts relevant to the studies presented in this thesis. The CEP-controlled single-cycle THz electric field, a vital tool for these studies, is realized based on commercial ultrafast femtosecond laser sources and custom-built ultrafast spectroscopy apparatus. We first discuss the nature of the ultrashort laser pulses and then explain the methods for the generation and detection of the THz pulses using femtosecond laser sources. Furthermore, the experimental realization of the CEP tuning of the single-cycle THz pulse is described in detail, which is vital for investigating ultrafast coherent control of electrons. Finally, we briefly introduce the principle and concept of scanning tunneling microscopy, which we combined with ultrafast THz spectroscopy to achieve a new experimental regime that is ultrafast and ultrasmall.

2.1 Ultrashort laser pulses

In the time domain, the electric field of ultrashort laser pulses can be simply described by multiplying the oscillatory electric field of a monochromatic plane wave with a slowly varying envelope function $F(t)$ as follows [1,2]:

$$\tilde{E}(t) = F(t)\exp\left[i\phi(t)\right].$$

(2.1)

where $\phi(t)$ is the temporal phase. We describe the electric field in complex form for mathematical convenience. However, the real part is the only measurable quantity. The relationship between the pulse duration and the spectral width of an ultrashort laser pulse are given by general time and frequency Fourier transformations:

$$\tilde{E}(\omega) = \frac{1}{2\pi} \int_{-\infty}^{+\infty} \tilde{E}(t)e^{i\omega t}dt, \tag{2.2}$$

$$\tilde{E}(t) = \frac{1}{2\pi} \int_{-\infty}^{+\infty} \tilde{E}(\omega)e^{-i\omega t}d\omega. \tag{2.3}$$

Therefore, the electric field of the laser pulse (2.1) in the frequency domain is given by the Fourier transform

$$\tilde{E}(\omega) = F(\omega)\exp\left[i\phi(\omega)\right], \tag{2.4}$$

where $F(\omega)$ is the envelope function and $\phi(\omega)$ is the spectral phase. The pulse duration $\Delta\tau$ and the spectral width $\Delta\omega$ are experimentally accessible at full width at half-maximum (FWHM) and satisfy the uncertainty principle:

$$\Delta\tau \cdot \Delta\omega \geq K. \tag{2.5}$$

The spectral width is defined as the FWHM of the spectral profile ($\propto F(\omega)^2$). The constant K is determined by the envelope function $F(t)$. For example, $K = 0.441$ [1] for a Gaussian-shaped function ($F_G(t) = \exp[-(t/\Delta\tau)^2]$). The pulse duration depends on the spectral width. In order to generate a single-cycle electric field, the octave-spanning spectral width and its phase control are required. The equality in equation (2.5) holds when the laser pulses are unchirped and reach the shortest transform-limited pulse for a given spectral width. The spectral phase of ultrashort laser pulse can be expressed as a Taylor expansion around the central frequency ω_0 of the laser pulse:

$$\phi(\omega) = \phi(\omega_0) + (\omega - \omega_0)\frac{\partial\phi}{\partial\omega}\bigg|_{\omega_0} +$$

$$+ \frac{1}{2}(\omega - \omega_0)^2\frac{\partial^2\phi}{\partial\omega^2}\bigg|_{\omega_0} + \frac{1}{6}(\omega - \omega_0)^3\frac{\partial^3\phi}{\partial\omega^3}\bigg|_{\omega_0} + \dots. \tag{2.6}$$

The first term describes the carrier envelope phase (CEP), denoted ϕ_{CEP},
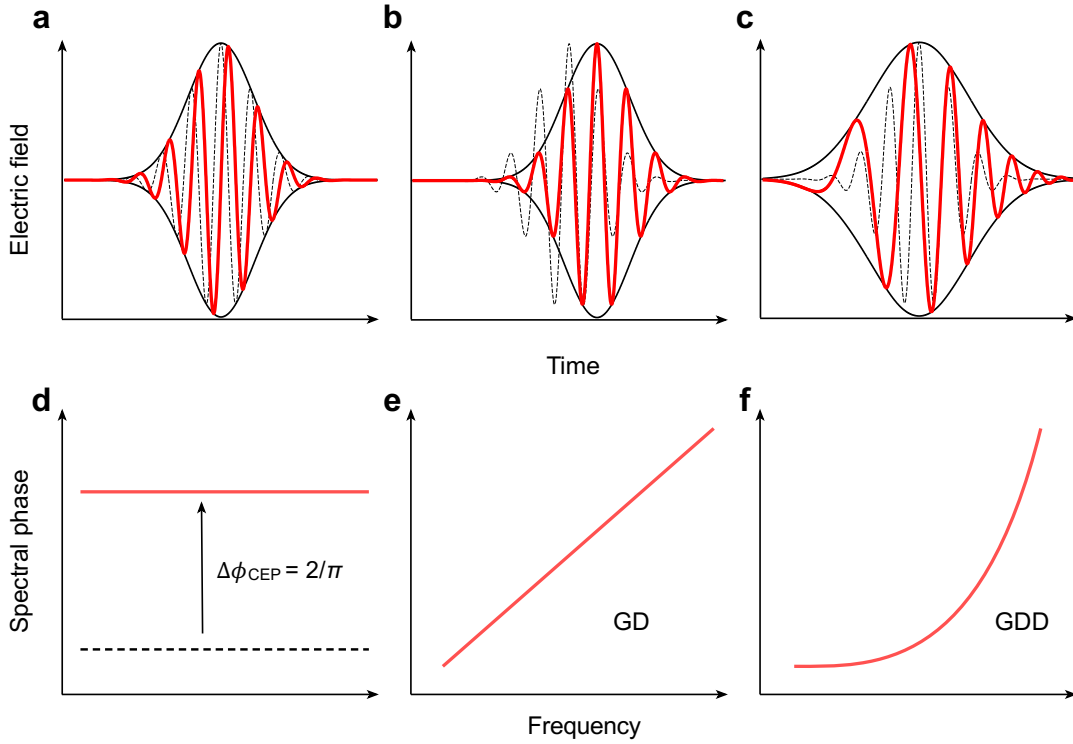
Figure 2.1 | Influence of the spectral phase on the electric field of ultrashort laser pulses. (a–c) Influence of the CEP, GD and GDD, respectively, on the electric field and the envelope. The dashed curve shows the original waveform without phase shift. The envelope was modeled using Gaussian-shaped function. **(d–f)**, The spectral phase shift as a function of frequency corresponding to **(a–c)**.

which is the phase between the carrier wave (electric field) and the position of the intensity envelope of the pulse ($F(t)$) (see Figure 2a, d). The second term is the group delay (GD) which induces the overall time shift of the laser pulse while the temporal pulse shape remains unchanged (see Figure 2b, e); this is directly related to the group velocity. The third term corresponds to the group delay dispersion (GDD) which leads to pulse broadening due to different groups velocities in different spectra. The GDD and the chirp $\alpha(t)$ are related (with Gaussian-shaped envelope function) by

$$\alpha(t) = -\frac{\partial^2 \phi(t)}{\partial t^2} = \frac{GDD\sigma^4}{1 + GDD^2\sigma^4}, \tag{2.7}$$

where $\sigma = 2\sqrt{\ln 2}/\Delta\tau$, and both the envelope and the phase of the laser pulse are distorted (see Figure 2c, f). The compensation of the chirp is an essential procedure for ultrashort laser pulses. When the spectral phase is a cubic

function of the frequency, the fourth term, which is called third order dispersion (TOD), becomes observable. The TOD appears as small sidebands alongside the main peak of the laser pulse, which often happens in mode-locked laser pulse generation. All of these spectral phase terms have to be presicelly controlled especially in the non-perturbative regime, in which the motion of electrons in the system is coherently driven by the electric field of ultrashort laser pulses.

However, in a typical pulsed laser source, such as the femtosecond mode-locked oscillator and amplifier, the CEP is different from shot to shot. This imperfection comes from the difference in group velocity v_g and phase velocity v_{ph} in the laser cavity, which is given by

$$v_g = \frac{\partial \omega}{\partial k},$$

(2.8)
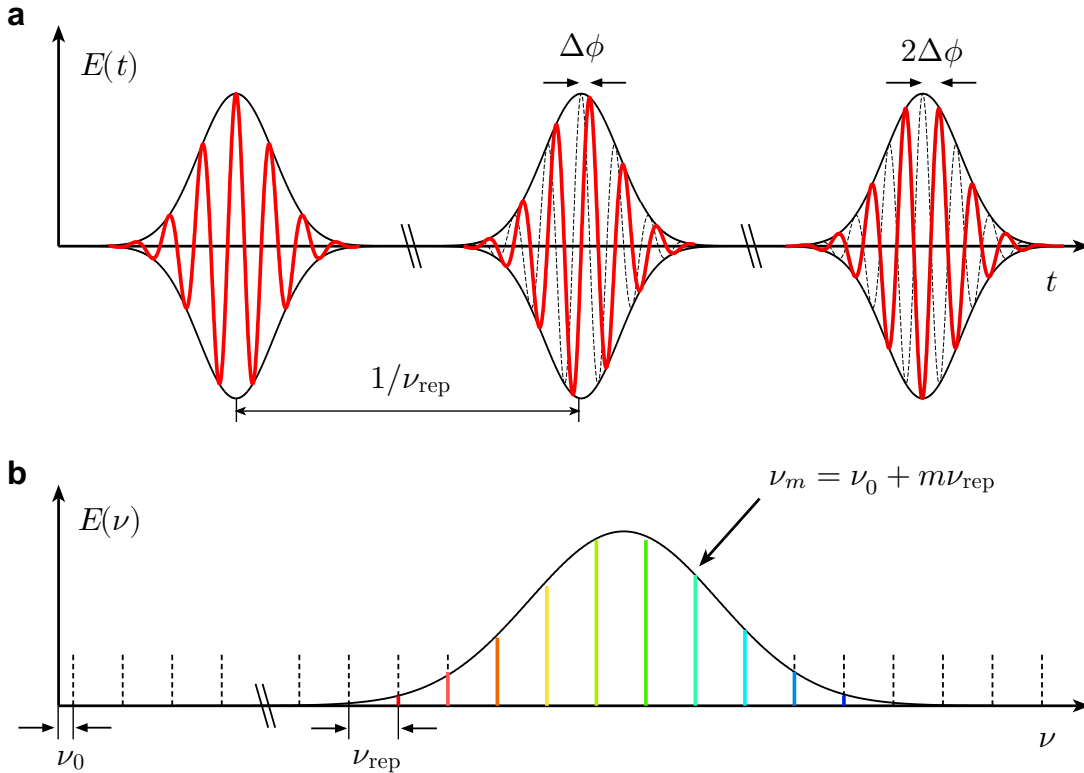
Figure 2.2 | Typical few-cycle ultrashort laser pulses. (a) Ultrashort laser pulses with repetition rate ν_{rep}. The phase between the carrier wave and pulse envelope fluctuate by $\Delta\phi$ from shot to shot. **(b)** Optical comb obtained by the Fourier transform of **(a)**; ν_0 is the offset frequency which is related to the carrier envelope offset by $\nu_0 = \Delta\phi/2\pi \cdot \nu_{rep}$.

$$v_{ph} = \frac{\omega}{k}, \tag{2.9}$$

where k is the wavenumber. The group velocity describes the velocity of the envelope of the propagating laser pulse, whereas the phase velocity describes the velocity of a single carrier wave. Figure 2.2 shows the pulse train of a typical few-cycle laser pulse in both the time domain (2.2a) and frequency domain (2.2b). In the frequency domain, a laser pulse train with repetition rate ν_{rep} forms a comb structure with equal intervals identical to the repetition rate. The entire frequency comb is offset from zero by the carrier envelope offset frequency ν_0, which is related to the CEP shift between two adjacent pulses $\Delta\phi$ (carrier envelope offset) in the time domain by $\nu_0 = \Delta\phi/2\pi \cdot \nu_{rep}$. Therefore, the frequency comb can be described by the following simple relationship

$$\nu_m = \nu_0 + m\nu_{rep}, \tag{2.10}$$

where m is a natural number. Because ν_{rep} is determined by the cavity length of the laser oscillator, one can obtain well-defined frequency makers by precisely controlling ν_0. A frequency comb of this nature was extensively studied in the last decade [3] for its important applications in high precision metrologies [4–7]. In order to drive ultrafast coherent motion of electrons, the fluctuation of the CEP has to be perfectly stabilized ($\Delta\phi = 0$) otherwise the coherent field effect averages out from shot to shot. The development of an optical frequency comb made it possible to stabilize the CEP of near-infrared (NIR) pulses by precisely controlling ν_0 in the frequency domain. This invention stimulated scientists to engineer coherent motion of electrons and transient states of matter at the shortest timescales, that is, within a single-cycle of ultrashort laser pulses.

2.2 Femtosecond laser system

Ultrafast spectroscopy with femtosecond temporal resolution and strong-field physics with high intensity is based on ultrafast laser technology. We utilized a near-infrared (NIR) femtosecond oscillator and amplifier system as shown in Figure 2.3. Firstly, low-energy high-repetition rate femtosecond laser pulses are generated using a Kerr-lens mode-locked oscillator with laser gain medium

using titanium-doped sapphire (Ti:Sapphire). This Ti:Sapphire oscillator (<100 fs, 80 MHz, 0.5 W, Tsunami, Spectra-Physics) is seeded by a CW diode-pumped solid state laser (532 nm, 4.5 W, Millennia Prime, Spectra-Physics). Then, femtosecond pulses are amplified based on chirp pulse amplification [8]. The stretched oscillator pulses are first amplified using a regenerative amplifier, temporally gated from a repetition of 80 MHz to 1 KHz with a Q-switched pump laser and further amplified using a multipass amplifier. Finally, our femtosecond laser system delivers 2 mJ pulse energy with a pulse duration less than 130 fs and 1 kHz repetition rate with center wavelength of 800 nm (Integra C, Quantronix). This high-energy femtosecond laser source is used throughout the research described in this thesis; specifically, THz time-domain spectroscopy (THz-TDS) in Chapter 3, and THz scanning tunneling microscopy (THz-STM) in Chapters 4 and 5.

2.3 Generation and detection of THz electric field

2.3.1 Optical rectification

In the last decade, a number of systems were investigated to generate the THz electric field in order to fill the so-called "THz gap" [9], including photo-conductive switches [10–12], organic and inorganic nonlinear crystals [13–24], laser-excited air plasma [25,26], and metallic spintronic emitters [27,28]. Among these, the most standard technique to generate a broadband THz electric field is optical rectification (OR) via nonlinear crystals because of
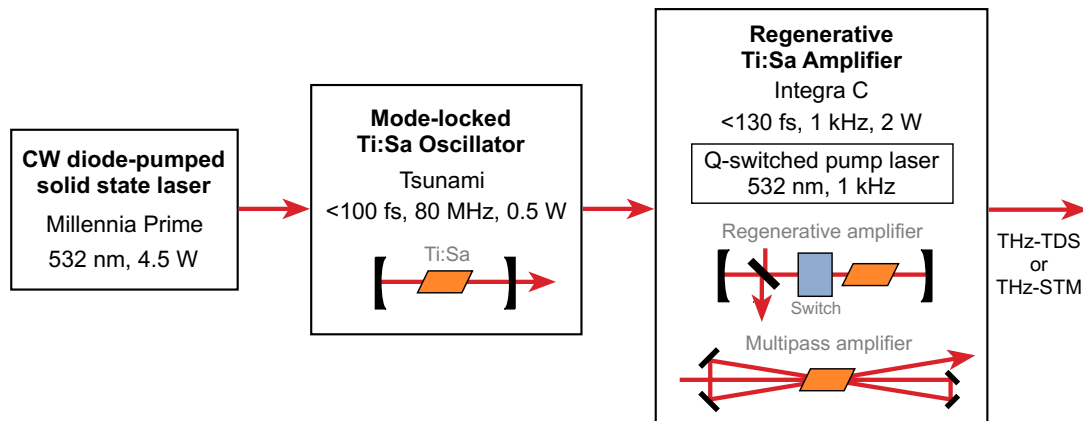
Figure 2.3 | Schematic of the femtosecond laser system.

the method's efficiency and practicality. We now describe the basic principles of OR.

OR is based on second order nonlinear polarization in the material which is represented by the difference frequency ω_1, ω_2 of incoming laser pulse by $\omega_1 - \omega_2$. We now consider the case when the broadband laser pulse is incident on a crystal having nonlinear polarization $P^{(2)}$. In the frequency domain, second order nonlinear polarization is given by

$$P_i^{(2),\pm}(\omega_3 = \omega_1 \pm \omega_2) = \sum_{\omega_3 = \omega_1 \pm \omega_2} \sum_{jk} \epsilon_0 \chi_{ijk}^{(2)}(\omega_3 = \omega_1 \pm \omega_2) \tilde{E}_j(\omega_1) \tilde{E}_k(\pm\omega_2), \quad (2.11)$$

where $\tilde{E}_i(\omega)$ is the component ($i = x,\ y,\ z$) of the Fourier transform of the incident light electric field and $\chi_{ijk}^{(2)}$ is the second order nonlinear susceptibility. Focusing on the difference frequency $\Omega = \omega_1 - \omega_2$, equation (2.11) can be written as

$$P_i^{(2),-}(\Omega) = \int_{-\infty}^{\infty} \sum_{jk} \epsilon_0 \chi_{ijk}^{(2)} \tilde{E}_j(\omega_2 + \Omega) \tilde{E}_k^*(\omega_2) d\omega_2. \quad (2.12)$$

Taking the Fourier transform of equation (2.12), this polarization is given in the time domain by

$$P_i^{(2),-}(t) = \int_{-\infty}^{\infty} P_i^{(2),-}(\Omega) e^{i\Omega t} d\Omega,$$

$$= \int_{-\infty}^{\infty} \sum_{jk} \epsilon_0 \chi_{ijk}^{(2)} \tilde{E}_j(\omega_2 + \Omega) \tilde{E}_k^*(\omega_2) d\omega_2 e^{i\Omega t} d\Omega,$$

$$= \sum_{jk} \epsilon_0 \chi_{ijk}^{(2)} \int_{-\infty}^{\infty} \tilde{E}_j(\omega_2 + \Omega) e^{i(\omega_2 + \Omega)t} d\Omega \int_{-\infty}^{\infty} \tilde{E}_k^*(\omega_2) e^{-i\omega_2 t} d\omega_2,$$

$$= \sum_{jk} \epsilon_0 \chi_{ijk}^{(2)} E_j(t) E_k(t) \propto I(t), \quad (2.13)$$

where $E_i(t)$ is the component ($i = x,\ y,\ z$) of the incident light electric field. Note that we ignore frequency dependence of the second order nonlinear susceptibility. By using femtosecond laser pulses as incident light, we can generate the THz electric field using OR. Equation (2.13) shows that the time evolution of the nonlinear polarization is proportional to the intensity envelope of the incident laser pulse. Therefore, the CEP of the generated THz electric

field is inherently stable, regardless of the CEP of incident NIR laser pulses. Alternatively, this CEP stabilization can be understood by cancellation of the offset frequency ν_0 of NIR pulses thorough the difference frequency process. The CEP stability of THz pulses coming from OR is much higher compared to active CEP stabilization using an *f*-to-2*f* interferometer which is commonly used in NIR femtosecond pulses [29–31]. Accurate manipulation of electron tunneling, required by the research described in this thesis, cannot be achieved without this highly stable CEP controlled THz electric field.

2.3.2 Velocity matching by tilted pulse front in LiNbO₃

There are several nonlinear crystals that are commonly used for OR-based THz sources: organic crystals such as 4-*N,N*-dimethylamino-4'-*N'*-methyl-stilbazolium tosylate (DAST) [13,14], (2-(3-(4-hydroxystyryl)-5,5-dimethylcyclohex-2-enylidene)malononitrile) (OH1) [19], and 4-*N,N*-dimethylamino-4'-*N'*-methyl-stilbazolium 2,4,6-trimethylbenzenesulfonate (DSTMS) [20]; or inorganic crystals such as zink telluride (ZnTe) [22], gallium phosphide (GaP) [23], gallium selenide (GaSe) [15,16,24], and lithium niobate (LiNbO₃) [17,18].

Organic crystals show very high conversion efficiency and an extremely high peak electric field of 83 MV/cm was reported recently [21]. On the other hand, these organic crystals suffer from heat damage, especially when pumped by high power and high repetition rate laser sources.

Among the inorganic crystals, LiNbO₃ is the most fascinating THz emitter due to its high nonlinear coefficient, which can be as high as $d_{\text{eff}} = 168$ pm/V [32], exceeding the value associated with other inorganic crystals (ZnTe : 4 pm/V, GaP : 1 pm/V, GaSe : 54.4 pm/V) [24,33]. In addition, the large bandgap energy of LiNbO₃ (3.8 eV) prevents two-photon absorption of incident NIR pulses and thus reaches a high optical damage threshold of approximately 1 J/cm^2, which enables intense THz generation through OR of mJ/pulse class high-power NIR femtosecond laser pulses. However, in order to convert the frequency of NIR pulse with high efficiency based on OR, phase matching conditions have to be fulfilled in order to avoid destructive interference during propagation inside the crystal, which is given by

$$v_{NIR}^{gr} = v_{THz}^{ph}, \tag{2.13}$$

where v_{NIR}^{gr} is the group velocity of propagating NIR femtosecond pulses,

and v_{THz}^{ph} is the phase velocity of the generated THz electric field.

Unfortunately, NIR femtosecond pulses with a center wavelength of 800 nm propagate much faster than the generated THz electric field at a frequency of 1 THz, by a factor of more than 2 ($n_{800\text{nm}}$: 2.25, n_{THz} : 4.96). This velocity mismatch can be overcome by using a Cherenkov-type phase matching scheme, first introduced by Hebling *et al.* in 2002 [34]. If a charged particle emitting electromagnetic radiation is propagating faster than the group velocity of the emitted radiation in the surrounding medium, the emitted radiation forms a corn structure as shown in Figure 2.4a. This radiation is called Cherenkov radiation, discovered by Pavel Cherenkov in 1934, for which he was awarded the Nobel Prize in 1958. Replacing the charged particle with the nonlinear polarization propagating inside the LiNbO₃ crystal created by NIR femtosecond laser pulses yields the same situation emitting THz radiation with the Cherenkov angle Θc, which is given by

$$v_{NIR}^{gr} \cdot \cos \Theta_c = v_{THz}^{ph}.$$

(2.14)

However, the conversion efficiency is low in this configuration because of the
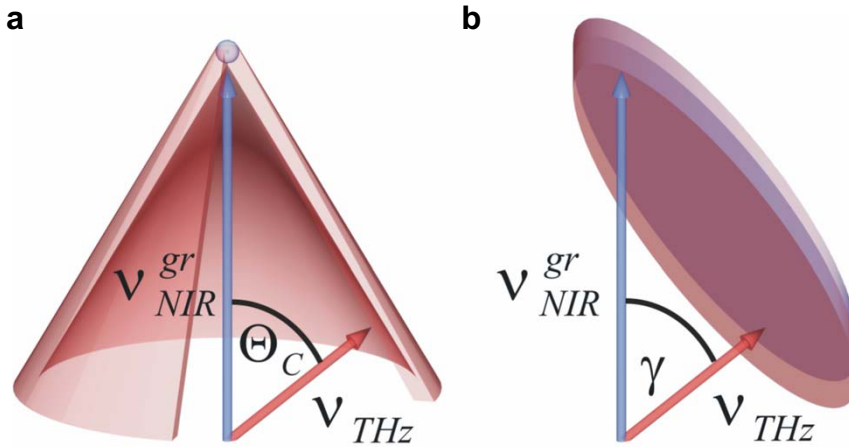
Figure 2.4 | Cherenkov-type phase matching in LiNbO₃. (a) If the pump spot of the excitation NIR pulse is sufficiently small compared to its longitudinal spread inside the LiNbO₃, then THz radiation analogous to Cherenkov radiation emitted from an accelerated charged particle. Therefore, THz pulses are generated with Cherenkov angle Θc. However, the conversion efficiency is low because of the limited beam size. **(b)** By tilting the pulse front of the NIR pulse, the phase matching condition holds for large cross-section and thus yields high conversion efficiency if the tilt angle γ is equal to Cherenkov angle Θc. These figures are adapted from Ref. [32].

narrow transverse beam profile of the NIR pulse. This drawback can be overcome by tilting the pulse front of the NIR pump pulses by an angle γ, as shown in Figure 2.4b. According to Huygens' principle, the THz radiation excited impulsively along this tilted pulse front will propagate perpendicularly to this front with velocity v_{THz}^{ph}. Consequently, the phase matching condition of equation (2.13) may be written as

$$v_{NIR}^{gr} \cdot \cos \gamma = v_{THz}^{ph}. \tag{2.14}$$

Therefore, if $\Theta c = \gamma = \cos^{-1}(v_{THz}^{ph}/v_{NIR}^{gr})$, the phase matching condition is fulfilled for a large cross-section of pump NIR femtosecond pulse and thus enables high conversion efficiency and the generation of intense THz electric fields. Furthermore, this Cherenkov-type phase matching makes it possible to choose the highest nonlinear coefficient by setting the polarization of the NIR pump and THz pulses parallel to the c-axis of the $LiNbO_3$ crystal.

We now describe our experimental setup for Cherenkov-type phase matching in order to generate the CEP-stable single-cycle intense THz electric field. The pulse front of the NIR femtosecond pulse is tilted using a diffraction grating, as shown in Figure 2.5. In the case of a monochromatic wave, the tilted angle θ after fast order diffraction is given by

$$\theta = \tan^{-1}(\cos \theta_d / p\lambda), \tag{2.15}$$
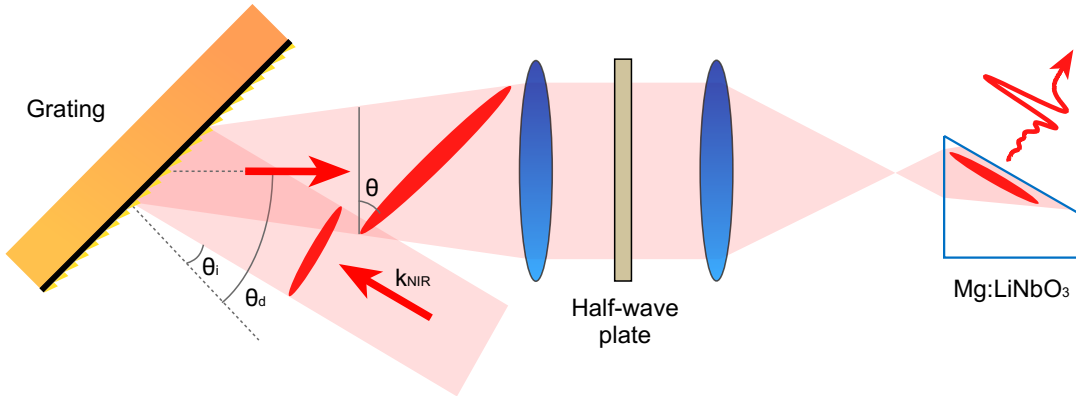
Figure 2.5 | Schematic of intense THz electric field generation based on tilted pulse front excitation. The pulse front of the NIR pulse is tilted using first order diffraction at the grating, and then collimated and focused on to MgO-doped $LiNbO_3$. Here, a grating with groove density of $p = 1500$ or 2000 mm^{-1} has been chosen. The $LiNbO_3$ is cut at an angle of 62° to fulfill the phase matching condition.

where θ_d is the diffracted angle, p is the groove density of the grating, and λ is the wavelength of incident light. However, angular dispersion of the broadband NIR pulses requires additional optical components to correctly image the tilted pulse front on the LiNbO$_3$ crystal. Here, we utilize a system of two lenses for collimation and then focus the NIR pulses as shown in Figure 2.5. A half-wave plate is used to rotate polarization by 90° in order to achieve the largest nonlinear coefficient in LiNbO$_3$ because *p*-polarized light shows the best diffraction efficiency at the grating. By taking the diffraction grating and the lens system into account, the tilt angle γ within LiNbO$_3$ is given by

$$\gamma = \tan^{-1}\left(\frac{\lambda_0 p}{n_{NIR}^{gr}\beta\cos\theta_d}\right), \tag{2.16}$$

where λ_0, and n_{NIR}^{gr} are the central pump pulse wavelength and group refractive index of the pump NIR pulse, respectively, and β is the horizontal magnification factor of the pulse front, which is determined by the grating and lenses. The appropriate tilt angle γ can be determined by solving equation (2.14), and is determined to be $\gamma = 62°$ with our MgO-doped LiNbO$_3$, which is used here for enhancing the optical damage threshold. With this setup, we are able to generate the CEP stable intense single-cycle THz electric field with peak amplitude exceeding 400 kV/cm.

2.3.2 Electro-optic sampling

In order to clarify the nonlinear interaction between electrons and ultrashort laser pulses under a non-perturbative regime, it is necessary to detect both the amplitude and phase of the electric field within the light pulse, whereas conventional spectroscopy can only access the intensity envelope. In THz spectroscopy, the electric field is directly resolved in the time domain using electro-optic sampling (EOS) [24,35–37]. EOS is based on the Pockels effect which is a linear electro-optic effect.

Pockels effect

In the presence of an external electric field, polarization in the crystal induces birefringence due to the anisotropy of refractive index in the crystal. The index ellipsoid of a crystal in an external electric field of *E* is given by

$$a_{11}X^2 + a_{22}Y^2 + a_{33}Z^2 + 2a_{23}YZ + 2a_{31}ZX + 2a_{12}XY = 1, \qquad (2.17)$$

where X, Y, Z are the principal axes of the crystal without electric field. Without the electric field of E, a_{ij} can be written as

$$a_{ij}^0 = \frac{1}{n_i^2}\delta_{ij}, \qquad (2.18)$$

where n_i is the principle refractive index along the i direction. When E is sufficiently low, the variation of a_{ij} is given by

$$\Delta a_{ij} = a_{ij} - a_{ij}^0 = \sum_k \gamma_{ijk}E_k, \qquad (2.19)$$

where γ_{ijk} is the electro-optic coefficient; γ_{ijk} is symmetric with respect to i, and j, and therefore equation (2.19) can be rewritten, using matrices and the simplified index notation given in Table 2.1, as follows:

$$\begin{bmatrix} \Delta a_1 \\ \Delta a_2 \\ \vdots \\ \Delta a_6 \end{bmatrix} = \begin{bmatrix} \gamma_{11} & \gamma_{12} & \gamma_{13} \\ \gamma_{21} & \cdots & \gamma_{23} \\ \vdots & \ddots & \vdots \\ \gamma_{61} & \cdots & \gamma_{63} \end{bmatrix} \begin{bmatrix} E_X \\ E_Y \\ E_Z \end{bmatrix}. \qquad (2.20)$$

m	1	2	3	4	5	6
jk	xx	yy	zz	yz	zx	xy
				zy	xz	yx

Table1 | Correspondence on index notation

Polarization dependence of THz-field induced birefringence

Figure 2.6 shows birefringence schematically in the (110)-oriented EO crystal and the coordinate system we used.

We now consider the THz polarization dependence of birefringence induced by the Pockels effect. By taking crystal symmetry in the EO crystal into account, the non-zero component in the EO coefficient (see equation (2.20)) is only $\gamma_{41} = \gamma_{52} = \gamma_{63}$. In addition, without an external electric field, the EO crystal is an isotropic medium and thus the index ellipsoid in XYZ coordinates is given by

$$\frac{X^2}{n^2} + \frac{Y^2}{n^2} + \frac{Z^2}{n^2} + 2\gamma_{41}\left(E_X^{\mathrm{THz}}YZ + E_y^{\mathrm{THz}}ZX + E_Z^{\mathrm{THz}}XY\right) = 1, \quad (2.21)$$

where n is the refractive index when the electric field is absent. Rewriting using matrices we obtain

$$[X \ \ Y \ \ Z]\begin{bmatrix} \frac{1}{n^2} & \gamma_{41}E_Z^{\mathrm{THz}} & \gamma_{41}E_Y^{\mathrm{THz}} \\ \gamma_{41}E_Z^{\mathrm{THz}} & \frac{1}{n^2} & \gamma_{41}E_X^{\mathrm{THz}} \\ \gamma_{41}E_Y^{\mathrm{THz}} & \gamma_{41}E_X^{\mathrm{THz}} & \frac{1}{n^2} \end{bmatrix}\begin{bmatrix} X \\ Y \\ Z \end{bmatrix} = 1. \quad (2.22)$$

Next, we convert the matrix (2.20) into the XYZ coordinate system using the following transformation matrix A.

$$A = \begin{bmatrix} -\frac{1}{\sqrt{2}} & 0 & \frac{1}{\sqrt{2}} \\ \frac{1}{\sqrt{2}} & 0 & \frac{1}{\sqrt{2}} \\ 0 & 1 & 0 \end{bmatrix}. \quad (2.23)$$

As shown in Figure 2.6c, polarization of THz electric field in XYZ coordinates is given by
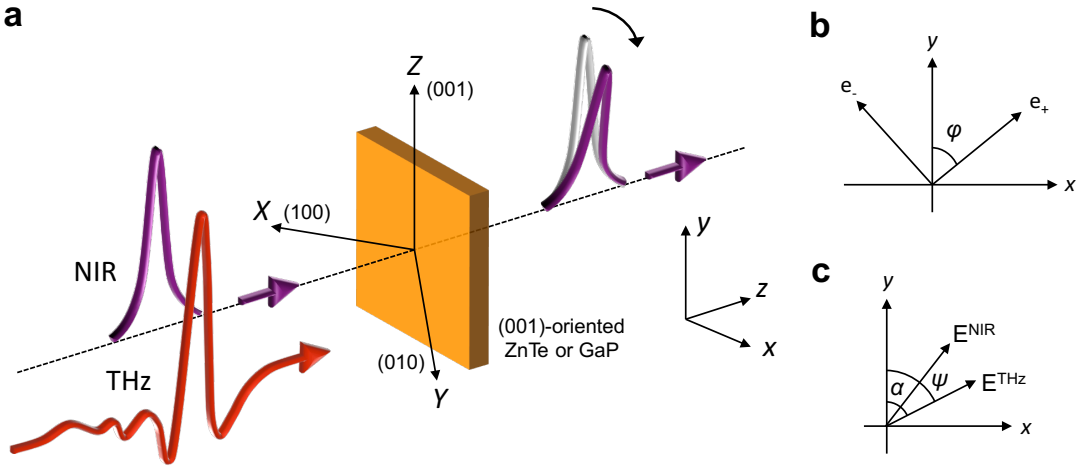
Figure 2.6 | Schematic of birefringence in the EO crystal induced by THz electric field. (a) The THz electric field and NIR probe pulse were both incident normally on the (110)-oriented EO crystal. Polarization of the NIR pulse is changed by THz-field induced birefringence at the EO crystal. **(b)** The principle axes of the index ellipsoid. **(c)** Polarization angle of the THz electric field and NIR probe pulse.

$$
\begin{bmatrix} E_X \\ E_Y \\ E_Z \end{bmatrix}_{XYZ} = E^{\text{THz}} A \begin{bmatrix} \sin\psi \\ \cos\psi \\ 0 \end{bmatrix}_{xyz} = E^{\text{THz}} \begin{bmatrix} -\dfrac{1}{\sqrt{2}}\sin\psi \\ \dfrac{1}{\sqrt{2}}\sin\psi \\ \cos\psi \end{bmatrix}_{XYZ} . \tag{2.24}
$$

Therefore, equation (2.22) can be rewritten as

$$
[x \ y \ z] \begin{bmatrix} \dfrac{1}{n^2} - \gamma_{41} E^{\text{THz}}\cos\psi & -\gamma_{41}E^{\text{THz}}\sin\psi & 0 \\ -\gamma_{41}E^{\text{THz}}\sin\psi & \dfrac{1}{n^2} & 0 \\ 0 & 0 & \dfrac{1}{n^2} + \gamma_{41}E^{\text{THz}}\cos\psi \end{bmatrix} \begin{bmatrix} x \\ y \\ z \end{bmatrix} = 1.
$$

$$\tag{2.25}$$

Here, both the THz and NIR pulses propagate along the z axis, therefore we focus on intersection with a plane $z = 0$. This ellipse is given by

$$
[x \ y] \begin{bmatrix} \dfrac{1}{n^2} - \gamma_{41}E^{\text{THz}}\cos\psi & -\gamma_{41}E^{\text{THz}}\sin\psi \\ -\gamma_{41}E^{\text{THz}}\sin\psi & \dfrac{1}{n^2} \end{bmatrix} \begin{bmatrix} x \\ y \end{bmatrix} = 1. \tag{2.26}
$$

By solving the secular equation of this matrix, we obtain the eigenvector and eigenvalue related to the principle axis of birefringence and refractive index along the principle axis, respectively. The eigenvector is given by

$$
\mathbf{e}_{\pm} \parallel \begin{bmatrix} -\dfrac{2\sin\psi}{\cos\psi \pm \sqrt{1 + 3\sin^2\psi}} \\ 1 \end{bmatrix} = \begin{bmatrix} \dfrac{1 \mp \sqrt{1 + 4\tan^2\psi}}{2\tan\psi} \\ 1 \end{bmatrix} . \tag{2.27}
$$

Here, we use relationship of the trigonometric function given by

$$
\tan\varphi = \frac{-1 + \sqrt{1 + \tan^2 2\varphi}}{\tan 2\varphi}, \tag{2.28}
$$

and define $\tan 2\varphi \equiv -2\tan\psi$ in order to normalize the eigenvector (2.27), giving

$$
\mathbf{e}_{+} = \begin{bmatrix} \sin\varphi \\ \cos\varphi \end{bmatrix}, \quad \mathbf{e}_{-} = \begin{bmatrix} -\cos\varphi \\ \sin\varphi \end{bmatrix}, \tag{2.29}
$$

which represents the principle axis of birefringence as shown in Figure 2.6b. On the other hand, the refractive index along principle axis is related to eigenvalue $s_\pm$, and is given by

$$n_\pm = \frac{1}{\sqrt{s_\pm}} = \left(\frac{1}{n^2} + \frac{1}{2} \gamma_{41} E^{\text{THz}} \left(-\cos\psi \pm \sqrt{1 + 3\sin^2\psi} \right) \right)^{-\frac{1}{2}}. \quad (2.30)$$

Expansion of $\Delta n \equiv n_+ - n_-$ with first order of $\gamma_{41} E^{\text{THz}}$ gives

$$\Delta n \approx \frac{\gamma_{41} E^{\text{THz}} n^3 \sqrt{1 + 3\sin^2\psi}}{2}. \quad (2.31)$$

Therefore, the phase difference δ induced by birefringence is given by

$$\delta = \frac{2\pi l \delta n}{\lambda} = \frac{2\pi l}{\lambda} \frac{\gamma_{41} E^{\text{THz}} n^3 \sqrt{1 + 3\sin^2\psi}}{2}, \quad (2.32)$$

where l is the thickness of the EO crystal and λ is the center wavelength of the NIR pulse. Finally, the phase difference δ is a maximum when $\psi = \pi/2$, and $\varphi = \pi/4$, and is given by

$$\delta_{\text{max}} = \frac{2\pi l \gamma_{41} E^{\text{THz}} n^3}{\lambda}. \quad (2.33)$$

Experimental setup of EOS

We now describe the experimental setup of EOS using balanced detection, shown in Figure 2.7a. After passing through the EO crystal, a quarter-wave plate (QWP) is placed at 45° in order to make the probe pulse circularly polarized. The Wollaston prism (WP) spatially separates two orthogonal polarization components of the probe pulse. Consequently, the difference between the two intensities on the photodiodes is zero. However, co-propagating the THz electric field induces a probe pulse that is elliptically polarized because of birefringence in the EO crystal, and thus THz induced polarization change can be measured on the photodiodes as the difference signal. Ideally, this scheme results in cancellation of common-mode noise of the probe beam, which is advantageous for high-sensitivity detection.

We now discuss polarization dependence of balanced detection. We denote
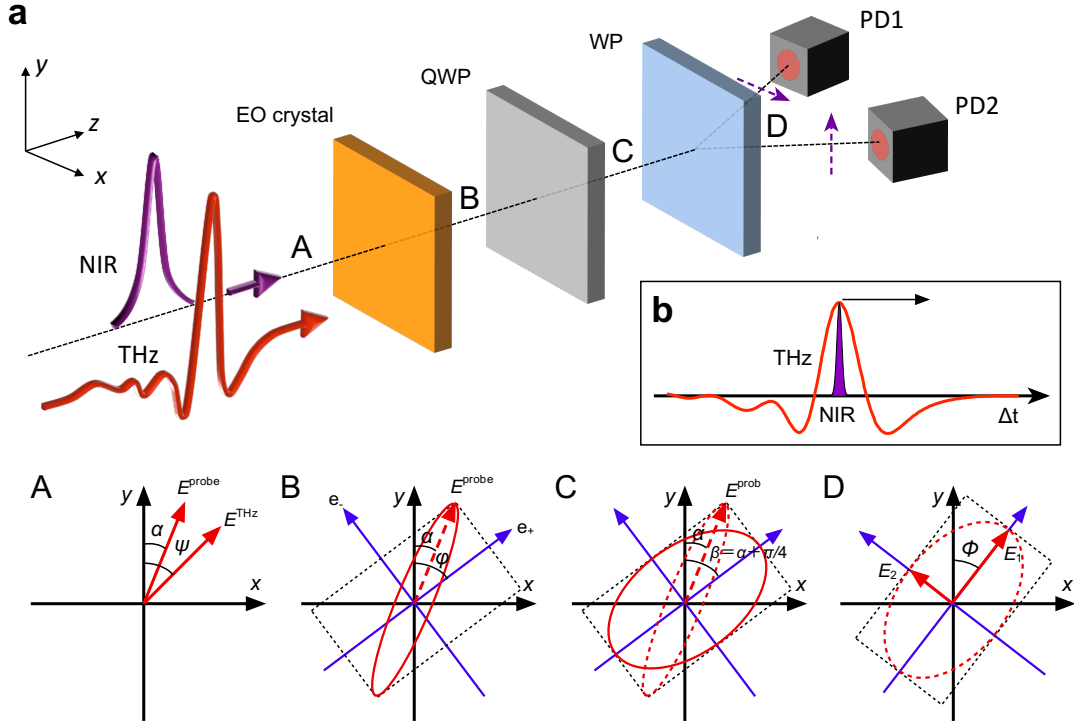
Figure 2.7 | EOS with balanced detection. (a) QWP: quarter-wave plate, WP: Wollaston prism, PD: photodiode. The polarization state of the NIR probe pulse after passing through each optical element is depicted in A-D. Finally, the difference of the two polarization components is detected at photodiodes (PD1 & PD2). **(b)** The variation of delay time Δt between the THz electric field and NIR pulse enables phase-resolved detection of the CEP-stable single-cycle THz electric field.

the polarization direction of the THz electric field and NIR probe pulse by ψ and α, respectively (Figure 2.7a, A). The principle axis of the EO crystal is denoted by φ (B). The polarization direction of the two separate orthogonal polarization components after WP is denoted by ϕ (D). The polarization state after passing through QWP (at position C in Figure 2.7a) can be described using the Jones vector **E**, given by

$$\mathbf{E}/E^{\text{probe}} = R\left(\frac{\pi}{2} - \left(\alpha + \frac{\pi}{4}\right)\right)\begin{bmatrix} e^{\frac{\pi}{4}i} & 0 \\ 0 & e^{\frac{\pi}{4}i} \end{bmatrix} R\left(-\frac{\pi}{2} - \left(\alpha + \frac{\pi}{4}\right)\right)$$

$$R\left(\frac{\pi}{2} - \varphi\right)\begin{bmatrix} e^{\frac{\delta}{2}i} & 0 \\ 0 & e^{-\frac{\delta}{2}i} \end{bmatrix} R\left(-\frac{\pi}{2} + \varphi\right) R(-\alpha)\begin{bmatrix} 0 \\ 1 \end{bmatrix}$$

$$= R\left(\frac{\pi}{2} - \beta\right) \begin{bmatrix} e^{\gamma i}\cos(\beta - \varphi)\cos(\varphi - \alpha) - ie^{-\gamma i}\sin(\beta - \varphi)\sin(\varphi - \alpha) \\ -ie^{\gamma i}\sin(\beta - \varphi)\cos(\varphi - \alpha) + e^{-\gamma i}\cos(\beta - \varphi)\sin(\varphi - \alpha) \end{bmatrix},$$

$$(2.34)$$

where E^{probe} is the electric field amplitude of the probe pulse, $R(\theta)$ is the rotation matrix, and we define $\beta \equiv \alpha + \pi/4$, $\gamma \equiv \delta/2 + \pi/4$. Then, the two orthogonal polarization components (E_1, E_2) separated by WP can be calculated using the additional rotation operation $R(\varphi - \pi/2)$, which is given by

$$\frac{1}{E^{\mathrm{probe}}}\begin{bmatrix} E_1 \\ E_2 \end{bmatrix} = R\left(\phi - \beta\right) \begin{bmatrix} e^{\gamma i}\cos(\beta - \varphi)\cos(\varphi - \alpha) - ie^{-\gamma i}\sin(\beta - \varphi)\sin(\varphi - \alpha) \\ -ie^{\gamma i}\sin(\beta - \varphi)\cos(\varphi - \alpha) + e^{-\gamma i}\cos(\beta - \varphi)\sin(\varphi - \alpha) \end{bmatrix}.$$

$$(2.35)$$

Therefore, using EOS with a balanced detection scheme, the difference signal measured by the photodiodes (PD1 & PD2) is given by

$$\Delta I/I^{\mathrm{probe}} = \frac{|E_1|^2 - |E_2|^2}{|E^{\mathrm{probe}}|^2}$$

$$= \frac{1}{2}(1 - \cos\delta)\sin[4(\varphi - \alpha)]\sin[2(\phi - \alpha)] - \sin\delta\sin[2(\varphi - \alpha)]\cos[2(\phi - \alpha)]$$

$$(2.36)$$

In the case of $\phi = \alpha$, equation (2.36) can be written as

$$\Delta I/I^{\mathrm{probe}} = -\sin\delta\sin[2(\varphi - \alpha)]. \qquad (2.37)$$

Finally, by taking equations (2.33) and (2.37) into account, the detection sensitivity of EOS is maximized when $(\alpha, \psi, \varphi, \phi)$ equals $(0,\ \pi/2,\ \pi/4,\ 0)$ or $(\pi/2,\ \pi/2,\ \pi/4,\ \pi/2)$, and, in such cases, the amplitude of the THz electric field is determined by

$$E^{\mathrm{THz}} = \sin^{-1}\left(\frac{\Delta I}{I^{\mathrm{probe}}}\right)\frac{2\pi l\gamma_{41}n^3}{\lambda}. \qquad (2.38)$$

As shown in Figure 2.7b, the complete THz electric field waveform can be temporally mapped out by delaying the NIR probe pulse with respect to the THz pulse.

2.4 THz time-domain spectroscopy

THz time-domain spectroscopy (THz-TDS) is a powerful spectroscopic technique used to investigate the properties of matter in the far-infrared region. In conventional Fourier transform infrared spectroscopy (FT-IR), Kramers-Kronig relations are used to deduce a complex refractive index because FT-IR is only sensitive to the amplitude. In contrast, THz-TDS measures coherent THz pulses in the time-domain with the absolute resolution of the amplitude and phase as shown in Section 2.3. Therefore, THz-TDS is able to obtain the complex refractive index without suffering from multiple reflections and Kramers-Kronig relations which require an ultra-broadband spectrum (in principle, $0 - \infty$ THz). Furthermore, the ultrafast dynamics of excited states can be probed using optical-pump THz-probe spectroscopy in a variety of systems [38].

In the following section, we describe the method to calculate a complex dielectric constant in transmission geometry which we used to investigate the nonlinear behavior of electrons in ultrathin Au films (Chapter 3).

2.4.1 Optical constants of a free-standing film

In the transmission geometry, multiple reflections at an air-sample interface arrive at a detector with certain time intervals determined by the thickness and refractive index of the sample. In the case of a thick sample, multiple reflections are completely separated in time, whereas a superimposed pulse is detected with a thin sample.
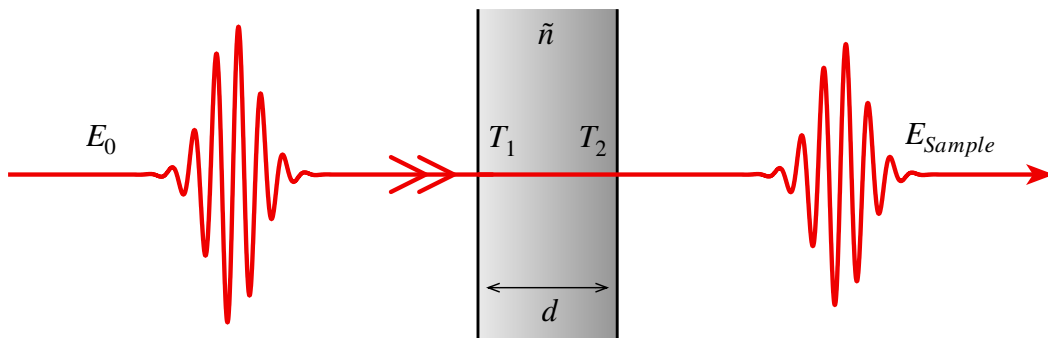
Figure 2.8 | Transmission of a free-standing thick film without multiple reflections.

We now derive the optical constants of a free-standing film which is sufficiently thick to separate multiple reflections as, schematically illustrated in Figure 2.8. The amplitude and phase of the THz pulse transmitted through a sample of thickness d is given by

$$E_{Sample} = E_0 T_1 T_2 \exp(ikd).$$ (2.39)

Using the complex refractive index of the film $\tilde{n}$ ($= n + i\kappa$), the transmittance of the THz pulse at the interface is given, using Fresnel equations, by

$$T_1 = \frac{2}{\tilde{n} + 1},$$ (2.40)

$$T_2 = \frac{2\tilde{n}}{\tilde{n} + 1}.$$ (2.41)

On the other hand, the THz pulse which propagates through a vacuum over distance d can be written as

$$E_{Reference} = E_0 \exp(ik_0 d).$$ (2.42)

The complex transmittance of the free-standing film is given by

$$\frac{E_{Sample}}{E_{Reference}} = T_1 T_2 \exp\{i(k - k_0)d\}$$

$$= \frac{4\tilde{n}}{(\tilde{n} + 1)^2} \exp\left(i\frac{\tilde{n} - 1}{c}\omega d\right),$$ (2.43)

where c is the speed of light, and ω is the angular frequency. In the actual experiment, we can obtain both the amplitude and phase of the transmittance: $T \exp(i\theta)$. Therefore, equation (2.43) can be rewritten, using natural logarithms, as

$$\ln T + i\theta = \ln\left|\frac{4\tilde{n}}{(\tilde{n} + 1)^2}\right| + i\operatorname{Arg}\left(\frac{4\tilde{n}}{(\tilde{n} + 1)^2}\right) - \frac{\kappa\omega}{c}d + i\frac{(n - 1)\omega}{c}d.$$ (2.44)

By equating real and imaginary parts, the complex refractive index is given by

$$n = 1 + \frac{c}{\omega d}\left(\theta - \operatorname{Arg}\left(\frac{4\tilde{n}}{(\tilde{n} + 1)^2}\right)\right),$$ (2.45)

$$\kappa = -\frac{c}{\omega d}\left(\ln T - \ln \left| \frac{4\tilde{n}}{(\tilde{n}+1)^2} \right| \right). \tag{2.46}$$

Moreover, the complex dielectric constant $\tilde{\epsilon}$ ($= \epsilon_1 + i\epsilon_2$) can be calculated using $\tilde{\epsilon} = \tilde{n}^2$, and given by

$$\epsilon_1 = n^2 - \kappa^2, \tag{2.47}$$

$$\epsilon_2 = 2n\kappa. \tag{2.48}$$

2.4.2   Optical constants of a thin film on the substrate

In this section, we will derive optical constants of a thin film deposited on the substrate which is transparent with respect to the THz pulses. A system having a nanometer scale thickness thin film and a sub-millimeter scale thickness supporting substrate is often investigated in THz-TDS, including our work on ultrathin Au films (described in Chapter 3). As shown in Figure 2.8, individual multiple reflections cannot be separated in the time-domain in this case, and thus the amplitude and phase of the THz pulse transmitted through a thin film of thickness d and a substrate of thickness D is given by
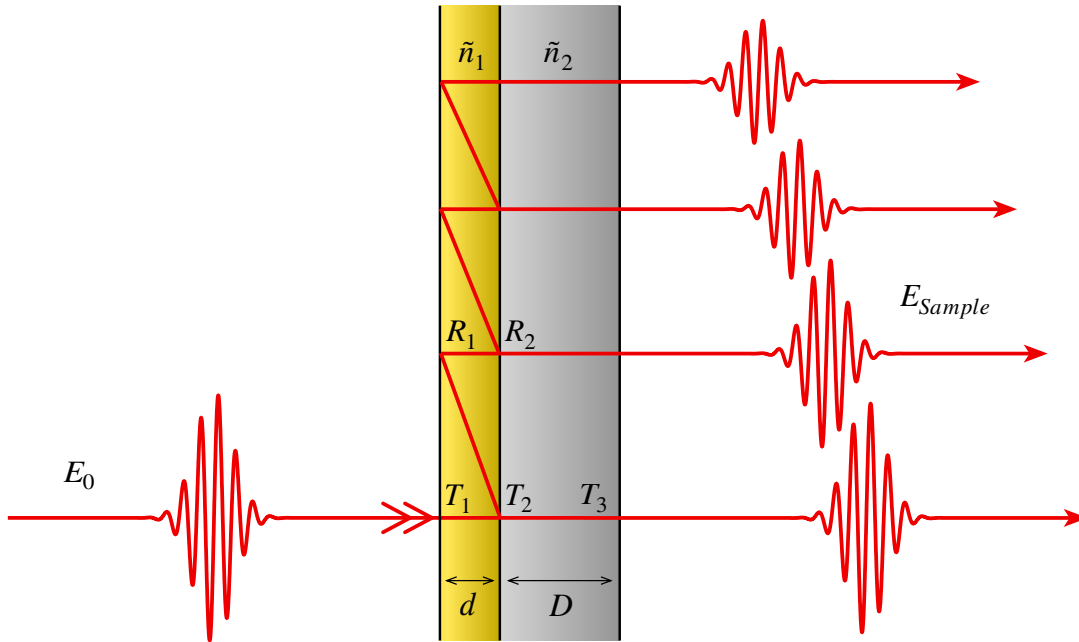
Figure 2.9 | Transmission of a thin film on the substrate with multiple reflections.

$$E_{Sample}$$

$$= E_0 T_1 T_2 \exp(ik_1 d)\left(1 + R_1 R_2 \exp(2ik_1 d) + R_1^2 R_2^2 \exp(4ik_1 d) + \cdots \right) T_3 \exp(ik_2 D)$$

$$= E_0 \frac{T_1 T_2 \exp(ik_1 d)}{1 - R_1 R_2 \exp(2ik_1 d)} T_3 \exp(ik_2 D). \tag{2.49}$$

Using the complex refractive index of the thin film $\tilde{n}_1$ ($= n_1 + i\kappa_1$), and the substrate $\tilde{n}_2$ ($= n_2 + i\kappa_2$), the transmittance and reflectance of the THz pulse at the interface is given, using Fresnel equations, by

$$T_1 = \frac{2}{\tilde{n}_1 + 1},$$

$$T_2 = \frac{2\tilde{n}_1}{\tilde{n}_1 + \tilde{n}_2},$$

$$T_3 = \frac{2\tilde{n}_2}{\tilde{n}_2 + 1},$$

$$R_1 = \frac{\tilde{n}_1 - 1}{\tilde{n}_1 + 1},$$

$$R_2 = \frac{\tilde{n}_1 - \tilde{n}_2}{\tilde{n}_1 + \tilde{n}_2}. \tag{2.50}$$

On the other hand, the THz pulse which propagates through a vacuum over a distance d and a substrate of thickness D can be written as

$$E_{Reference} = E_0 T_4 \exp(ik_0 d) T_3 \exp(ik_2 D), \tag{2.51}$$

where T_4 is the transmittance at the substrate-air interface, which is

$$T_4 = \frac{2}{\tilde{n}_2 + 1}. \tag{2.52}$$

The complex transmittance of the thin film on the substrate is given by

$$\frac{E_{Sample}}{E_{Reference}}$$

$$= \frac{T_1 T_2}{T_4} \frac{\exp\left\{i(k_1 - k_0)d\right\}}{1 - R_1 R_2 \exp(2ik_1 d)}$$

$$= \frac{2\tilde{n}_1(\tilde{n}_2 + 1)}{(\tilde{n}_1 + 1)(\tilde{n}_1 + \tilde{n}_2) - (\tilde{n}_1 - 1)(\tilde{n}_1 - \tilde{n}_2)\exp(2i\tilde{n}_1 \omega d/c)} \exp\left\{i\frac{(\tilde{n}_1 - 1)\omega}{c}d\right\}.$$

$$(2.53)$$

When d is sufficiently small compared to the wavelength of THz pulses, polarization within the film can be assumed to be constant, thus the following approximate expression can be applied to equation (2.53),

$$d \to 0, \tag{2.54}$$

$$\tilde{n}_1^2 d = \text{const}. \tag{2.55}$$

In this case, equation (2.53) simplifies to

$$\frac{E_{Sample}}{E_{Reference}} = \tilde{T}(\omega) \simeq \frac{\tilde{n}_2 + 1}{\tilde{n}_2 + 1 - i\omega\tilde{n}_1^2 d/c}. \tag{2.56}$$

Therefore, the complex dielectric constant $\tilde{\epsilon}$ can be calculated using $\tilde{\epsilon} = \tilde{n}^2$, and given by

$$\tilde{\epsilon} = \frac{i(\tilde{n}_2 + 1)c}{\omega d} \frac{1 - \tilde{T}(\omega)}{\tilde{T}(\omega)}. \tag{2.57}$$

2.5 Carrier-envelope phase control of the single-cycle THz pulse

The CEP control of electrons has been extensively studied using few-cycle near-infrared pulses in a variety of systems [39,40]. In the near-infrared region, CEP control is achieved by inserting a disperse medium in the laser beam path. When we only consider the primary of the reflective index dispersion $dn/d\lambda$, the phase velocity v_{ph} and the group velocity v_g of the transmitted laser pulse is represented as

$$v_{ph} = \frac{c}{n}, \tag{2.58}$$

$$v_g = \frac{c}{n - dn/d\lambda}. \tag{2.59}$$

Therefore, the CEP shift is given by

$$\phi_{CEP} = 2\pi L \frac{dn}{d\lambda}, \tag{2.60}$$

where L is the propagating distance in the disperse medium. For example, in the near-infrared region, a pair of SiO_2 wedges can produce desirable CEPs by changing the propagating distance between a few μm and tens of μm. However, in the THz spectral range (0.1–3 THz), no suitable dispersive medium exists. Therefore, despite the expectation that intense THz pulses should be able to drive ultrafast nonlinear processes due to their characteristics (that is, highly intense, long-wavelength, passively phase-locked, and single-cycle pulse), the CEP control of electrons has not been reported so far. In the following section, we will describe the method to control the CEP of single-cycle THz pulses using the Gouy phase shift [41–43] and broadband CEP shifter [44].

2.5.1 The Gouy phase shift

The Gouy phase shift is the well-known phenomenon that occurs when a tightly focused lightwave experiences a phase shift as it passes through its focus. For a line focus using a cylindrical lens, a phase shift of $\pi/2$ occurs while propagating from $-\infty$ to ∞, whereas a phase shift of π occurs for a point focus using a spherical lens. Although the Gouy phase shift was discovered more than 100 years ago, a simple and satisfying physical interpretation of the phenomenon took a long time to develop. In this section, we describe a simple explanation of this phase anomaly, developed by S. Feng *et al.* in 2001 [43], based on the uncertainty principle.

Consider a monochromatic wave propagating along the *z* axis with frequency ω and wave number $k = c/\omega$. In the case of an infinite plane wave, the momentum is directed along the *z* axis with no transverse component. The spread in transverse momentum is zero, and thus the spread in transverse position is infinite because of the uncertainty principle. On the other hand, a finite beam has a spread in transverse momentum because it is made up of an angular spectrum of plane waves obtainable by means of a Fourier transform.

The transverse momentum is related to the wave number by

$$k^2 = k_x^2 + k_y^2 + k_z^2, \tag{2.61}$$

where k_x, k_y, and k_z are the wave vector components along the coordinate axes. Using expectation values defined by

$$\langle \xi \rangle \equiv \frac{\int_{-\infty}^{+\infty} \xi \, |f(\xi)|^2 \, \mathrm{d}\xi}{\int_{-\infty}^{+\infty} |f(\xi)|^2 \, \mathrm{d}\xi}, \tag{2.62}$$

where $f(\xi)$ is the distribution of the ξ, an effective axial propagation constant for the finite beam through the second moment can be defined as

$$\bar{k}_z \equiv \frac{\langle k_z^2 \rangle}{k} = k - \frac{\langle k_x^2 \rangle}{k} - \frac{\langle k_y^2 \rangle}{k} \,. \tag{2.63}$$

This effective propagation constant is related to the overall propagation phase $\phi(z)$ along the z axis by the following equation [45]:

$$\bar{k}_z \equiv \frac{\partial \phi(z)}{\partial z} \,. \tag{2.64}$$

The first term of equation (2.63) gives the phase of the infinite plane wave propagating along the z axis, while the last two terms give rise to the Gouy phase shift:

$$\phi_G = -\frac{1}{k} \int^z \left(\langle k_x^2 \rangle + \langle k_y^2 \rangle \right) \mathrm{d}z \,. \tag{2.65}$$

Therefore, the Gouy phase shift can be interpreted as the expectation value of the axial phase shift owing to the transverse momentum spread.

We now consider the case of a monochromatic beam with a Gaussian transverse distribution given by

$$f(x,y) = \sqrt{\frac{2}{\pi}} \frac{1}{w(z)} \exp\left[-\frac{x^2 + z^2}{w^2(z)} \right], \tag{2.66}$$

$$w^2(z) = w_0^2 \left[1 + \left(\frac{z}{z_R} \right)^2 \right], \tag{2.67}$$

where equation (2.67) is used to calculate the beam radius, w_0 is the smallest

a

b

π phase shift
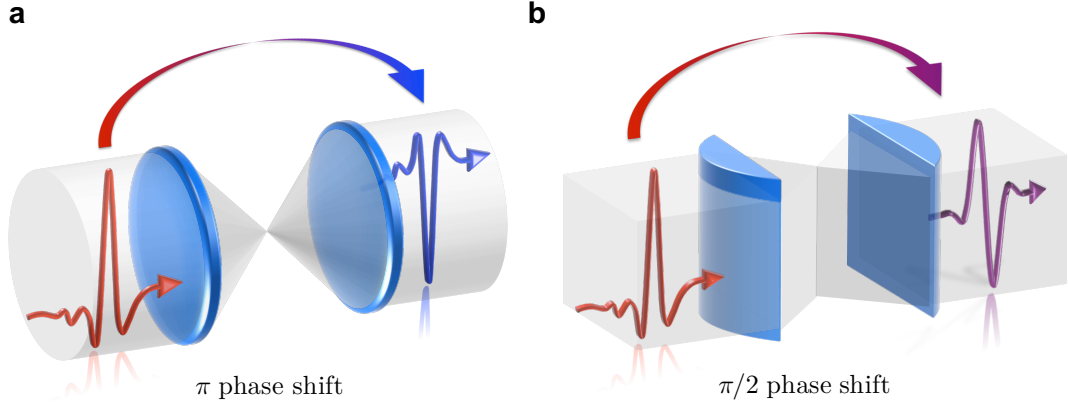
$\pi/2$ phase shift

Figure 2.10 | CEP control of the single-cycle THz electric field via the Gouy phase shift. (a) The CEP shift of π induced by point focus using a pair of spherical lenses. **(b)** The CEP shift of $\pi/2$ induced by line focus using a pair of cylindrical lenses.

spot size at $z = 0$, and z_R is the Rayleigh length (defined by $z_R = \pi w_0^2/\lambda$, where λ is the wavelength). The distribution of transverse wave vector components (the angular spectrum of plane waves) is given by the Fourier transformation:

$$\tilde{F}(k_x, k_y) = \frac{1}{2\pi} \int_{-\infty}^{+\infty} \int_{-\infty}^{+\infty} f(x,y) \exp(-ik_x x - ik_y y) dx dy$$

$$= \frac{w(z)}{\sqrt{2\pi}} \exp\left[-\frac{w^2(z)}{4}(k_x^2 + k_y^2)\right]. \tag{2.68}$$

Both functions $f(x,y)$ and $\tilde{F}(k_x, k_y)$ are normalized, and thus, using equation (2.62), we have

$$\langle k_x^2 \rangle = \int_{-\infty}^{+\infty} \int_{-\infty}^{+\infty} k_x^2 |\tilde{F}(k_x, k_y)|^2 dk_x dk_y = \frac{1}{w^2(z)} = \langle k_y^2 \rangle. \tag{2.69}$$

Therefore, the Gouy phase shift is given by

$$\phi_G = -\frac{1}{k} \int^z \left(\langle k_x^2 \rangle + \langle k_y^2 \rangle\right) dz = -\frac{2}{k} \int^z \frac{1}{w^2(z)} dz. \tag{2.70}$$

The factor of 2 in equation (2.70) arises from the number of transverse dimensions, with each dimension contributing $1/w^2(z)$ to the mean-square transverse momentum. This is why the Gouy phase shift of line focusing ($\pi/2$)

is half that of point focusing (π). Performing the integration in equation (2.70), we obtain the standard result for the Gouy phase shift

$$\phi_G = -\arctan(z/z_R), \qquad (2.71)$$

which gives a phase shift of π by point focus while propagating from $-\infty$ to ∞.

The Gouy phase shift was shown to exist for any wave, including acoustic waves and THz pulses [41,42]. As shown in Figure 2.9a, b, we inserted THz lenses in the beam path for the CEP control of THz pulses instead of using the disperse medium. This scheme enabled us to generate the CEP controlled single-cycle THz pulses with different CEPs of $\phi_{\text{CEP}} = 0$, $\pi/2$, and π. Using this THz source, we succeeded in demonstrating real-space coherent manipulation of electron tunneling, as described in Chapter 4.

2.5.2 Carrier-envelope phase shifter

Although Gouy phase manipulation enables CEP control of single-cycle THz pulses, several aspects of this technique prevent perfect control of CEP:

4. The value of CEPs is restricted to $\phi_{\text{CEP}} = 0$, $\pi/2$, and π.
5. Distortion of the intensity spectrum is easily introduced because geometrical imperfections in the lenses may result in focusing and collimating.
6. The large group delay during the CEP control is unavoidable.

Recently, Y. Kawada *et al.* invented a carrier-envelope phase shifter that provides perfect control of the CEP of broadband THz pulses [44] and is free from the above concerns. The CEP shifter is composed of broadband prism-type wave plates which were developed by the same group in 2014 [46]. This achromatic wave plate is based on Fresnel's rhomb and made from silicon. The phase retardation between p-polarized light and s-polarized light induced by total internal reflection is only determined by the incident angle and the refractive index of the silicon. Therefore, the wave plate works perfectly for the ultra-broadband spectrum from 0.5 to 4.5 THz [46], in contrast to other methods [47–50], which are limited to a narrow frequency window.

Figure 2.11 shows the configuration of the CEP shifter, which comprises three optical elements: a first quarter-wave plate (QWP), a half-wave plate (HWP), and a second QWP. The second QWP can be replaced by a wire grid polarizer
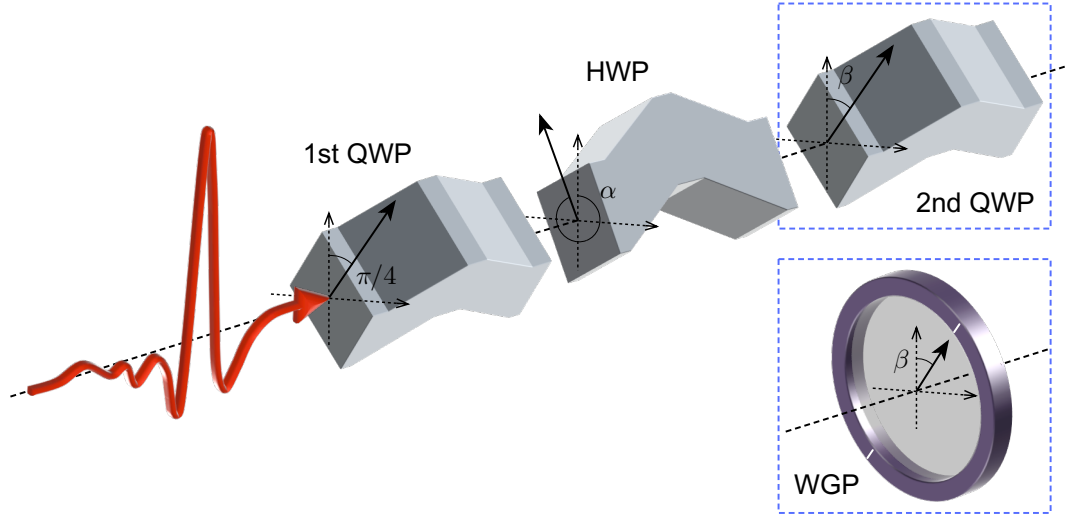
Figure 2.11 | CEP control of the single-cycle THz electric field via the CEP shifter. QWP: quarter-wave plate, HWP: half-wave plate, WGP: wire grid polarizer. The azimuth angles of the HWP and the second QWP are α and β, respectively. The second QWP can be replaced by a WGP. Any desired CEP value can be chosen by rotating the HWP.

(WGP). The azimuth angle of the first QWP is set to $\pi/4$ with respect to the polarization direction of the incident THz pulse. On the other hand, the azimuth angles of the HWP and the second QWP may vary, and are denoted by α and β, respectively. The function of each of the optical elements can be explained as follows. The first QWP converts the polarization of the THz pulse so that it is circularly polarized. Then, the HWP rotates the azimuth angle of the circularly polarized pulse without distorting the pulse shape. Finally, the second QWP converts the circularly polarized pulse into a linearly polarized pulse and determines the polarization direction of the output THz pulse. The function of the second QWP can be replaced by the WGP in order to eliminate polarized components in a particular direction. Any CEP value for the output THz pulse can be chosen by an appropriate rotation of HWP.

We now quantitatively describe the function of the CEP shifter using Jones matrices. When we use the second QWP for the third optical element, the output THz pulse L_{out} is given by

$$L_{\text{out}} = R(-\beta)C_{1/4}R(\beta)R(-\alpha)C_{1/2}R(\alpha)R(-\pi/4)C_{1/4}R(\pi/4)L_{\text{in}}, \qquad (2.72)$$

where L_{in} is the input THz pulse, R is the rotation matrix, and C is the matrix for a phase retarder. The subscripts denote the amount of phase retardation:

1/2 denotes $\lambda/2$ and 1/4 denotes $\lambda/4$. Note that equation (2.72) holds for the entire spectrum of the single-cycle THz electric field generated by optical rectification in LiNbO$_3$ because of broadband wave plates. Therefore, the phase shift calculated using equation (2.72) represents the amount of CEP shift. With an initial phase ϕ_{CEP0}, the linear polarized input THz pulse is described by

$$L_{\text{in}} = \begin{pmatrix} \exp(i\phi_{CEP_0}) \\ 0 \end{pmatrix}. \tag{2.73}$$

By substituting equation (2.73) into equation (2.72), we have

$$L_{\text{out}} = \begin{bmatrix} \cos\beta & -\sin\beta \\ \sin\beta & \cos\beta \end{bmatrix} \begin{bmatrix} 1 & 0 \\ 0 & -i \end{bmatrix} \begin{bmatrix} \cos\beta & \sin\beta \\ -\sin\beta & \cos\beta \end{bmatrix} \begin{bmatrix} \cos\alpha & -\sin\alpha \\ \sin\alpha & \cos\alpha \end{bmatrix} \begin{bmatrix} 1 & 0 \\ 0 & -1 \end{bmatrix}$$
$$\begin{bmatrix} \cos\alpha & \sin\alpha \\ -\sin\alpha & \cos\alpha \end{bmatrix} \frac{1}{\sqrt{2}} \begin{bmatrix} 1 & -1 \\ 1 & 1 \end{bmatrix} \begin{bmatrix} 1 & 0 \\ 0 & -i \end{bmatrix} \frac{1}{\sqrt{2}} \begin{bmatrix} 1 & 1 \\ -1 & 1 \end{bmatrix} \begin{bmatrix} \exp(i\phi_{CEP_0}) \\ 0 \end{bmatrix}. \tag{2.74}$$

Equation (2.74) can be simplified to

$$L_{\text{out}} = \begin{pmatrix} \cos\left(-\beta + \frac{\pi}{4}\right) \exp\left[i\left(\phi_{CEP_0} + 2\alpha - \beta - \frac{\pi}{4}\right)\right] \\ \cos\left(\beta + \frac{\pi}{4}\right) \exp\left[i\left(\phi_{CEP_0} + 2\alpha - \beta + \frac{3\pi}{4}\right)\right] \end{pmatrix}. \tag{2.75}$$

In equation (2.75), the phase difference of the two orthogonal electric fields is π, and thus the output THz pulse is linearly polarized.

Next, we will derive the polarization direction of the THz pulse by calculating the coordinate rotation angle θ for which the orthogonal electric field component vanishes. By rotating the coordinates of equation (2.75), we have

$$R(\theta)L_{\text{out}}$$
$$= \frac{1}{\sqrt{2}} \begin{bmatrix} \cos\theta \cos\left(-\beta + \frac{\pi}{4}\right)(1-i) + \sin\theta \cos\left(\beta + \frac{\pi}{4}\right)(-1+i) \\ -\sin\theta \cos\left(-\beta + \frac{\pi}{4}\right)(1-i) + \cos\theta \cos\left(\beta + \frac{\pi}{4}\right)(-1+i) \end{bmatrix} e^{i\left(\phi_{CEP_0} + 2\alpha - \beta\right)}. \tag{2.76}$$

Therefore, the polarization direction θ can be calculated using the second row

by the following equation:

$$-\sin\theta \cos\left(-\beta + \frac{\pi}{4}\right)(1-i) + \cos\theta \cos\left(\beta + \frac{\pi}{4}\right)(-1+i) = 0, \qquad (2.77)$$

and is given by

$$\theta = \beta - \frac{\pi}{4}. \qquad (2.78)$$

On the other hand, the amount of the CEP shift can be calculated by substituting equation (2.78) into the first row of equation (2.76). To do this, we simplify the first row of equation (2.76) to

$$\cos\left(\theta - \beta + \frac{\pi}{4}\right)e^{i\left(\phi_{CEP_0} + 2\alpha - \beta - \frac{\pi}{4}\right)}, \qquad (2.79)$$

thus the CEP of the output THz pulse is given by

$$\exp i\left(\phi_{CEP_0} + 2\alpha - \beta - \frac{\pi}{4}\right). \qquad (2.80)$$

Finally, the amount of the CEP shift $\Delta\phi_{CEP}$ induced by the CEP shifter is given by

$$\Delta\phi_{CEP} = \phi_{CEP} - \phi_{CEP_0} = 2\alpha - \beta - \frac{\pi}{4}. \qquad (2.81)$$

Equation (2.78) tells us that the polarization angle is determined by β, while the CEP shift depends on both α and β. In practice, the polarization direction is first determined by rotating the second QWP, and then the CEP is controlled by rotating the HWP.

When we used the WGP for the third optical element, equation (2.78) becomes

$$\theta = \beta, \qquad (2.82)$$

and the amount of the CEP shift is the same as the case where a QWP is used as the third optical component (equation (2.81)). In the experiment (as we describe in Chapter 5) we used the WGP to make the CEP shifter compact in order to develop the Mach-Zehnder interferometer.

As shown in equation (2.81), using the CEP shifter, any CEP values can be precisely chosen, in contrast to the use of Gouy phase manipulation. In addition, because of the broadband character of the wave plates, the CEP can be controlled without any distortion in the intensity spectrum. Furthermore, in the CEP shifter, propagation length of the THz pulse is always constant, and thus, the output pulse is free from extra delay while changing the CEP. Using this perfectly controlled single-cycle THz electric field, we were able to demonstrate in-situ tailoring of THz near field in a single tunnel junction, as described in Chapter 5.

2.6   Scanning tunneling microscopy

Since the invention of scanning tunneling microscopy (STM) by Binning and Rohrer in 1981 [51,52], for which they were awarded the Nobel prize in 1986, STM has become a versatile tool in nanoscience and nanotechnology for visualizing the electronic wave function at the atomic scale (sub-angstrom). The way in which STM operates is entirely different from that of a conventional optical microscope. In an optical microscope, the spatial resolution is limited by the diffraction limit of the light, which is determined by the wavelength (a few hundred nanometers for the visual light), thereby making it unsuitable at the atomic scale. On the other hand, STM "sees" the object by the tunnel current through an atomically sharp metallic nanotip. Because of the highly nonlinear nature of electron tunneling, STM is capable of visualizing individual atoms, which is essential for condensed matter research. Furthermore, STM enables access to the local density of states (DOS) by scanning the voltage at a fixed position. In this section, we will briefly introduce the basic principles of STM. Further information about and more detailed descriptions of STM can be found in common textbooks [53,54].

2.6.1   Working principle of STM

When a positive bias voltage V is applied to the sample, the Fermi level of the sample is decreased by eV, causing electrons to flow from the occupied states of the tip into the empty states of the sample through quantum tunneling, as shown in Figure 2.12. The tunnel current is exponentially dependent on the
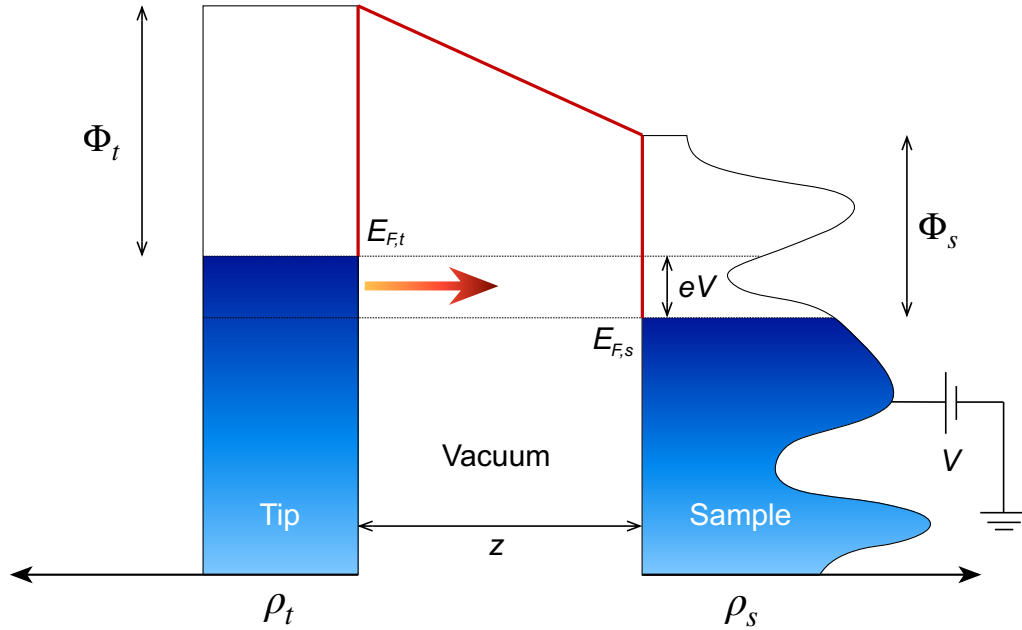
Figure 2.12 | Schematic of a tunnel junction in the STM. Φ_t: work function of the tip, Φ_s: work function of the sample, ρ_t: DOS of the tip, ρ_s: DOS of the sample, $E_{F,t}$: Fermi level of the tip, $E_{F,s}$: Fermi level of the sample. A positive bias voltage V is applied to the sample. The electrons flow from the occupied states of the tip into the empty states of the sample through quantum tunnelling. DOS of the tip is assumed to be constant. The increase in the tunnel current is proportional to the number of newly accessible empty states, which is proportional to the DOS at the given bias voltage.

tip-sample distance z, given by

$$I(z) = I(0)\exp(-2\kappa z), \tag{2.83}$$

$$\kappa = \frac{\sqrt{m\left(\Phi_t + \Phi_s - eV\right)}}{\hbar}, \tag{2.84}$$

where κ is the decay constant, m is the electron mass, $\hbar$ is the Planck constant, and Φ_t and Φ_s are the work functions of the tip and sample, respectively. A typical value of the work function is about 5 eV, which gives a value of the decay constant of 11 nm^{-1}. According to equation (2.83), the tunnel current decreases by an order of magnitude when the tip-sample distance is increased by just o.1 nm. A more realistic model of the tunnel current, including the effect of an image force using the WKB approximation, will be described in Chapter 4.
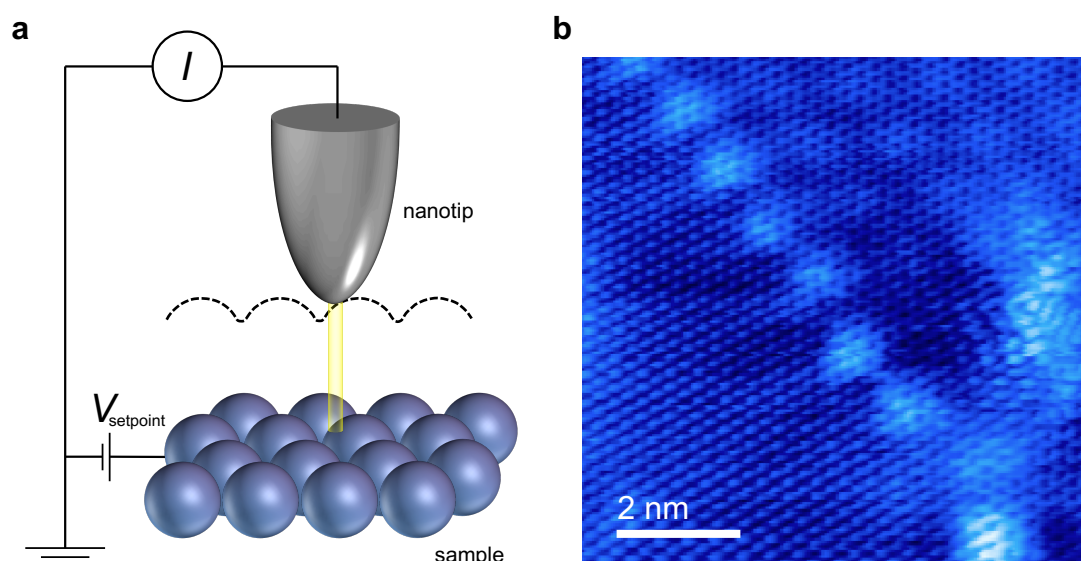
Figure 2.13 | Topographic imaging with an STM. (a) Schematic illustration of imaging the sample surface under constant-current mode. A metallic tip is placed above a conducting sample surface. The tip and sample should be in contact electronically. The tip position is precisely controlled using piezoelectric elements. The tunnel current can be detected when the tip brought very close to the surface ($<$ 1 nm). **(b)** Atomic-scale topographic image of highly oriented pyrolytic graphite obtained by constant-current mode using a commercial ultra-high-vacuum STM. The quantum interference between the top layer and second layer was observed as a *moiré pattern. The image was recorded at a setpoint of 0.5 nA at 500 mV.*

The exponential distance dependence of the tunnel current is key to controlling the tip position with sub-atomic precision. Figure 2.13a schematically illustrates the imaging of a sample surface in constant-current mode. The measured tunnel current is converted to a voltage by the current amplifier, which is then compared with a reference value (setpoint). The difference is amplified in order to drive piezo-electric elements that enable three-dimensional control of the tip movement with extremely high accuracy. The phase of the amplifier is set to provide negative feedback: when the value of the tunnel current is larger than the reference value, the tip-sample distance (z) is increased to minimize the difference, and vice versa. As the tip scans over the xy plane, a two-dimensional array of z positions, representing a counter plot of the equal tunnel current surface is obtained. In another operational mode, called constant-height mode, the tip-sample distance is kept constant while the tunnel current is recorded during the tip scan over the xy plane. The

STM topographic image recorded in constant-current mode is shown in Figure 2.13b.

2.6.2 Scanning tunneling spectroscopy

The tunnel current is not only dependent on the tip-sample distance, but is also sensitive to the applied bias voltage *V*. By scanning the voltage, the STM is able to locally detect the DOS as a function of energy with high sensitivity near the Fermi energy. This unique capability makes STM a powerful and exciting tool for physicists and chemists. Although formulation of the tunnel current can be treated in many ways, Bardeen's theory [55] provides a sound basis for understanding the connection between the tunnel current and the DOS of the tunnel junction. In this model, the tunnel current is obtained by the finite overlap of the wave functions of the tip and sample. The resulting current at a voltage *V* can be evaluated by summing over all relevant states based on Fermi's golden rule, and given by

$$I = \frac{4\pi e}{\hbar} \int_{-\infty}^{\infty} \left[f\left(E_F - eV + \epsilon\right) - f\left(E_F + \epsilon\right) \right]$$
$$\times \rho_s \left(E_F - eV + \epsilon\right) \rho_t \left(E_F + \epsilon\right) |M|^2 d\epsilon, \qquad (2.85)$$

where e is the electron charge, $f(E)$ is the Fermi distribution function, E_F is the Fermi energy, ρ_s and ρ_t are the DOS of the sample and tip, respectively, and M is the tunneling matrix element. This equation can be simplified by assuming that the magnitude of the tunneling matrix element is constant in the region of interest, and is given by

$$I \propto \int_0^{eV} \rho_s \left(E_F - eV + \epsilon\right) \rho_t \left(E_F + \epsilon\right) d\epsilon. \qquad (2.86)$$

The situation described by equation (2.86) is represented in Figure 2.12. Under the conditions that the DOS of the tip is flat and the temperature is sufficiently low, the DOS of the sample is proportional to the differential conductance dI/dV:

$$\frac{dI}{dV} \propto \rho_s \left(E_F - eV\right). \qquad (2.87)$$

In scanning tunneling spectroscopy (STS), local DOS can be obtained with resolution at atomic scales by measuring the differential conductance. The energy resolution of STS is limited by thermal broadening due to the Fermi distribution. In many cases, the tip DOS cannot be made completely flat, and especially, great care must be taken with a negative bias voltage because the energy spectrum of the tip plays a leading role. Using STS, specific energy levels can be accessed in the real-space. Beautiful applications of this technique include LOMO and HOMO imaging of a single molecule [56], and the imaging of a superconducting gap using quasi-particle interference [57]. This unique capability makes STM an indispensable tool for condensed matter research. For the measurements in this thesis, presented in Chapters 4 and 5, we used a Pt-Ir nanotip and a highly oriented pyrolytic graphite (HOPG) for the sample. In this case, THz-field-induced electron tunneling is explained very well with the flat DOS for both tip and sample.

References in chapter 2

[1]   C. Rullière, Femtosecond Laser Pulses Principles and Experiments Second Edition, Springer (2005)

[2]   J.-C. Diels, W. Rudolph., Ultrashort Laser Pulse Phenomena: Fundamentals, Techniques, and Applications on a Femtosecond Time Scale Second Edition, Elsevier (2006)

[3]   T. Udem, R. Holzwarth, T.W. Hänsch, Optical frequency metrology, Nature. 416 (2002) 233–237.

[4]   M. Fischer, N. Kolachevsky, M. Zimmermann, R. Holzwarth, T. Udem, T.W. Hänsch, M. Abgrall, J. Grünert, I. Maksimovic, S. Bize, H. Marion, F.P. Dos Santos, P. Lemonde, G. Santarelli, P. Laurent, A. Clairon, C. Salomon, M. Haas, U.D. Jentschura, C.H. Keitel, New Limits on the Drift of Fundamental Constants from Laboratory Measurements, Phys. Rev. Lett. 92 (2004) 230802.

[5]   S.A. Diddams, L. Hollberg, V. Mbele, Molecular fingerprinting with the resolved modes of a femtosecond laser frequency comb, Nature. 445 (2007) 627–630.

[6]   T. Steinmetz, T. Wilken, C. Araujo-Hauck, R. Holzwarth, T.W. Hansch, L. Pasquini, A. Manescau, S. D'Odorico, M.T. Murphy, T. Kentischer, W. Schmidt, T. Udem, Laser Frequency Combs for Astronomical Observations, Science 321 (2008) 1335–1337.

[7]   A.D. Ludlow, M.M. Boyd, J. Ye, E. Peik, P.O. Schmidt, Optical atomic clocks, Rev. Mod. Phys. 87 (2015) 637–701.

[8]   D. Strickland, G. Mourou, Compression of amplified chirped optical pulses, Opt. Commun. 56 (1985) 219–221.

[9]   M. Tonouchi, Cutting-edge terahertz technology, Nat. Photonics. 1 (2007) 97–105.

[10]   D.H. Auston, K.P. Cheung, P.R. Smith, Picosecond photoconducting Hertzian dipoles, Appl. Phys. Lett. 45 (1984) 284–286.

[11]   S. Matsuura, M. Tani, K. Sakai, Generation of coherent terahertz radiation by photomixing in dipole photoconductive antennas, Appl. Phys. Lett. 70 (1997) 559–561.

[12] A. Dreyhaupt, S. Winnerl, M. Helm, T. Dekorsy, Optimum excitation conditions for the generation of high-electric-field terahertz radiation from an oscillator-driven photoconductive device., Opt. Lett. 31 (2006) 1546–1548.

[13] P.Y. Han, M. Tani, F. Pan, X.C. Zhang, Use of the organic crystal DAST for terahertz beam applications, Opt. Lett. 25 (2000) 675.

[14] C.P. Hauri, C. Ruchert, C. Vicario, F. Ardana, Strong-field single-cycle THz pulses generated in an organic crystal, Appl. Phys. Lett. 99 (2011) 161116.

[15] A. Sell, A. Leitenstorfer, R. Huber, Phase-locked generation and field-resolved detection of widely tunable terahertz pulses with amplitudes exceeding 100 MV/cm., Opt. Lett. 33 (2008) 2767–2769.

[16] F. Junginger, A. Sell, O. Schubert, B. Mayer, D. Brida, M. Marangoni, G. Cerullo, A. Leitenstorfer, R. Huber, Single-cycle multiterahertz transients with peak fields above 10 MV/cm., Opt. Lett. 35 (2010) 2645–7.

[17] K.L. Yeh, M.C. Hoffmann, J. Hebling, K.A. Nelson, Generation of 10 μJ ultrashort terahertz pulses by optical rectification, Appl. Phys. Lett. 90 (2007).

[18] H. Hirori, A. Doi, F. Blanchard, K. Tanaka, Single-cycle terahertz pulses with amplitudes exceeding 1 MV/cm generated by optical rectification in $LiNbO_3$, Appl. Phys. Lett. 98 (2011) 091106.

[19] C. Ruchert, C. Vicario, C.P. Hauri, Scaling submillimeter single-cycle transients toward megavolts per centimeter field strength via optical rectification in the organic crystal OH1, Opt. Lett. 37 (2012) 899.

[20] C. Vicario, B. Monoszlai, C.P. Hauri, GV/m single-cycle terahertz fields from a laser-driven large-size partitioned organic crystal, Phys. Rev. Lett. 112 (2014) 213901.

[21] M. Shalaby, C.P. Hauri, Demonstration of a low-frequency three-dimensional terahertz bullet with extreme brightness, Nat. Commun. 6 (2015) 5976.

[22] F. Blanchard, L. Razzari, H.C. Bandulet, G. Sharma, R. Morandotti, J.C. Kieffer, T. Ozaki, M. Reid, H.F. Tiedje, H.K. Haugen, F.A Hegmann, Generation of 1.5 μJ single-cycle terahertz pulses by optical rectification from a large aperture ZnTe crystal., Opt. Express. 15 (2007) 13212–13220.

[23] T. Tanabe, K. Suto, J. Nishizawa, K. Saito, T. Kimura, Tunable terahertz wave generation in the 3- to 7-THz region from GaP, Appl. Phys. Lett. 83 (2003) 237–239.

[24] C. Kübler, R. Huber, S. Tübel, A. Leitenstorfer, Ultrabroadband detection of multi-terahertz field transients with GaSe electro-optic sensors: Approaching the near infrared, Appl. Phys. Lett. 85 (2004) 3360–3362.

[25] T. Bartel, P. Gaal, K. Reimann, M. Woerner, T. Elsaesser, Generation of single-cycle THz transients with high electric-field amplitudes, Opt. Lett. 30 (2005) 2805.

[26] Y. Minami, T. Kurihara, K. Yamaguchi, M. Nakajima, T. Suemoto, High-power THz wave generation in plasma induced by polarization adjusted two-color laser pulses, Appl. Phys. Lett. 102 (2013) 041105.

[27] T. Kampfrath, M. Battiato, P. Maldonado, G. Eilers, J. Nötzold, S. Mährlein, V. Zbarsky, F. Freimuth, Y. Mokrousov, S. Blügel, M. Wolf, I. Radu, P.M. Oppeneer, M. Münzenberg, Terahertz spin current pulses controlled by magnetic heterostructures, Nat. Nanotechnol. 8 (2013) 256–260.

[28] T. Seifert, S. Jaiswal, U. Martens, J. Hannegan, L. Braun, P. Maldonado, F. Freimuth, A. Kronenberg, J. Henrizi, I. Radu, E. Beaurepaire, Y. Mokrousov, P.M. Oppeneer, M. Jourdan, G. Jakob, D. Turchinovich, L.M. Hayden, M. Wolf, M. Münzenberg, M. Kläui, T. Kampfrath, Efficient metallic spintronic emitters of ultrabroadband terahertz radiation, Nat. Photonics. 10 (2016) 483–488.

[29] H.R. Telle, G. Steinmeyer, A.E. Dunlop, J. Stenger, D.H. Sutter, U. Keller, Carrier-envelope offset phase control: A novel concept for absolute optical frequency measurement and ultrashort pulse generation, Appl. Phys. B. 69 (1999) 327–332.

[30] D.J. Jones, Carrier-Envelope Phase Control of Femtosecond Mode-Locked Lasers and Direct Optical Frequency Synthesis, Science 288 (2000) 635–639.

[31] A. Apolonski, A. Poppe, G. Tempea, C. Spielmann, T. Udem, R. Holzwarth, T.W. Hänsch, F. Krausz, Controlling the Phase Evolution of Few-Cycle Light Pulses, Phys. Rev. Lett. 85 (2000) 740–743.

[32] J. Hebling, A.G. Stepanov, G. Almási, B. Bartal, J. Kuhl, Tunable THz pulse generation by optical rectification of ultrashort laser pulses with tilted pulse fronts, Appl. Phys. B Lasers Opt. 78 (2004) 593–599.

[33] Q. Wu, X.C. Zhang, 7 terahertz broadband GaP electro-optic sensor, Appl. Phys. Lett. 70 (1997) 1784–1786.

[34] J. Hebling, G. Almasi, I. Kozma, J. Kuhl, Velocity matching by pulse front tilting for large area THz-pulse generation, Opt. Express. 10 (2002) 1161.

[35] Q. Wu, X.C. Zhang, Free-space electro-optic sampling of terahertz beams, Appl. Phys. Lett. 67 (1995) 3523.

[36] A. Leitenstorfer, S. Hunsche, J. Shah, M.C. Nuss, W.H. Knox, Detectors and sources for ultrabroadband electro-optic sampling: Experiment and theory, Appl. Phys. Lett. 74 (1999) 1516–1518.

[37] N.C.J. van der Valk, T. Wenckebach, P.C.M. Planken, Full mathematical description of electro-optic detection in optically isotropic crystals, J. Opt. Soc. Am. B. 21 (2004) 622.

[38] R. Ulbricht, E. Hendry, J. Shan, T.F. Heinz, M. Bonn, Carrier dynamics in semiconductors studied with time-resolved terahertz spectroscopy, Rev. Mod. Phys. 83 (2011) 543–586.

[39] F. Krausz, M. Ivanov, Attosecond physics, Rev. Mod. Phys. 81 (2009) 163–234.

[40] F. Krausz, M.I. Stockman, Attosecond metrology: from electron capture to future signal processing, Nat. Photonics. 8 (2014) 205–213.

[41] A.B. Ruffin, J.F. Whitaker, S. Feng, H.G. Winful, J.V. Rudd, Direct observation of the Gouy phase shift with single-cycle terahertz pulses, Phys. Rev. Lett. 83 (1999) 3410–3413.

[42] R.W. McGowan, R.A. Cheville, D. Grischkowsky, Direct observation of the Gouy phase shift in THz impulse ranging, Appl. Phys. Lett. 76 (2000) 670.

[43] S. Feng, H.G. Winful, Physical origin of the Gouy phase shift., Opt. Lett. 26 (2001) 485–487.

[44] Y. Kawada, T. Yasuda, H. Takahashi, Carrier envelope phase shifter for broadband terahertz pulses, Opt. Lett. 41 (2016) 986.

[45] H.A. Haus, Waves and Fields in Optoelectronics, Prentice-Hall, Englewood Cliffs, N. J. (1984)

[46] Y. Kawada, T. Yasuda, A. Nakanishi, K. Akiyama, K. Hakamata, H. Takahashi, Achromatic prism-type wave plate for broadband terahertz pulses, Opt. Lett. 39 (2014) 2794.

[47] M. Li, H. Pan, Y. Tong, C. Chen, Y. Shi, J. Wu, H. Zeng, All-optical ultrafast polarization switching of terahertz radiation by impulsive molecular alignment, Opt. Lett. 36 (2011) 3633.

[48] M. Nagai, N. Mukai, Y. Minowa, M. Ashida, J. Takayanagi, H. Ohtake, Achromatic THz wave plate composed of stacked parallel metal plates, Opt. Lett. 39 (2014) 146.

[49] J. Masson, G. Gallot, Terahertz achromatic quarter-wave plate, Opt. Lett. 31 (2006) 265.

[50] A.K. Kaveev, G.I. Kropotov, E.V. Tsygankova, I.A. Tzibizov, S.D. Ganichev, S.N. Danilov, P. Olbrich, C. Zoth, E.G. Kaveeva, A.I. Zhdanov, A.A. Ivanov, R.Z. Deyanov, B. Redlich, Terahertz polarization conversion with quartz waveplate sets, Appl. Opt. 52 (2013) B60.

[51] G. Binnig, H. Rohrer, C. Gerber, E. Weibel, Tunneling through a controllable vacuum gap, Appl. Phys. Lett. 40 (1982) 178–180.

[52] G. Binnig, H. Rohrer, C. Gerber, E. Weibel, Surface Studies by Scanning Tunneling Microscopy, Phys. Rev. Lett. 49 (1982) 57–61.

[53] R. Wiesendanger, Scanning Probe Microscopy and Spectroscopy, Cambridge Univ. Press (1994)

[54] C.J. Chen, Introduction to Scanning Tunneling Microscopy, Oxford Univ. Press (2008)

[55] J. Bardeen, Tunnelling from a Many-Particle Point of View, Phys. Rev. Lett. 6 (1961) 57–59.

[56] J. Repp, G. Meyer, S.M. Stojković, A. Gourdon, C. Joachim, Molecules on Insulating Films: Scanning-Tunneling Microscopy Imaging of Individual Molecular Orbitals, Phys. Rev. Lett. 94 (2005) 026803.

[57] T. Hanaguri, C. Lupien, Y. Kohsaka, D.H. Lee, M. Azuma, M. Takano, H. Takagi, J.C. Davis, A "checkerboard" electronic crystal state in lightly hole-doped Ca 2-xNaxCuO2Cl2, Nature. 430 (2004) 1001–1005.

Chapter 3

THz-Field-Induced Nonlinear Electron Delocalization in Au Nanostructures

Precise and fast control of electrons in metallic nanostructures is indispensable for the development of next-generation devices for advanced information technology. Harnessing THz-field-induced nonlinearity is a promising method of manipulating the ultrafast motion of electrons in metallic systems, while avoiding undesirable thermal effects and electronic transitions.

In this chapter, we will demonstrate how intense single-cycle THz electric fields can be used to manipulate electron delocalization in percolated gold (Au) nanostructures on a picosecond time scale. We fabricate both isolated and percolated Au nanostructures on Si substrates. Unexpected large opacity in the THz transmission spectra occurs in the percolated nanostructures when the THz electric field strength is increased: the maximum THz-field-induced transmittance difference, more than 50%, is reached just above the percolation threshold thickness. By fitting the experimental data using a Drude-Smith model, we also found that the both the localization and scattering of electrons in Au nanostructures decreases as the THz electric field strength increases. These results indicate that nonlinear electron delocalization takes place due to the strong electric field of THz pulses; the intense THz electric field suppresses the backscattering rate at grain boundaries and induces electron tunneling between Au nanostructures across a nanometer-scale air gap without any material breakdown.

3.1 Introduction

It is now possible to generate intense single-cycle terahertz (THz) electric fields with a peak amplitude of 0.1 – 100 MV/cm [1–5]. In contrast to excitation using near-infrared or visible light, THz pulses can access low-frequency elementary excitation directly and accelerate electrons without undesirable interband excitation because of their low photon energy. These advantages have led to the extensive study of THz-field-induced nonthermal and nonlinear phenomena in a wide range of materials, notably dielectrics [6–8], semiconductors [9–12], and semimetals [13,14]. However, despite their fascinating electromagnetic and transport properties, very few studies have been devoted to metallic systems.

Exploiting their high conductivity and chemical stability, metallic systems have been widely studied in the fields of micro- and nano-electronics, and plasmonics. In particular, metallic nanostructures can manifest unique properties that completely differ from those of the bulk material, depending on their morphologies, such as insulator-to-metal transition (IMT) caused by the formation of a percolating network [15,16], surface plasmon-enhanced intense near fields for single-molecule detection [17], high-efficiency THz generation at the percolation threshold [18], and quantum tunneling between metallic nanoparticles [19–21]. Owing to these unique properties, metallic nanostructures are promising candidates for next-generation integrated nanocircuits and plasmonic devices. In this context, it is important to develop methods that can provide improved control over the motion of electrons in metallic nanostructures and their electromagnetic properties.

In order to explain the dielectric properties of inhomogeneous metal nanostructures, effective-medium theories such as the Maxwell-Garnet [22] and Bruggeman [23] models have been proposed that take into account the local-field effect (on a length scale much smaller than the incident wavelength). However, these models struggle to describe systems with strong carrier localization arising from carrier backscattering at the boundaries of grains or nanoparticles, which occurs when the characteristic dimension of the nanostructure becomes comparable to the carrier mean free path at the Fermi energy [24] (e.g., $25-35$ nm in Au). Hence, a phenomenological Drude-Smith model [25] is generally used to explain the carrier response of inhomogeneous metal nanostructures. This is an extension of the simple Drude model with an

additional term that suppresses conductivity at low frequencies [16,26–29].

In this chapter, THz-field-induced nonlinear electron delocalization is demonstrated. We show the experimental THz transmissions and complex dielectric spectra are well described by the Drude-Smith model over relatively broad frequency ranges of 0.35−1.25 THz and 13−100 THz. We also show the THz transmittance decreases dramatically in the percolated Au nanostructures by increasing THz electric field strength, indicating that intense THz electric fields induce electron tunneling between Au nanostructures across nanometer-scale insulating bridges.

3.2 Fabrication of Au nanostructures

In order to fabricate Au nanostructures, we employed the d.c. sputtering method, illustrated schematically in Figure 3.1. In a vacuum chamber, the Au target acts as the cathode, while the Si substrate to be coated is located underneath and acts as the anode. The Au target is vaporized to atoms in the plasma by ionized Argon gas which is accelerated to hit the surface of the target. These vaporized atoms are then deposited onto the Si substrate to form ultrathin Au films with nanogap structures. The average thickness of the ultrathin Au films is precisely controlled by the sputtering time. As the substrate, we used 500 µm thick high resistivity Si(100) wafer covered by a native oxide of about 2 nm thickness [30]. High resistivity Si is used to avoid nonlinear effects from the substrate under intense THz irradiation such as impact ionization [31]. All films were prepared by sputtering and without any post annealing to obtain Au nanostructures that were both isolated and percolated.
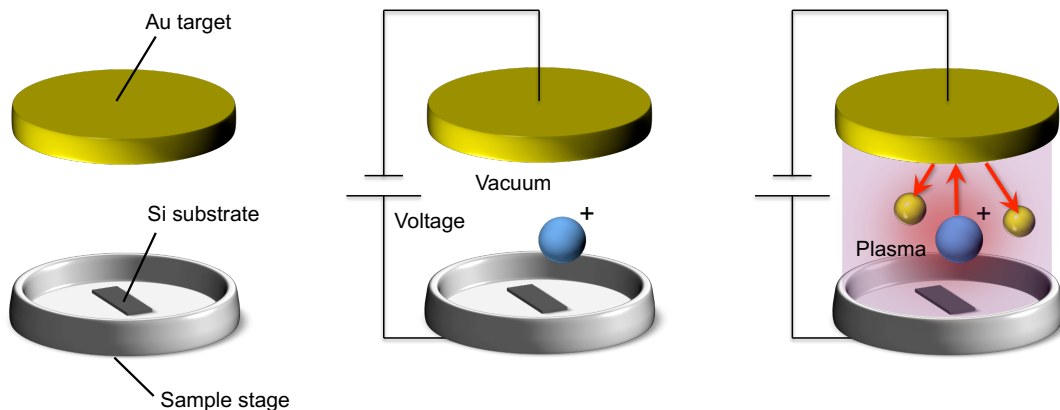
Figure 3.1 | Schematic of d.c. sputtering method.
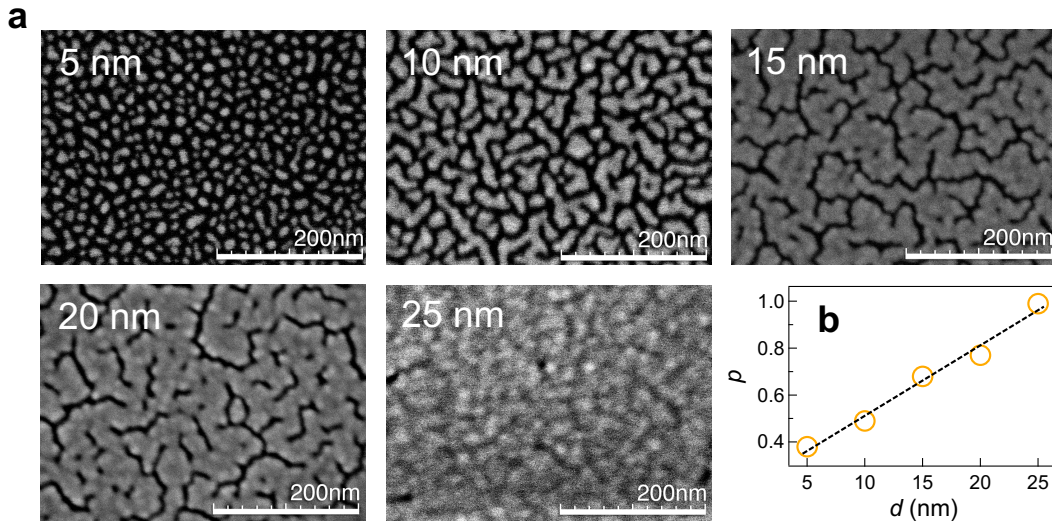
Figure 3.2 | Characterization of Au nanostructures using SEM. (a) Scanning electron micrographs of ultrathin Au films with average thicknesses of $d = 5$, 10, 15, 20, and 25 nm, sputtered on high resistivity Si substrates. **(b)** Fractional surface coverage of the films p as a function of their average thickness. The dashed line highlights the linear correlation.

The surface morphology of the Au films was investigated using scanning electron microscopy (SEM). Figure 3.2a shows the SEM images of Au films with different average thicknesses of $d = 5$, 10, 15, 20, and 25 nm. The surface morphology of the Au film is strongly dependent on average thickness.

In the thinnest sample ($d = 5$ nm), Au nanostructures are isolated, forming nanoislands. In contrast, the nanogap structure almost vanishes in the thickest sample ($d = 25$ nm). Figure 3.2b illustrates the linear correlation
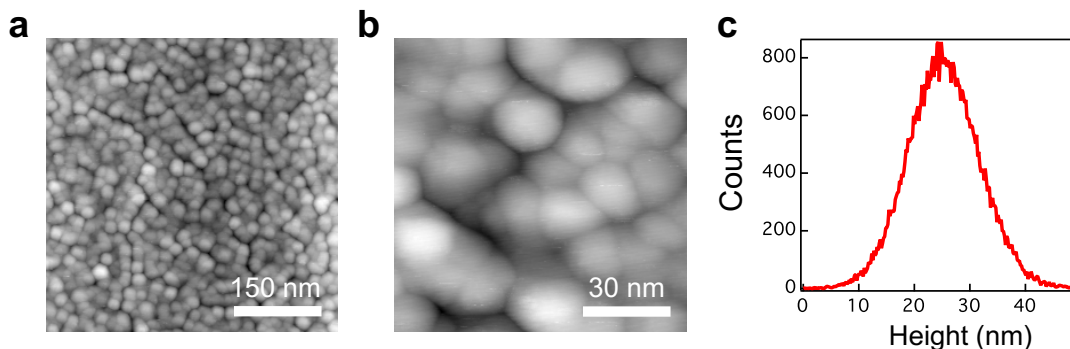
Figure 3.3 | Characterization of Au nanostructures using STM. (a,b) Topographic images of ultrathin Au films with average thicknesses of 25 nm obtained by constant-current mode of STM. **(c)** Height histogram of **(a)** which shows average height of 25 nm.

between the fractional surface coverage (p) and the average thickness. The fractional surface coverage was calculated by applying a filter function to the raw image (Figure 3.2a) in order to separate Au regions from the Si substrate. The isolated Au nanostructures coalesce into a percolating Au network above the percolation threshold coverage, $p = 0.68$ ($d = 15$ nm), which is in good agreement with previously reported values [32]. In this film, IMT is expected to take a place due to percolative transport of electrons. The Au percolation network forms more gradually here than in Au films prepared by thermal evaporation [16]. In order to investigate the 3D profile of Au nanostructures with higher resolution, we measured a topographic image of Au thin film with a thickness of $d = 25$ nm using scanning tunneling microscopy (STM), as shown in Figure 3.3a. The Au thin film consists of Au nanoparticles with a radius of 15-25 nm. This STM image is consistent with the SEM image shown in Figure 3.2a. Average film thickness was determined to be 25 nm using the height histogram (Figure 3.3c). This is in good agreement with the intended value (25 nm) which we sought to achieve by controlling the sputtering time.

3.3   Experimental setup for THz-TDS

Figure 3.4a shows our experimental setup. A Ti:sapphire amplifier system (repetition rate, 1 kHz; pulse duration, 130 fs; center wavelength, 800 nm; pulse energy, 2 mJ/pulse) was employed to generate intense single-cycle THz electric field transients, which were produced using a $LiNbO_3$ prism in a tilted-pulse-front configuration (as we explained in Chapter 2). THz pulses with a beam diameter of 700 μm were incident normally on the Au films. Peak field strengths of up to 340 kV/cm were tuned using a pair of wire-grid polarizers (WG1 and WG2). The THz pulse was measured after passing through the Au thin film using EOS with a 400 μm thick GaP crystal. We confirmed that the transmittance of the plain Si substrate ($T_{Si} = E_{Si}/E_{air} = 0.7$) is independent of the incident THz field strength, ensuring that any nonlinearities in the EOS were negligible in our experiment. All the measurements were performed at room temperature in a nitrogen gas atmosphere in order to avoid water absorption.

  Figure 3.4b illustrates THz transmission measurement through the Au thin film. For all samples, in order to avoid the undesirable phase shift, half of the Si substrate was covered with Au, while the remaining half was a bare Si
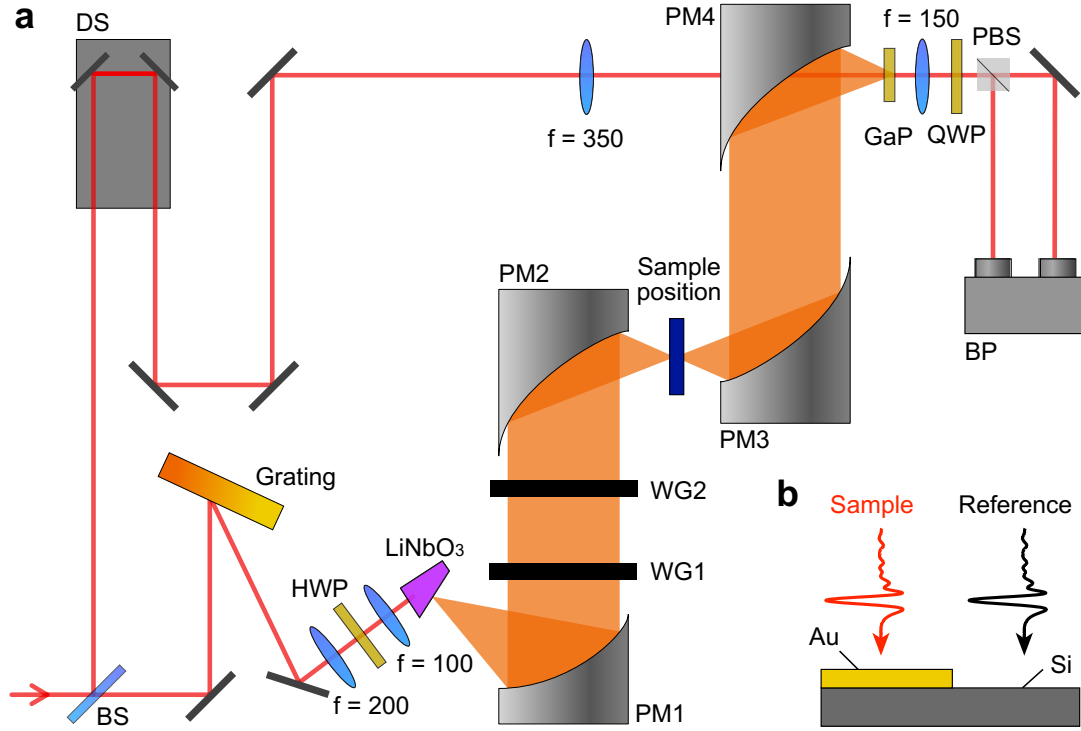
Figure 3.4 | Experimental setup for THz-TDS with intense THz electric field. (a) BS: beam splitter, DS: delay stage, HWP: half-wave plate, PM: parabolic mirror, WG: wire-grid polarizer, QWP: quarter-wave plate, PBS: Polarizing beam splitter, BP: balanced photodiode. **(b)** Illustration of THz transmission measurement through the Au thin film.

substrate. The THz transmittance spectrum was obtained by measuring THz electric-field transients transmitted through an Au thin film and a bare Si substrate. This scheme enables us to discuss THz-field-induced nonlinearity of electrons in Au nanostructures by measuring THz transmittance spectrum as a function of THz electric field strength using ultrathin Au films with different film thicknesses.

3.4 Theory of electrical conduction

3.4.1 Drude model

When free electrons in a metallic or a semiconductor system are exposed to an a.c. electric field of light, the equation of motion is given by

$$m^* \frac{\partial^2 \vec{r}}{\partial t^2} = -m^* \gamma \frac{\partial \vec{r}}{\partial t} - e\vec{E}, \tag{3.1}$$

where m_* is the effective mass of free electrons, and γ is the damping constant. The first term on the right hand side is a frictional force proportional to velocity, and the second term is the Coulomb force acting on free electrons.

Here, we express the a.c. electric field of light using the following equation:

$$\vec{E} = \vec{E}_0 \exp(-i\omega t). \tag{3.2}$$

In this case, free electrons also oscillate with frequency ω. Therefore, the motion of free electrons is given by

$$\vec{r} = \frac{e}{m^*} \frac{1}{\omega^2 + i\omega\gamma} \vec{E}. \tag{3.3}$$

Then, the polarization is given by

$$\vec{P} = \frac{N}{V}\vec{p} = n(-e\vec{r}) = -\frac{ne^2}{m^*} \frac{1}{\omega^2 + i\omega\gamma} \vec{E}, \tag{3.4}$$

where N is the number of free electrons, V is the volume, and n is the density of free electrons. From equation (3.4), the polarizability is given by

$$\tilde{\chi}(\omega) = -\frac{ne^2}{m^*} \frac{1}{\omega^2 + i\omega\gamma}. \tag{3.5}$$

Therefore, using the plasma frequency ω_p, the dielectric constant is given by

$$\tilde{\varepsilon}(\omega) = 1 + \frac{\chi}{\varepsilon_0} = 1 - \frac{\omega_p^2}{\omega(\omega + i\gamma)}, \tag{3.6}$$

where

$$\omega_p^2 = \frac{ne^2}{\varepsilon_0 m^*}, \tag{3.7}$$

while the optical conductivity is given by

$$\tilde{\sigma}(\omega) = \frac{\omega_p^2}{\gamma - i\omega}. \tag{3.8}$$

3.4.2   Drude-Smith model

The Drude-Smith model was developed by N. V. Smith [25] to explain optical conductivity in poor metals such as liquid metals and quasicrystals. In these materials, the optical conductivity spectrum is known to deviate from the Drude model in the infrared region. The Drude-Smith model is derived using an impulse response approach and Poisson statistics as explained below.

Consider a unit impulse of electric field applied to the electron system at time $t = 0$ and the current response at time t $j(t)$. Then $j(0) = ne2/m*$ and the complex conductivity can be obtained from the Fourier transform of $j(t)$:

$$\tilde{\sigma}(\omega) = \int_0^\infty j(t)\exp(i\omega t)dt. \tag{3.9}$$

In the case of isotropic scattering, scattering reduces the population of electrons carrying current, because only non-scattered electrons contribute to the current response. If the carrier relaxation time is τ, the resulting current response is given by

$$j(t)/j(0) = \exp(-t/\tau), \tag{3.10}$$

and the Fourier transform of this equation gives

$$\tilde{\sigma}(\omega) = \frac{ne^2\tau/m^*}{1 - i\omega\tau}, \tag{3.11}$$

which corresponds to the Drude model as described above $(\tau = 1/\gamma)$.

In the case of anisotropic scattering, a scattering event cannot be treated as population decay in the current response. The probability of n anisotropic scattering events in the time interval $(0, t)$ with relaxation time τ is given by the Poisson distribution

$$P_n(0, t) = \frac{(t/\tau)^n\exp(-t/\tau)}{n!}. \tag{3.12}$$

Taking account of the first and subsequent scattering events, the current response is given by

$$j(t)/j(0) = \exp(-t/\tau)\left[1 + \sum_{i=1}^\infty \frac{c_n(t/\tau)^n}{n!}\right], \tag{3.13}$$

where c_n can be viewed as the probability that electrons will experience anisotropic backscattering rather than isotropic scattering. The value of c_n can range from -1 to 0, where complete backscattering occurs for $c_n = -1$ and isotropic scattering is recovered for $c_n = 0$. Here, Smith made a key assumption: anisotropic backscattering only happens for the first scattering event ($n = 1$). The validity of this single-scattering assumption is still under debate [24,33] as we explain later. However, with this assumption, the current response yields

$$j(t)/j(0) = \exp(-t/\tau) \left[1 + \frac{ct}{\tau} \right], \qquad (3.14)$$

where c_1 is relabeled as c. Then, the Drude-Smith optical conductivity can be found using the Fourier transform:

$$\tilde{\sigma}(\omega) = \frac{ne^2\tau/m^*}{1 - i\omega\tau} \left[1 + \frac{c}{1 - i\omega\tau} \right], \qquad (3.15)$$

where c ($-1 \leq c \leq 0$) is a localization parameter that accounts for partial electron localization caused by backscattering. For $c = 0$, the Drude-smith model reduces to the simple Drude model, giving the conductivity due to free electrons. Electron backscattering increases with decreasing c, and for $c = -1$, the electrons are completely localized and afford no d.c. conductivity.

Alternatively, the dielectric constant is given by

$$\tilde{\varepsilon}(\omega) = 1 - \frac{\omega_p^2}{\omega(\omega + i\gamma)} \left(1 + \frac{c}{1 - i\omega\gamma} \right). \qquad (3.16)$$

3.4.3 Physical interpretation of the Drude-Smith model

The Drude-Smith model has been applied to reproduce experimental conductivity spectra for various nanomaterials including Au nanostructures in the THz region [16]. Its most significant difference from the Drude model is the presence of a localization parameter c, which is intended to represent the localization of electrons. As we described above, Smith assumes that the anisotropic backscattering only happens for the first scattering event and any subsequent scattering is always isotropic. However, no physical explanation is

given for introducing this hypothesis. In addition, the physical meaning of the localization parameter c is ambiguous. In most papers using the Drude-Smith model, the meanings of its fit parameters, beyond phenomenological expressions, are not discussed in detail. The physical interpretation of the Drude-Smith model is an active area of research in the THz community [24,33,34]. Němec *et al.* [24], for example, conducted Monte Carlo simulations in 2009 in order to calculate the optical conductivity in the THz range of free charge carriers localized in semiconductor nanoparticles. The shape of conductivity spectra is fitted well by the Drude-Smith model, and they found that the localization parameter c indeed represented the degree of localization of charge carriers, determined by the transmission probability of carriers through interparticle boundaries and the ratio of the nanoparticle size and carrier mean free path in the bulk. Based on this finding (although the validity of the single-scattering approximation remains unclear), we applied the Drude-Smith model to evaluate the localization of electrons in nanostructured Au film.

3.5   Measurement results

Figure 3.5 compares typical THz electric-field transients transmitted through an Au thin film and a plain Si substrate. The inset shows the THz transmission
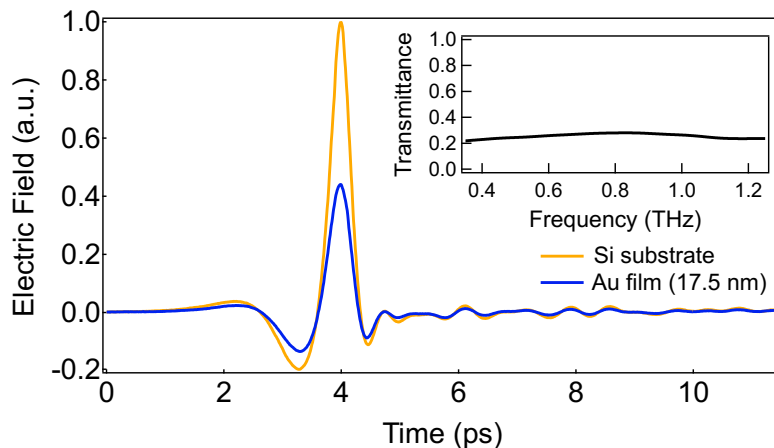

Figure 3.5 | Waveform of transmitted THz electric field. Temporal waveforms of the single-cycle THz electric field transmitted through either a 17.5 nm thick Au film or a plain Si substrate. The maximum field strength of the incident THz electric field was 340 kV/cm. The inset shows the power transmittance spectrum.

spectrum, $|E_{\text{sample}}(\omega)|^2/|E_{\text{reference}}(\omega)|^2$, which is obtained by normalizing the transmitted THz waveform from the Au thin film to that from the Si substrate. As shown in the inset, the transmittance has weak frequency dependence between 0.35 and 1.25 THz. In order to discuss the dependence of the transmittance on the THz electric field strength, the intensities are averaged over this frequency range henceforth.

Figure 3.6a shows the averaged transmittance as a function of the film thickness with different THz peak electric fields. The averaged transmittance is almost unity below the percolation threshold thickness (<15 nm) and then decreases as the thickness of the film increases. This behavior is typically the result of an IMT [16]. The most striking feature shown in Figure 3.6a is the decrease in transmittance as the THz electric field strength increases, which only appears above the percolation threshold (<15 nm). This strongly indicates that electrons in percolated Au nanostructures play a crucial role in THz-field-induced opacity. In order to evaluate this nonlinearity, we define the THz-field-induced transmittance difference as $\Delta\text{OD}(E)/\text{OD}(E_{\text{weak}})$, where $\Delta\text{OD}(E) = \text{OD}(E) - \text{OD}(E_{\text{weak}})$, and $\text{OD}(E)$ and $\text{OD}(E_{\text{weak}})$ are, respectively, the average optical densities at a given THz electric field strength, E, and at
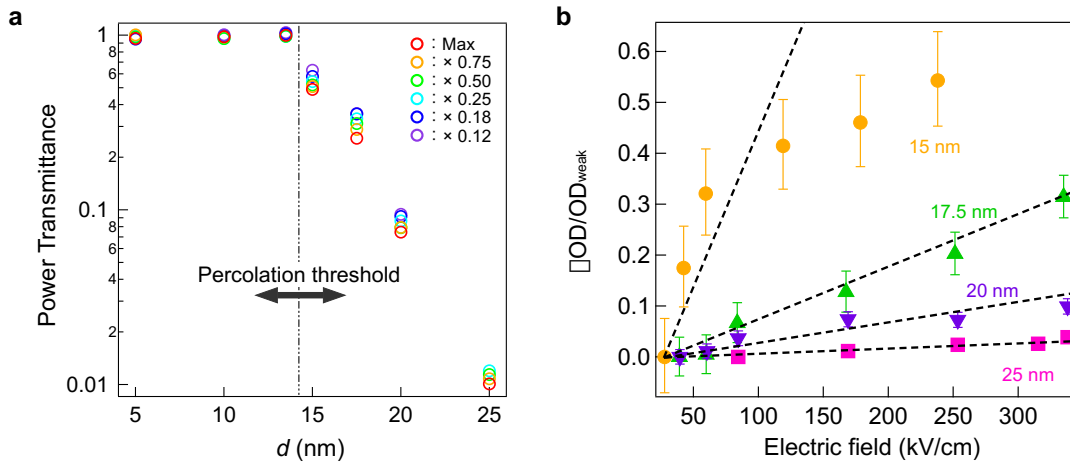
Figure 3.6 | Nonlinear response of Au nanostructures. (a) Averaged THz power transmittance as a function of film thickness for Au films sputtered on high resistivity Si substrates at different THz electric field strengths. The vertical line indicates the percolation threshold thickness. **(b)** THz-field-induced transmittance difference as a function of the electric field strength for Au films of different thicknesses. The dashed lines indicate the nonlinearity, which is more marked the steeper the line.

the weakest field strength, E_{weak}.

Figure 3.6b shows how this nonlinearity varies as a function of the incident THz electric field strength in percolated Au nanostructures with different film thicknesses. The dashed lines, drawn to highlight nonlinear effects, show that the THz-field-induced transmittance difference strongly depends on the thickness of the film. The transmittance difference is maximal (more than 50%) just above the percolation threshold ($\sim$15 nm), and decreases abruptly with increasing film thicknesses, becoming negligible for the 25 nm thick film, which is fully covered with Au ($p \approx 1$). Note that no transmittance difference was observed for the isolated Au nanostructures below the percolation threshold, meaning that this THz-field-induced nonlinearity is characteristic of percolated Au nanostructures.

In order to confirm the presence of an IMT, broadband infrared transmission spectra were measured using a conventional Fourier transform infrared (FT-IR) spectrometer. These spectra are combined in Figure 3.7a for various film thicknesses with THz transmission spectra under the weakest THz electric field of 40 kV/cm (assuming the linear regime). As shown in Figure 3.2a, for thicknesses below the percolation threshold ($<$15 nm), the Au nanostructures are isolated so the transmittance decreases with frequency in the IR region due to a tail of localized surface plasmon resonance located at higher frequency. On the other hand, in the THz region the film becomes transparent because of the absence of free carriers and therefore behaves as an insulator. Near the percolation threshold ($d = 15$ nm), the transmittance becomes small at THz frequencies and the same trend is observed in the IR region, suggesting strong carrier localization at grain boundaries. In contrast, for films thicker than 20 nm, strong attenuation occurs in the THz region, but the transmittance increases with frequency in the IR region, which is typical of metallic phases [35]. This behavior therefore verifies the presence of an IMT in our Au nanostructures with different morphologies.

In order to clarify this non-monotonic behavior of electrons in the metallic phase quantitatively, the sheet dielectric constant was calculated for thicknesses above the percolation threshold using the following formula (as we discussed in Chapter 2);

$$\tilde{\varepsilon}(\omega) = \frac{i(n_2 + 1)\nu_c}{\omega d} \frac{1 - T/T_0}{T/T_0},$$
(3.17)
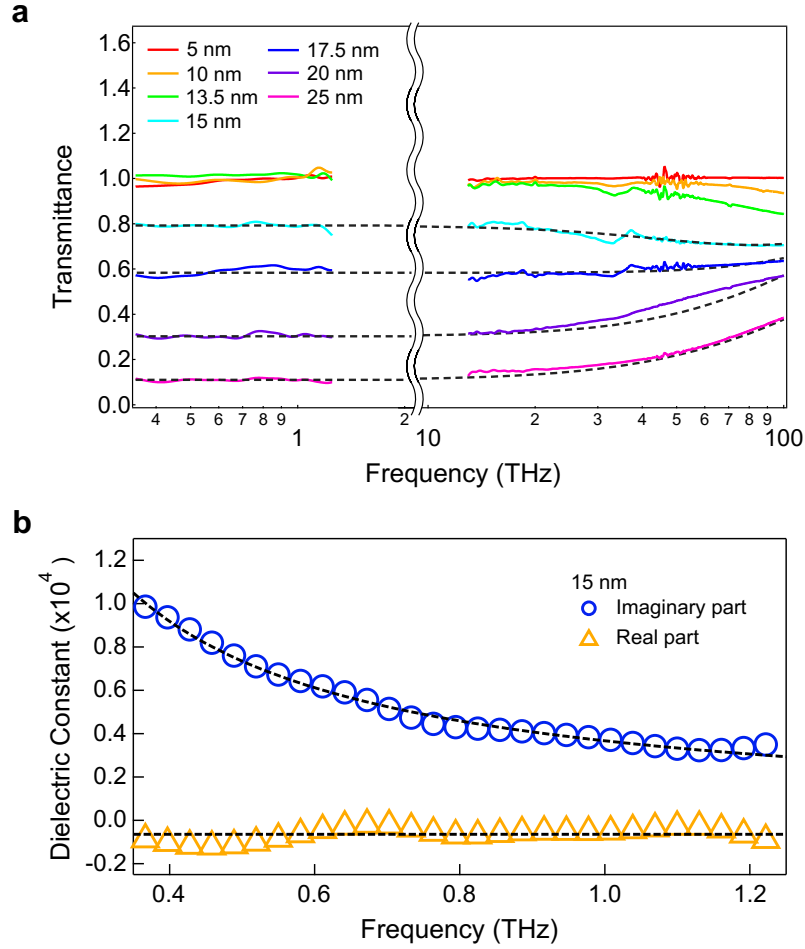
Figure 3.7 | THz and infrared spectra of Au nanostructures. (a) Infrared and THz transmission spectra (at an electric field of 40 kV/cm) for Au films of different thicknesses sputtered on high resistivity Si substrates. **(b)** Real and imaginary parts of the complex dielectric constant measured for 15 nm thick Au film. The dashed curves in (a) and (b) show the best fits obtained using the Drude-Smith model (equation (3.18)).

where, n_2 is the dielectric constant of the Si substrate, d is the thickness of the ultrathin Au films, ν_c is the velocity of light, and T/T_0 is the complex electric field transmittance of the Au films relative to that of the bare Si substrate. Figure 3.7b shows the real and imaginary parts of the dielectric constant for a 15 nm-thick Au film at the weakest field strength of 40 kV/cm. In order to clarify the behavior of conduction electrons, the data were fitted to the Drude-Smith model using

$$\tilde{\varepsilon}(\omega) = \varepsilon_\infty - \frac{\omega_p^2}{\omega(\omega + i\gamma)}\left(1 + \frac{c}{1 - i\omega\gamma}\right), \tag{3.18}$$

69

where ε_∞ is the dielectric constant at infinitely high frequency, ω_p is the plasma frequency, γ is the damping constant, and c $(-1 \leq c \leq 0)$ is a localization parameter (described in detail in Sections 3.4.2 and 3.4.3). The resulting fits, shown in Figure 3.7a, b by dashed curves, have good agreement with the transmittance at $0.35-1.25$ and $13-100$ THz, as well as for the real and imaginary parts of the dielectric constant, confirming that this numerical evaluation is reasonable for revealing details of conduction electrons in Au nanostructures.

Figure 3.8a-c shows the fitted Drude-Smith parameters in the linear regime (with the lowest THz electric field), obtained by fitting broadband spectra as shown in Figure 3.7a, b, in order to highlight the influence of nanostructure morphology on electron conduction. With decreasing film thicknesses, both the effective electron density and the plasma frequency decrease because of the depolarization effect [36]. The negative localization parameter c approaches 0 as the films become thicker, whereas the damping constant decreases toward the bulk value $(\gamma/2\pi = 17.1$ THz [37]). This indicates that thicker Au films have electromagnetic properties similar to those of bulk Au; namely, the localized electrons become mobile because of reduced backscattering at grain boundaries.

Focusing now on THz-field-induced nonlinearity, recall that this is enhanced for thicknesses just above the percolation threshold, as shown in Figure 3.6a, b. Figure 3.9a, b shows the fitted Drude-Smith parameters – the localization parameter and damping constant – as functions of the THz field strength
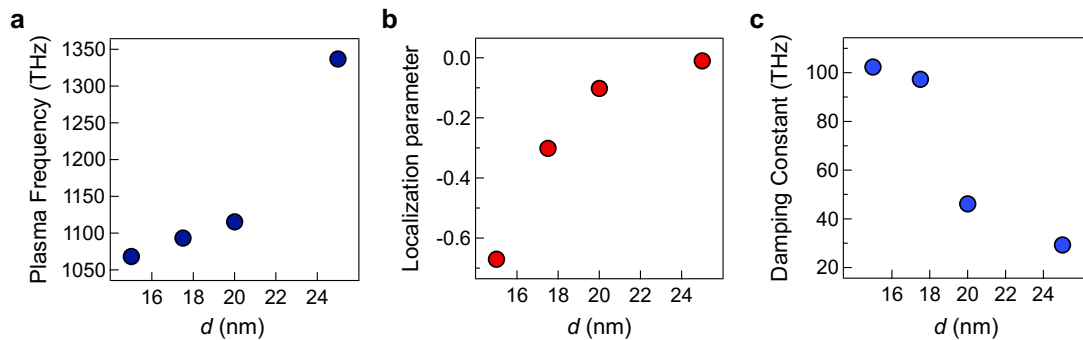

Figure 3.8 | Drude-Smith parameters in the linear regime. (a) Plasma frequency. **(b)** Localization parameter. **(c)** Damping constant. These parameters are obtained by fitting both broadband transmission spectrum $(0.35-1.25$ and $13-100$ THz) and complex dielectric constant $(0.35-1.25$ THz) with the lowest THz electric field.
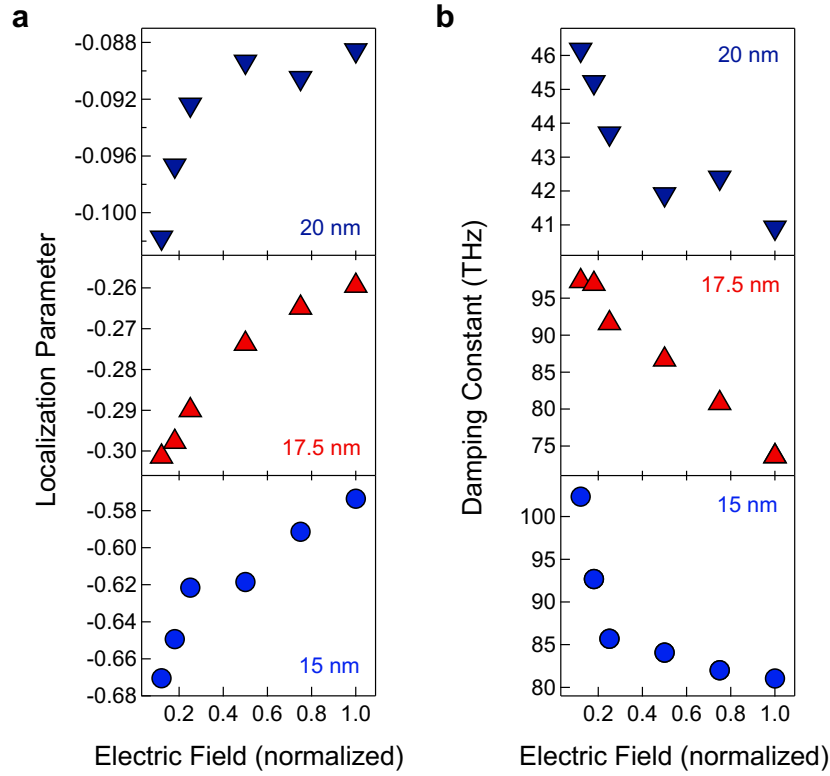
Figure 3.9 | Drude-Smith parameters in the nonlinear regime. (a) The localization parameter and **(b)** the damping constant in the Drude-Smith model as a function of the normalized THz field strength for percolated Au films with different average thicknesses.

(normalized to the maximum value) in a percolated Au nanostructure with film thickness of 15, 17.5, and 20 nm. Although the absolute values differ for percolated Au nanostructures of different film thicknesses, in each case the damping constant decreases and the localization parameter increases toward 0 with increasing THz electric field strengths. This indicates that the observed nonlinearity has a single cause. Note the increased variability of the Drude-Smith parameters close to the percolation threshold thickness; the large negative value of c indicates the strong carrier backscattering due to many open nanogaps. The nonlinear behavior can be understood by considering electron delocalization under a strong electric field of THz pulses.

3.6 Discussion

We believe that electron delocalization occurs mainly through electron tunneling, which is suggested in the d.c. field experiments [38,39]. When a

sufficiently strong local field is applied to a nanometer-scale insulating bridge, the insulating channel becomes conductive due to intergrain tunneling, leading to less electron backscattering and thereby lowering the damping constant, as schematically illustrated in Figure 3.10. Note that the characteristic time required to complete electron tunneling is sufficiently short compared with the pulse duration of the single-cycle THz electric field ($\sim$1 ps) [40]. The THz electric field may therefore be regarded as a quasi-static field for the tunneling process, and as a result, it could effectively produce the nonlinearity.

We also note that this nonlinear response is repeatable, not irreversible, as is, for instance, material breakdown [41]. The reversibility was confirmed by the THz transmission measurement with low field strength after intense THz irradiations. Any irreversible change was observed in our ultrathin Au films. In micrometer-scale metamaterials with Au split-ring resonators (SRR), strong electric field enhancement occurs at THz frequencies due to LC resonance [42]. This THz-electric-field enhancement can readily and permanently damage SRR gap structures. In contrast, the percolated Au nanostructures are not damaged, probably because the electron tunneling itself reduces the field enhancement [19] and/or the relatively long length-scale of the Au network places their resonance outside the THz range. Percolated Au nanostructures therefore suppress excess THz-field enhancement and avoid permanent breakdown, while retaining the nonlinearity required to enhance electron tunneling across the nanometer-scale insulating bridges.

Our findings, large THz-field-induced opacity and/or nonlinear electron
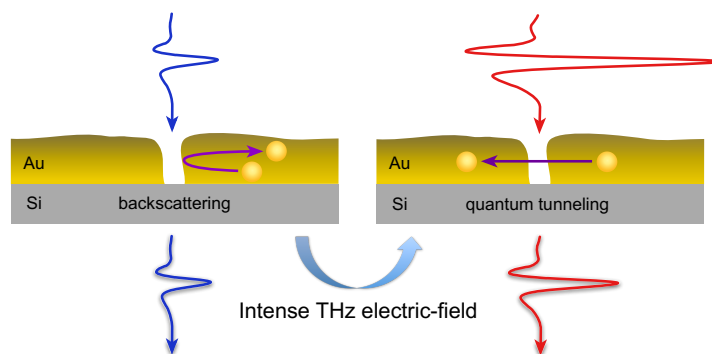

Figure 3.10 | THz -field-induced quantum tunneling. The backscattering of electrons at the grain boundaries plays an important role in electron localization under weak THz electric field strengths, whereas the quantum tunneling of electrons is induced across the narrow insulating bridge between the Au nanostructures by intense THz electric field strengths.

delocalization in percolated Au nanostructures, should prove useful for controlling and enhancing the unique electromagnetic properties of metal nanostructures on the picosecond time scale, which, more generally, will be useful for future microelectronics and nanometer-scale plasmonic devices.

Finally, we would like to discuss the validity of the Drude-Smith model used in our analysis. We evaluated the complex dielectric constants for all the experimental data with different THz electric field strengths, based on the same procedure generally used in the linear regime. The obtained dielectric constants therefore deviate from conventional dielectric properties, because they include contributions from nonlinear polarizations. However, because the nonlinearity might be averaged over the whole Au nanostructure randomly distributed with different sizes and nanogaps, we believe that our analysis provides a preliminary intuitive understanding of the origin of THz-induced nonlinearity. Recent research, using well-defined nanogap structures, has reported transmittance decrease due to electron tunneling induced via intense THz electric fields [43,44]. The use of well-defined nanogap structures in these studies enabled an in-depth analysis of nonlinear electron tunneling and the enhanced electric field, and also made it possible to successfully estimate the dielectric change at the nanogap.

3.7   Summary and outlook

In summary, the nonlinear response of localized electrons driven by intense THz electric field transients has been demonstrated in ultrathin Au films with percolated Au nanostructures. As the THz electric field strength is increased, large opacity in the THz transmission spectrum occurs in percolated Au nanostructures. The Drude-Smith model was applied over wide frequency ranges, viz. 0.35−1.25 and 13−100 THz, in order to understand the nonlinear behavior of localized electrons quantitatively. The damping constant in this model decreases and the localization parameter increases as the strength of the incident THz electric field is increased. The experimental data indicate that ultrafast electron delocalization occurs due to the strong electric field of THz pulses, leading to electron tunneling across the narrow insulating bridge between Au nanostructures without material breakdown. These results show that intense THz pulses are a highly effective means of controlling the electromagnetic properties of metal nanostructures.

In this chapter, we investigated THz-field-induced electron tunneling in random nanogap structures via THz-TDS. Our results strongly suggest that the combination of a single-cycle THz electric field and a tunnel junction is a promising candidate for a new platform for ultrafast lightwave nanoelectronics. To this end, it is essential to be able to detect and manipulate the THz-field-induced tunnel current directly. Furthermore, detailed mechanisms of THz-field-induced electron tunneling, such as dynamics, nonlinearity, and field enhancement, will become clear by using a well-defined tunnel junction. In the following chapter, we will show how these ideas can be investigated using THz scanning tunneling microscopy (THz-STM).

References in chapter 3

[1]   K.L. Yeh, M.C. Hoffmann, J. Hebling, K.A. Nelson, Generation of 10 μJ ultrashort terahertz pulses by optical rectification, Appl. Phys. Lett. 90 (2007).

[2]   H. Hirori, A. Doi, F. Blanchard, K. Tanaka, Single-cycle terahertz pulses with amplitudes exceeding 1 MV/cm generated by optical rectification in LiNbO$_3$, Appl. Phys. Lett. 98 (2011) 091106.

[3]   Y. Minami, T. Kurihara, K. Yamaguchi, M. Nakajima, T. Suemoto, High-power THz wave generation in plasma induced by polarization adjusted two-color laser pulses, Appl. Phys. Lett. 102 (2013) 041105.

[4]   A. Sell, A. Leitenstorfer, R. Huber, Phase-locked generation and field-resolved detection of widely tunable terahertz pulses with amplitudes exceeding 100 MV/cm., Opt. Lett. 33 (2008) 2767–2769.

[5]   F. Junginger, A. Sell, O. Schubert, B. Mayer, D. Brida, M. Marangoni, G. Cerullo, A. Leitenstorfer, R. Huber, Single-cycle multiterahertz transients with peak fields above 10 MV/cm., Opt. Lett. 35 (2010) 2645–7.

[6]   I. Katayama, H. Aoki, J. Takeda, H. Shimosato, M. Ashida, R. Kinjo, I. Kawayama, M. Tonouchi, M. Nagai, K. Tanaka, Ferroelectric Soft Mode in a SrTiO3 Thin Film Impulsively Driven to the Anharmonic Regime Using Intense Picosecond Terahertz Pulses, Phys. Rev. Lett. 108 (2012) 097401.

[7]   T. Miyamoto, H. Yada, H. Yamakawa, H. Okamoto, Ultrafast modulation of polarization amplitude by terahertz fields in electronic-type organic ferroelectrics., Nat. Commun. 4 (2013) 2586.

[8]   C. Somma, K. Reimann, C. Flytzanis, T. Elsaesser, M. Woerner, High-Field Terahertz Bulk Photovoltaic Effect in Lithium Niobate, Phys. Rev. Lett. 112 (2014) 146602.

[9]   J. Hebling, M.C. Hoffmann, H.Y. Hwang, K.-L. Yeh, K.A. Nelson, Observation of nonequilibrium carrier distribution in Ge, Si, and GaAs by terahertz pump–terahertz probe measurements, Phys. Rev. B. 81 (2010) 035201.

[10] H. Hirori, K. Shinokita, M. Shirai, S. Tani, Y. Kadoya, K. Tanaka, Extraordinary carrier multiplication gated by a picosecond electric field pulse, Nat. Commun. 2 (2011) 594.

[11] F. Junginger, B. Mayer, C. Schmidt, O. Schubert, S. Mährlein, A. Leitenstorfer, R. Huber, A. Pashkin, Nonperturbative Interband Response of a Bulk InSb Semiconductor Driven Off Resonantly by Terahertz Electromagnetic Few-Cycle Pulses, Phys. Rev. Lett. 109 (2012) 147403.

[12] O. Schubert, M. Hohenleutner, F. Langer, B. Urbanek, C. Lange, U. Huttner, D. Golde, T. Meier, M. Kira, S.W. Koch, R. Huber, Sub-cycle control of terahertz high-harmonic generation by dynamical Bloch oscillations, Nat. Photonics. 8 (2014) 119–123.

[13] S. Tani, F. Blanchard, K. Tanaka, Ultrafast Carrier Dynamics in Graphene under a High Electric Field, Phys. Rev. Lett. 109 (2012) 166603.

[14] H. Hwang, N. Brandt, H. Farhat, Nonlinear THz conductivity dynamics in p-type CVD-grown graphene, J. Phys. Chem. B. 117 (2013) 15819.

[15] J.J. Tu, C.C. Homes, M. Strongin, Optical Properties of Ultrathin Films: Evidence for a Dielectric Anomaly at the Insulator-to-Metal Transition, Phys. Rev. Lett. 90 (2003) 017402.

[16] M. Walther, D. Cooke, C. Sherstan, M. Hajar, M. Freeman, F. Hegmann, Terahertz conductivity of thin gold films at the metal-insulator percolation transition, Phys. Rev. B. 76 (2007) 125408.

[17] X.-M. Qian, S.M. Nie, Single-molecule and single-nanoparticle SERS: from fundamental mechanisms to biomedical applications, Chem. Soc. Rev. 37 (2008) 912.

[18] G. Ramakrishnan, P.C.M. Planken, Percolation-enhanced generation of terahertz pulses by optical rectification on ultrathin gold films., Opt. Lett. 36 (2011) 2572–4.

[19] D.C. Marinica, A.K. Kazansky, P. Nordlander, J. Aizpurua, A.G. Borisov, Quantum plasmonics: Nonlinear effects in the field enhancement of a plasmonic nanoparticle dimer, Nano Lett. 12 (2012) 1333–1339.

[20] J.A. Scholl, A. García-Etxarri, A.L. Koh, J.A. Dionne, Observation of Quantum Tunneling between Two Plasmonic Nanoparticles, Nano Lett. 13 (2013) 564–569.

76

[21] S.F. Tan, L. Wu, J.K.W. Yang, P. Bai, M. Bosman, C.A. Nijhuis, Quantum Plasmon Resonances Controlled by Molecular Tunnel Junctions, Science. 343 (2014) 1496–1499.

[22] J. Garnett, Colours in Metal Glasses and in Metallic Films, Proc. R. Soc. London. (1904).

[23] D.A.G. Bruggeman, Berechnung verschiedener physikalischer Konstanten von heterogenen Substanzen. I. Dielektrizitätskonstanten und Leitfähigkeiten der Mischkörper aus isotropen Substanzen, Ann. Phys. 416 (1935) 636–664.

[24] H. Němec, P. Kužel, V. Sundström, Far-infrared response of free charge carriers localized in semiconductor nanoparticles, Phys. Rev. B. 79 (2009) 115309.

[25] N. Smith, Classical generalization of the Drude formula for the optical conductivity, Phys. Rev. B. 64 (2001) 155106.

[26] R. Lovrinčić, A. Pucci, Infrared optical properties of chromium nanoscale films with a phase transition, Phys. Rev. B. 80 (2009) 205404.

[27] C. Richter, C.A. Schmuttenmaer, Exciton-like trap states limit electron mobility in TiO2 nanotubes., Nat. Nanotechnol. 5 (2010) 769–72.

[28] D.G. Cooke, F.C. Krebs, P.U. Jepsen, Direct Observation of Sub-100 fs Mobile Charge Generation in a Polymer-Fullerene Film, Phys. Rev. Lett. 108 (2012) 056603.

[29] S.A. Jensen, R. Ulbricht, A. Narita, X. Feng, K. Müllen, T. Hertel, D. Turchinovich, M. Bonn, Ultrafast photoconductivity of graphene nanoribbons and carbon nanotubes., Nano Lett. 13 (2013) 5925–30.

[30] A.H. Al-Bayati, K.G. Orrman-Rossiter, J.A. van den Berg, D.G. Armour, Composition and structure of the native Si oxide by high depth resolution medium energy ion scattering, Surf. Sci. Lett. 241 (1991) A5.

[31] H. Wen, M. Wiczer, A. Lindenberg, Ultrafast electron cascades in semiconductors driven by intense femtosecond terahertz pulses, Phys. Rev. B. 78 (2008) 125203.

[32] Y. Yagil, P. Gadebbe, C. Julien, G. Deutscher, Optical properties of thin semicontinuous gold films over a wavelength range of 2.5 to 500 μm, Phys. Rev. B. 46 (1992).

[33] T.L. Cocker, D. Baillie, M. Buruma, L. V. Titova, R.D. Sydora, F. Marsiglio, F.A. Hegmann, Microscopic origin of the Drude-Smith model, Phys. Rev. B. 96 (2017) 205439.

[34] K. Shimakawa, T. Itoh, H. Naito, S.O. Kasap, The origin of non-Drude terahertz conductivity in nanomaterials, Appl. Phys. Lett. 100 (2012) 132102.

[35] B. Gompf, J. Beister, T. Brandt, J. Pflaum, M. Dressel, Nanometer-thick Au-films as antireflection coating for infrared light., Opt. Lett. 32 (2007) 1578–80.

[36] A. Bittar, S. Berthier, J. Lafait, Non metal-metal transition in Bruggeman optical theory for inhomogeneous media, J. Phys. 45 (1984) 623–631.

[37] P. Johnson, R. Christy, Optical constants of the noble metals, Phys. Rev. B. 1318 (1972).

[38] C.A. Neugebauer, M.B. Webb, Electrical Conduction Mechanism in Ultrathin, Evaporated Metal Films, J. Appl. Phys. 33 (1962) 74.

[39] Y. Gefen, W. Shih, R. Laibowitz, J. Viggiano, Nonlinear Behavior near the Percolation Metal-Insulator Transition, Phys. Rev. Lett. 57 (1986) 3097–3100.

[40] A.S. Landsman, U. Keller, Attosecond science and the tunnelling time problem, Phys. Rep. 547 (2015) 1–24.

[41] Y. Yagil, G. Deutscher, D. Bergman, Electrical Breakdown Measurements of Semicontinuous Metal Films, Phys. Rev. Lett. 69 (1992) 1423–1426.

[42] M. Liu, H.Y. Hwang, H. Tao, A.C. Strikwerda, K. Fan, G.R. Keiser, A.J. Sternbach, K.G. West, S. Kittiwatanakul, J. Lu, S.A. Wolf, F.G. Omenetto, X. Zhang, K.A. Nelson, R.D. Averitt, Terahertz-field-induced insulator-to-metal transition in vanadium dioxide metamaterial, Nature. 487 (2012) 345–348.

[43] J.-Y. Kim, B.J. Kang, J. Park, Y.-M. Bahk, W.T. Kim, J. Rhie, H. Jeon, F. Rotermund, D.-S. Kim, Terahertz Quantum Plasmonics of Nanoslot Antennas in Nonlinear Regime, Nano Lett. 15 (2015) 6683–6688.

[44] Y.-M. Bahk, B.J. Kang, Y.S. Kim, J.-Y. Kim, W.T. Kim, T.Y. Kim, T. Kang, J. Rhie, S. Han, C.-H. Park, F. Rotermund, D.-S. Kim, Electromagnetic Saturation of Angstrom-Sized Quantum Barriers at Terahertz Frequencies, Phys. Rev. Lett. 115 (2015) 125501.

Chapter 4

Real-Space Coherent Manipulation of Electrons in a Single Tunnel Junction

The ultrafast coherent manipulation of electrons using the electric field of waveform-controlled laser pulses is a key technique in the development of lightwave electronics. Developing such a technique for a tunnel junction will provide a new platform for governing ultrafast currents on an even smaller scale, which will be indispensable for the advancement of next-generation ultrafast quantum nanocircuits and plasmonic devices.

In this chapter, we demonstrate that carrier-envelope-phase (CEP) controlled single-cycle terahertz (THz) electric fields can coherently drive electron tunneling either from a nanotip to a sample or vice versa in a scanning tunneling microscope (STM). The motion of electrons in a single tunnel junction can be coherently manipulated in real-space by controlling the CEP of the THz electric field. Spatially confined intense THz pulses with a peak amplitude of more than 10 V/nm strongly modulate the potential barrier at a single tunnel junction on the subpicosecond timescale and can steer a large number of electrons in an extremely nonlinear regime, which is not possible using a conventional STM with d.c. electric field. We expect our results, by making available a new, ultrafast and ultrasmall experimental regime, will pave the way for the future development of nanoscale science and technologies.

4.1 Introduction

The latest advances in laser technology have made it possible to control the carrier-envelope phase (CEP) of ultrashort laser pulses with high accuracy. Using few-cycle CEP-controlled near-infrared (NIR) laser pulses, several studies have demonstrated the ultrafast coherent control of electrons in a wide range of systems [1–9]. In these studies, metallic nanostructures, so-called metal nanotips, were used to produce highly localized near-fields by concentrating laser pulses to a scale far below the diffraction limit of the incident light. Using a spatiotemporally tunable near-field of up to ∼10 V/nm, the sub-cycle control of ultrafast electron bursts from a nanotip has been realized [7–9].

 These sophisticated electron manipulations offer the opportunity to overcome the bandwidth limitation of signal processing in modern information technology [10,11]. The largest field enhancement is expected to occur at a tunnel junction [12–15] by concentrating the laser field at a sub-nanometer scale. The strong nonlinearity of electron tunneling will be useful for the manipulation of electrons at the atomic scale, which is highly desirable for the advancement of next-generation integrated nanocircuits [12,13,16,17] and plasmonic devices [14,18,19].

 However, strong NIR laser pulses focused on a tunnel junction induce thermal expansion [20], leading to permanent damage to the junction. Therefore, precise control of the motion of electrons at the atomic scale is still a challenging task. Recently, single-cycle electric field transients with high intensity have been generated in the terahertz (THz) spectral range (0.1–10 THz) [21,22]. In contrast to few-cycle NIR laser pulses, single-cycle THz electric fields with a bandwidth over an octave may be useful for accurately steering electrons and may, because of their low photon energy, drive electron tunneling without undesirable heating. Indeed, THz-field-induced nonlinear electron tunneling has been observed in percolated gold nanostructures [23] and metal–graphene–metal hybrid structures [14] without any adverse thermal effects. Terahertz scanning tunneling microscopy (THz-STM) [15], which was developed after optical pump–probe STM [24,25], may allow atomic-scale imaging of ultrafast dynamics with fewer thermal expansion problems.

 In this chapter, we demonstrate real-space coherent manipulation of the motion of electrons in a single tunnel junction using CEP-controlled

single-cycle THz electric fields. In the THz spectral range, no suitable medium for changing the CEP has been identified yet, because most materials exhibit a flat frequency response in this range, in contrast to NIR laser pulses. Therefore, it remains difficult to investigate the CEP-dependence of nonlinear response using a low-frequency (below 10 THz) single-cycle THz electric field. In order to actively control the CEP, we utilize the Gouy phase shift [26] by placing a lens pair in the THz beam path. Unlike the imaging of surfaces at the atomic scale using conventional STM, our THz-STM with the tunnel junction presented here acts as an ultrafast rectifying diode or a THz field-effect transistor; the electron current is switched on and off via the CEP-controlled single-cycle THz electric fields.

4.2   Experimental setup

4.2.1   Scanning tunneling microscope

A commercial STM (Digital Instruments, Nanoscope E), which has excellent stability in air, was used in this study. Sharp nanotips were fabricated by electrochemical etching of a Pt/Ir (80/20%) wire with a diameter of 0.3 mm, while blunter tips were obtained by pulling the wire with pliers. The formation of the nanotip apex was confirmed using a scanning electron microscope (SEM),
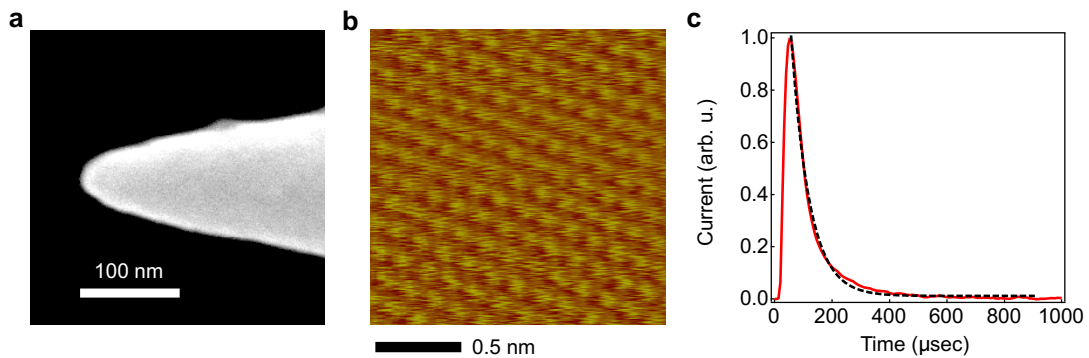
Figure 4.1 | Setup for the tunnel junction of STM. (a) SEM image of a sharp nanotip fabricated by electrochemical etching with a tip apex diameter of 40 nm. **(b)** STM image of HOPG with atomic resolution. **(c)** Typical current pulse generated by a single THz pulse. The dashed curve shows the best fit obtained using a single exponential function with a decay time of 63 ± 1 µs, which corresponds to the bandwidth of the current amplifier incorporated in the STM circuit.

as shown in Figure 4.1a. Highly oriented pyrolytic graphite (HOPG) was freshly cleaved before the measurements to obtain a clean surface, and its atomically flat surface was confirmed using the STM, as shown in Figure 4.1b. Figure 4.1c shows a tunnel current pulse with a decay time of 63 ± 1 μs generated by a single THz pulse. This decay time corresponds to the bandwidth (15 kHz) of a current amplifier incorporated in the STM circuits. Since the bandwidth is much greater than the repetition rate (1 kHz) of THz pulses, integrating the current pulse with respect to time gives the number of rectified electrons driven by a single THz pulse through the junction; i.e., the number of rectified electrons, N, was calculated using $N = \int (I(t)/e)dt,$ where $I(t)$ is the tunnel current and e is the elementary charge.

4.2.2   Experimental setup for the THz-STM

Figure 4.2 shows our experimental setup for the THz-STM. As a light source, we employed a Ti:sapphire regenerative amplifier with a repetition rate of 1 kHz, a pulse duration of 130 fs, and a center wavelength of 800 nm. As shown
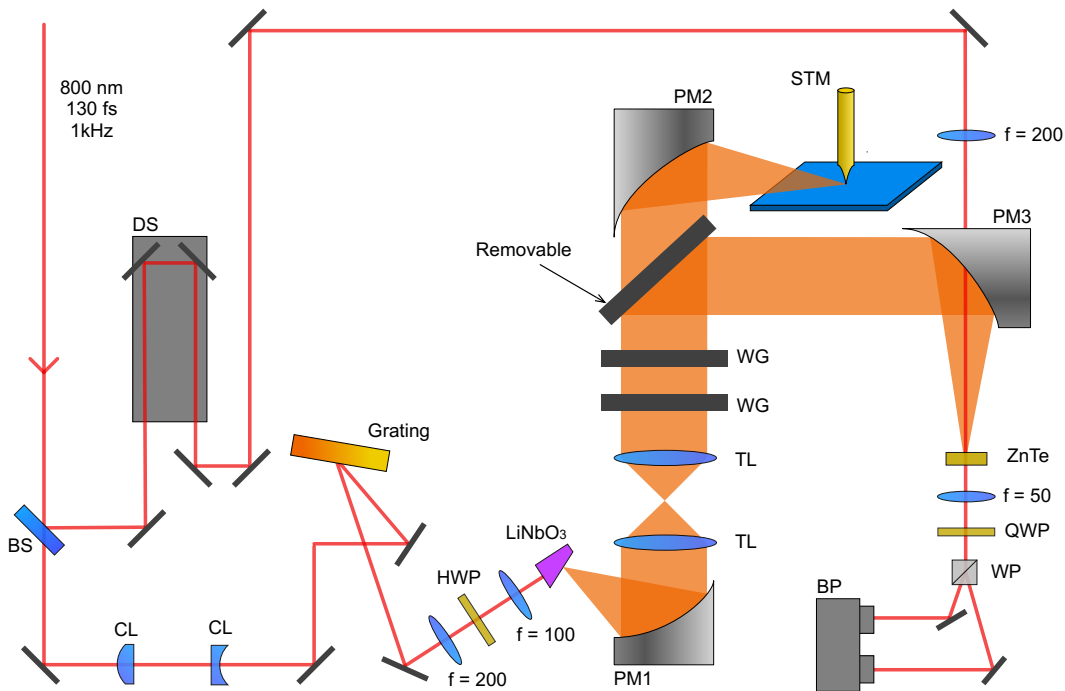

Figure 4.2 | Experimental setup for THz-STM. BS: beam splitter, DS: delay stage, CL: cylindrical lens, HWP: half-wave plate, PM: parabolic mirror, TL: Tsurupica lens, WG: wire grid polarizer, QWP: quarter-wave plate, WP: Wollaston prism, BP balanced photodiode.

in Chapter 2, intense single-cycle THz electric field transients were generated using a LiNbO$_3$ prism in a tilted-pulse-front configuration [21]. The generated THz pulses were collimated by a gold-coated off-axis parabolic mirror (PM1), and the field strength was tuned by a pair of wire grid polarizers. In order to generate the THz pulses with a CEP of π or $\pi/2$, we set either a pair of spherical or cylindrical Tsurupica lenses, respectively, in the optical pathway. The waveform-controlled THz pulses were then guided into one of two paths by tuning a removable Au-coated mirror: one was used for characterizing the THz pulses by electro-optic sampling (EOS) and the other was used for delivering the THz pulses to a tunnel junction of the STM. For the EOS, a 2 mm-thick ZnTe (110) crystal was used as an EO crystal. The field strength was evaluated by assuming an electro-optic coefficient of $r_{41} = 3.9$ pm/V and refractive indices of $n_{800\mathrm{nm}} = 2.86$ and $n_{\mathrm{THz}} = 3.19$. In order to accurately characterize the THz waveform at the junction, identical off-axis parabolic mirrors (PM2 and PM3) with 4-inch focal length and 2-inch diameter were used to focus the THz pulses. The resulting beam diameter at the STM junction and the EO crystal was 1.2 mm. The THz tunnel current was recorded by a digital oscilloscope via the STM circuits. All measurements were performed under ambient laboratory conditions. Note that intense THz electric fields with a repetition rate lower than the bandwidth of the circuits were used in our system. Therefore, we could observe the tunnel current as a pulse train in real-time using a conventional oscilloscope.

4.3   Theory of electron tunneling

Electron tunneling between electrodes separated by a thin insulator, as schematically shown in Figure 4.3, was extensively studied by Simmons [27] in the 1960s. Here, we describe the Simmons model, which can be used to calculate the *I–V* (current vs. voltage) and *I–Z* (current vs. distance) curves in the tunnel junction.

  The probability $D(E_x)$ that an electron can penetrate a potential barrier $V(x)$ is given by the WKB approximation [28]

$$D(E_x) = \exp\left\{ -\frac{4\pi}{h} \int_{s_1}^{s_2} [2m(V(x) - E_x)]^{\frac{1}{2}} dx \right\}, \tag{4.1}$$

where E_x is longitudinal energy of the electron (normal to the surface), s_1 and

s_2 are the two roots of $V(x) - E_x = 0$. The mumber N_1 of electrons tunneling through the barrier from metal electrode 1 (M_1) to metal electrode 2 (M_2) is given by

$$N_1 = \frac{1}{m} \int_0^{E_m} n(v_x) D(E_x) dE_x, \tag{4.2}$$

where E_m is the maximum energy of electrons in the electrode, and $n(v_x)$ is given using the Fermi distribution function $f(E)$ by

$$n(v_x) = \frac{4\pi m^3}{h^3} \int_0^\infty f(E) dE_r, \tag{4.3}$$

with polar cordinates; $v_r^2 = v_y^2 + v_z^2$, $E_r^2 = m v_r^2 / 2$. Then, N_1 can be expressed by

$$N_1 = \frac{4\pi m^2}{h^3} \int_0^{E_m} D(E_x) dE_x \int_0^\infty f(E) dE_r. \tag{4.4}$$

In the same way,

$$N_2 = \frac{4\pi m^2}{h^3} \int_0^{E_m} D(E_x) dE_x \int_0^\infty f(E + eV) dE_r. \tag{4.5}$$

Therefore, the tunnel current J is given by
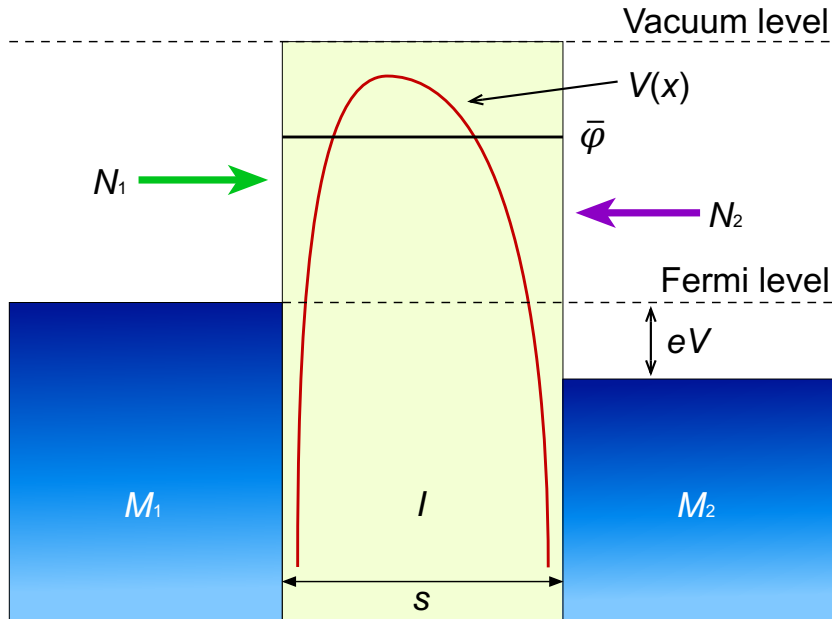
Figure 4.3 | Metal-insulator-metal tunnel junction.

$$J = N_1 - N_2 = \int_0^{E_m} D(E_x)dE_x \times \left\{ \frac{4\pi m^2}{h^3} \int_0^{\infty} [f(E) - f(E + eV)]dE_r \right\}. \quad (4.6)$$

This formula can be further simplified to

$$J = \alpha J_0 \left\{ \bar{\varphi} \exp(-A\bar{\varphi}^{\frac{1}{2}}) - (\bar{\varphi} + eV)\exp\left[-A(\bar{\varphi} + eV)^{\frac{1}{2}} \right] \right\}, \quad (4.7)$$

with $J_0 = e/2\pi h \Delta s^2$ and $A = (4\pi \Delta s/h)(2m)^{\frac{1}{2}}$, where $\bar{\varphi}$ is the mean barrier height, $\Delta s (= s_1 - s_2)$ is the effective barrier width, m is the electron mass, h is Planck's constant, and α is a scaling parameter that accounts for the density of states and the effect of the geometry of the tunnel junction. This equation can be applied to a potential barrier of arbitrary shape, providing the mean barrier height is known.

The potential barrier in the tunnel junction is expressed by considering a rectangular potential barrier, an external bias voltage, and an image potential as follows:

$$\varphi(x) = \varphi_0 - \frac{eV}{s}x + V_i(x), \quad (4.8)$$

where φ_0 is the effective work function of the junction, V is the applied bias voltage across the gap, s is the gap width, and $V_i(x)$ is the image potential. Now $V_i(x)$ is given by

$$V_i(x) = \left(-\frac{e^2}{8\pi\varepsilon} \right) \left[\frac{1}{2x} + \sum_{n=1}^{\infty} \left\{ \frac{ns}{[(ns)^2 - x^2]} \right\} - \frac{1}{ns} \right], \quad (4.9)$$

where ε is the permittivity of the gap. We approximated the image potential by

$$V_i(x) = -\frac{1.15\lambda s^2}{x(s-x)}, \quad (4.10)$$

where

$$\lambda = \frac{e^2 \ln 2}{16\pi\varepsilon s}, \quad (4.11)$$

which is a good approximation to the true image potential. Note that $V_i(x)$ is half that in the original Simmons equation, which included an error previously noted by Miskovsky *et al.* [29]. The mean barrier height is given by

$$\bar{\varphi} = \frac{1}{\Delta s} \int_{s_1}^{s_2} V_i(x) dx, \tag{4.12}$$

where s_1 and s_2 are the real roots of the cubic equation

$$\varphi_0 - \frac{eV}{s}x - \frac{1.15\lambda s^2}{x(s-x)} = 0. \tag{4.13}$$

When considering a rectangular potential barrier without including the image potential, the tunnel current J can be calculated in the three different regimes, shown schematically in Figure 4.4.
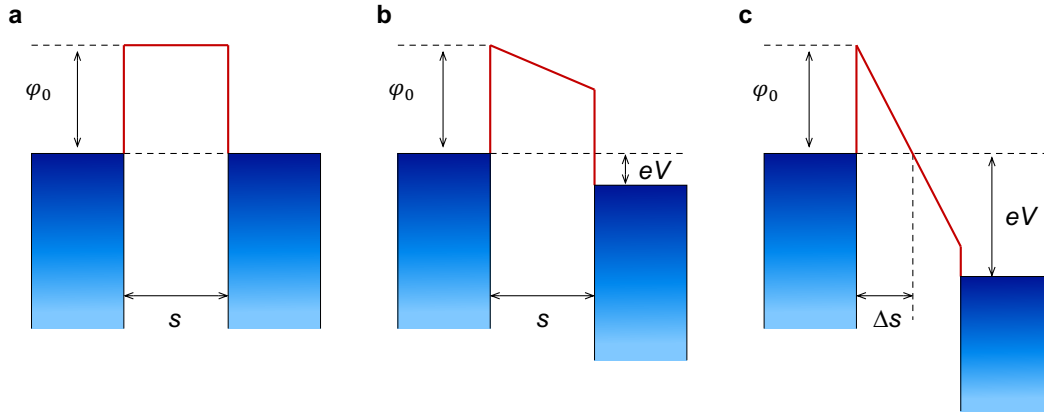
Figure 4.4 | Potential barrier with rectangular shape. (a) Low-voltage regime: $V \cong 0$. **(b)** Intermediate-voltage regime: $V < e/\varphi_0$. **(c)** High-voltage regime: $e/\varphi_0 < V$.

(a) Low-voltage regime : $V \cong 0$ (Figure 4.4a)

$$J = \left[3(2m\varphi_0)^{\frac{1}{2}}/2s \right] (e/h)^2 V \exp\left[-(4\pi s/h)(2m\varphi_0)^{\frac{1}{2}} \right]. \tag{4.14}$$

(b) Intermediate-voltage regime : $V < e/\varphi_0$ (Figure 4.4b)

$$J = \left(\frac{e}{2\pi h s^2} \right) \left\{ \left(\varphi_0 - \frac{eV}{2} \right) \exp\left[-\frac{4\pi s}{h}(2m)^{\frac{1}{2}} \left(\varphi_0 - \frac{eV}{2} \right)^{\frac{1}{2}} \right] \right.$$

$$- \left(\varphi_0 + \frac{eV}{2} \right) \exp\left[-\frac{4\pi s}{h}(2m)^{\frac{1}{2}}\left(\varphi_0 + \frac{eV}{2} \right)^{\frac{1}{2}} \right] \Biggr\}.$$

$$(4.15)$$

(c) High-voltage regime : $e/\varphi_0 < V$ (Figure 4.4c)

$$J = \frac{2.2e^3F^2}{8\pi h\varphi_0} \Biggl\{ \exp\left[-\frac{8\pi}{2.96heF}(2m)^{\frac{1}{2}}\varphi_0^{\frac{3}{2}} \right]$$

$$- \left(1 + \frac{2eV}{\varphi_0} \right)\exp\left[-\frac{8\pi}{2.96heF}(2m)^{\frac{1}{2}}\varphi_0^{\frac{3}{2}}\left(1 + \frac{2eV}{\varphi_0} \right)^{\frac{1}{2}} \right] \Biggr\},$$

$$(4.16)$$

with $F = V/\Delta s$.

4.4 Measurement results

4.4.1 CEP control of THz-field-driven tunnel current

Our experimental set-up is illustrated schematically in Figure 4.5a–c. The generated THz pulses were guided into one of two optical paths: one was used to characterize the THz waveforms using EOS, while the other was used to deliver the THz pulses to a single tunnel junction. By placing either a pair of spherical or cylindrical lenses in the beam path (Figure 4.5b), the CEP of the incident THz pulses ($\phi_{\mathrm{CEP}} = 0$) was shifted by $\phi_{\mathrm{CEP}} = \pi$ or $\phi_{\mathrm{CEP}} = \pi/2$, respectively, via the Gouy phase shift. As schematically shown in Figure 4.5c, the CEP-controlled single-cycle THz electric field modifies the potential barrier between the nanotip and the sample, leading to the unidirectional coherent motion of electrons.

By irradiating the junction with THz pulses with $\phi_{\mathrm{CEP}} = 0$ (Figure 4.6a), a series of tunnel currents were synchronously generated with the same repetition rate as the laser system (1 kHz), as shown in Figure 4.6b. Note that the time-integrated value of each current pulse represents the number of rectified electrons driven by a single THz pulse through the junction, as we
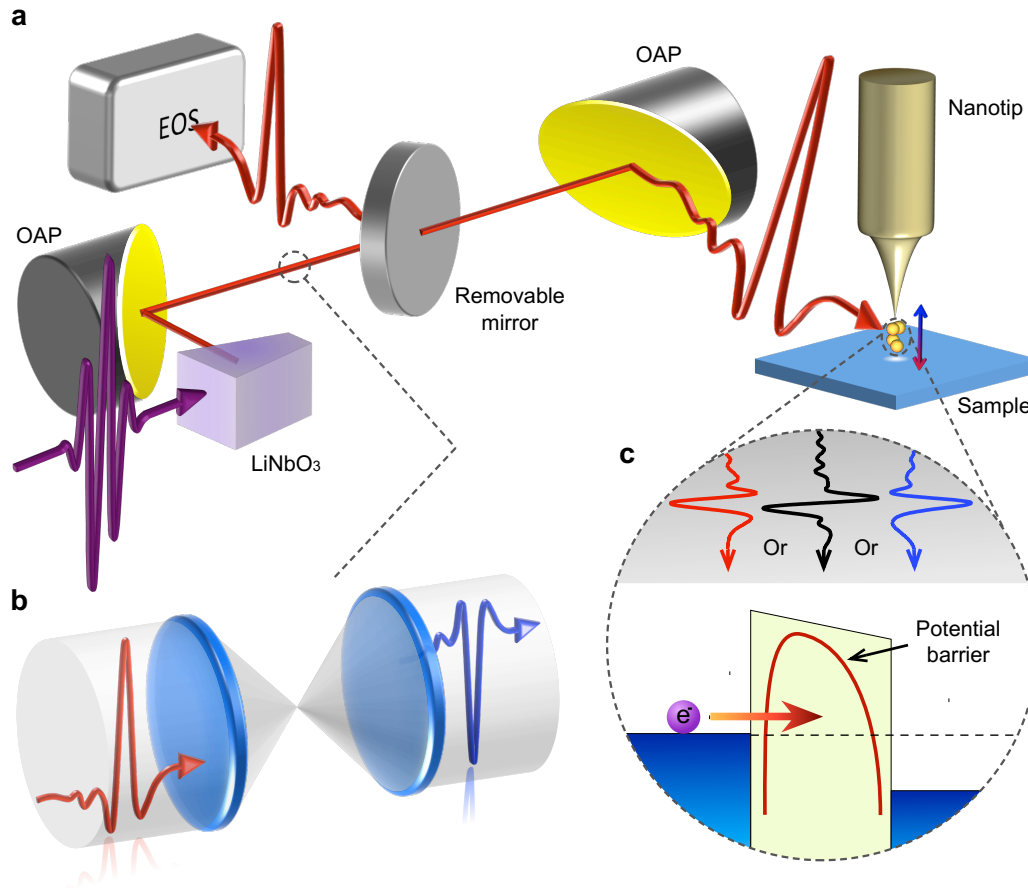
Figure 4.5 | Schematic illustrations of the experiment and measurements.
(a) CEP-controlled single-cycle THz electric fields are focused onto the apex of a Pt/Ir nanotip at an incident angle of 75°. OAP, off-axis parabolic mirror; EOS, electro-optic sampling. **(b)** π phase-shift of a THz electric field via the Gouy phase shift using a pair of spherical lenses. A pair of cylindrical lenses is used when a $\pi/2$ phase-shift is required **(c)** An electron (e$^-$) tunneling between a nanotip and a sample under the influence of a static electric field. The motion of electrons is coherently controlled using THz electric fields with different CEPs.

explained in Section 4.2.1.

The CEP dependence of the tunnel current was measured with different CEPs of $\phi_{CEP} = 0$, $\pi/2$ and π, while adjusting the d.c. bias from 300 mV to – 300 mV (Figure 4.7a, b). The most remarkable feature of Figure 4.7b is a series of THz-induced pulse trains, which is the fingerprint of ultrafast current bursts in the tunnel junction. In the case of $\phi_{CEP} = 0$, the pulse train takes a positive value, which corresponds to an electron tunneling from the nanotip to the sample. The intensity of the pulse train increases with increasing d.c. bias. In the case of $\phi_{CEP} = \pi$, on the other hand, the tunnel current shows the
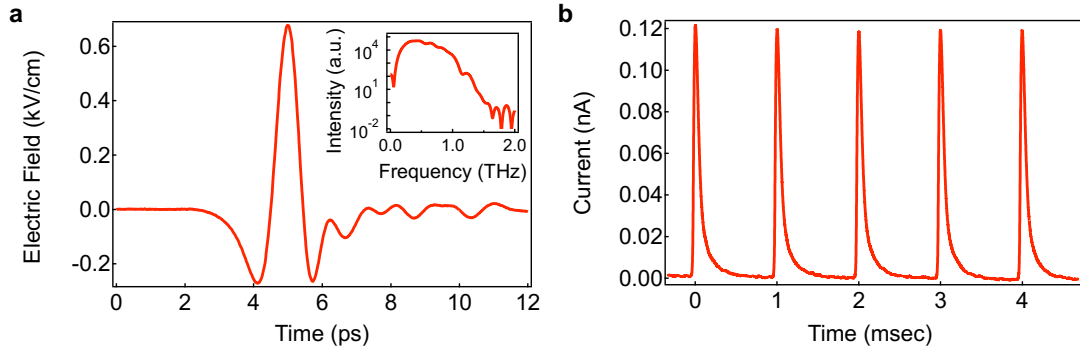
Figure 4.6 | THz-field-driven tunnel current without d.c. bias. (a)
Temporal profile of a single-cycle THz electric field ($\phi_{\mathrm{CEP}} = 0$) measured
using EOS. The inset shows the corresponding THz frequency spectrum.
(b) Pulse train generated by the THz electric field ($\phi_{\mathrm{CEP}} = 0$) without any
d.c. bias. The feedback loop remained off during the measurement
(setpoint: bias voltage $V_{\mathrm{s}} = 1$ V; tunnel current $I_{\mathrm{s}} = 1$ nA). The decay
profile of each current pulse comes from the bandwidth of the amplifier
used in the STM circuits.

opposite behaviour; the pulse train with a negative value indicating an electron
tunneling from the sample to the nanotip. In the case of $\phi_{\mathrm{CEP}} = \pi/2$, the
direction of electron tunneling strongly depends on the d.c. bias; electrons
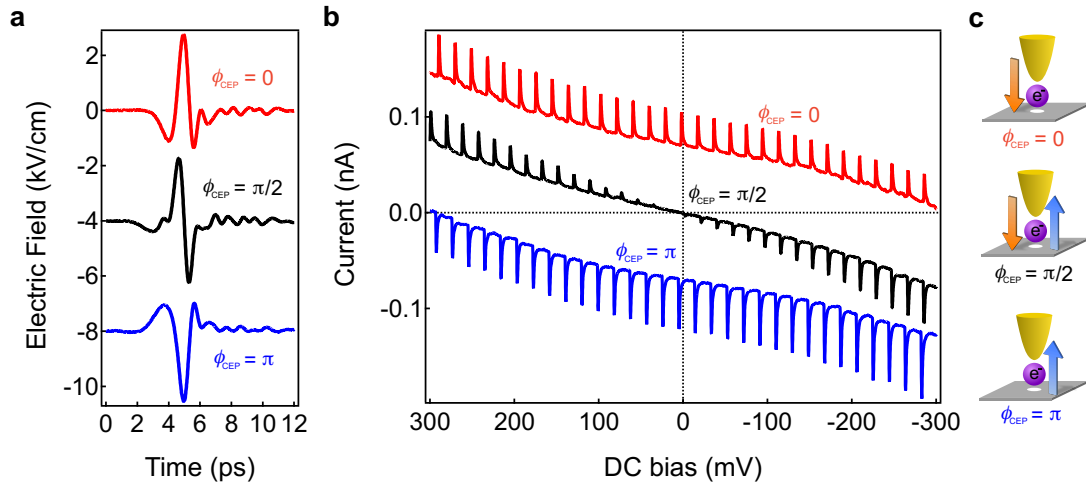
**Figure 4.7 | CEP dependence of THz-field-driven tunnel current with d.c.
bias. (a)** Temporal profiles of single-cycle THz electric fields with different
CEPs ($\phi_{\mathrm{CEP}} = 0$, $\pi/2$ and π). **(b)** CEP dependence of tunnel current as a
function of d.c. bias (Vs = 1 V, Is = 0.5 nA). The spectra with $\phi_{\mathrm{CEP}} = 0$
and π are offset by ± 0.07 nA for clarity. **(c)** Schematic illustration of the
motion of electrons driven by THz electric fields with different CEPs. The
orange and blue arrows show the tunnelling direction.
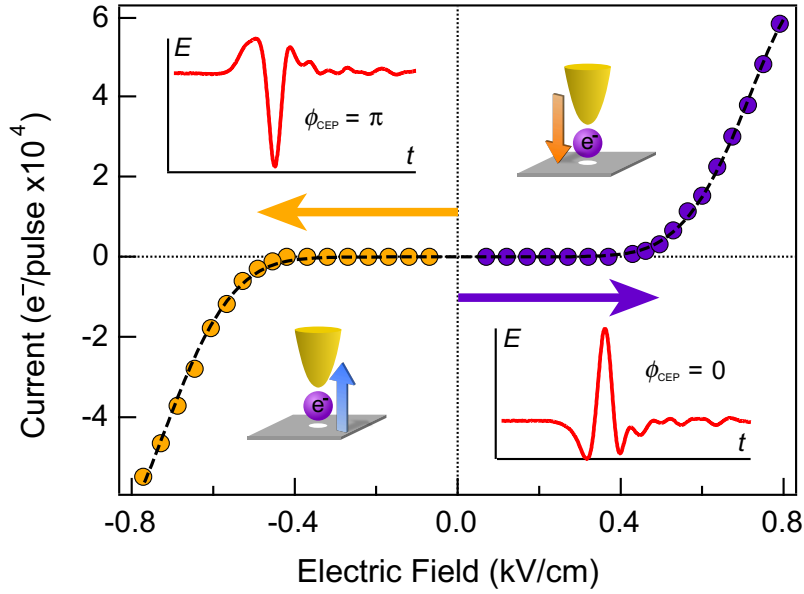
Figure 4.8 | CEP and power dependence of THz-field-driven tunnel current. Number of rectified electrons induced by a single THz pulse without d.c. bias as a function of the peak electric field ($V_s = 1$ V, $I_s = 1$ nA). The insets show the corresponding incident THz waveforms with different CEPs ($\phi_{CEP} = 0$, π). The dashed curve shows the best fit obtained by the Simmons model.

undergo tunneling from the nanotip to the sample under a positive d.c. bias and in the opposite direction under a negative d.c. bias. The current pulse disappears as the d.c. bias approaches 0. As schematically summarized in Figure 4.8c, the coherent motion of electrons at the junction is controlled by the CEP-controlled THz pulses with a given d.c. bias.

Figure 4.8 shows the number of rectified electrons induced by a single THz pulse as a function of the peak electric field with different CEPs ($\phi_{CEP} = 0$ and $\phi_{CEP} = \pi$). The nonlinear increase in the number of rectified electrons with the THz electric field was computed on the basis of the Simmons model [27] assuming a potential barrier between the nanotip (M_1) and the sample (M_2) under a bias voltage V, as illustrated in Figure 4.3. More details about the modeling of THz-field-driven tunnel current will be given in Section 4.5. As shown by the dashed line in Figure 4.8, the experimental data are accurately reproduced by the adjustable parameters of an effective work function of 3.8 ± 0.1 eV, a gap width of 1.00 ± 0.01 nm and an enhancement factor of $100,000 \pm 10,000$. These values were also confirmed by current–distance (I–Z) and d.c. current–voltage (I–V) experiments, as we discuss in Section 4.4.2. The large

field enhancement originates from the extremely tight focusing of the THz electric field onto the single junction with a 1 nm gap between the sample and the nanotip induced by the broadband antenna effect of the nanotip and/or the plasmonic effect at the tunnel junction [8,13].

4.4.2   *I–V* and *I–Z* characteristics of the tunnel junction under d.c. electric field

In order to further confirm the validity of the estimated parameters – i.e., the effective work function, the gap width and the field enhancement factor – we carried out two *I–Z* (current vs. distance) and d.c. *I–V* (current vs. voltage) measurements. Figure 4.9a shows the observed current as a function of the change in the tip-surface distance. The mean barrier height $\bar{\varphi}$ was estimated to be 3.3 ± 0.1 eV under the setpoint bias voltage of 1 V. The effective work function φ_0 was therefore determined to be 3.8 ± 0.1 eV by taking account of the fact that $\bar{\varphi} = \varphi_0 - eV/2$. On the other hand, as shown in Figure 4.9b, the gap width was experimentally estimated to be 0.85 ± 0.17 nm by driving the
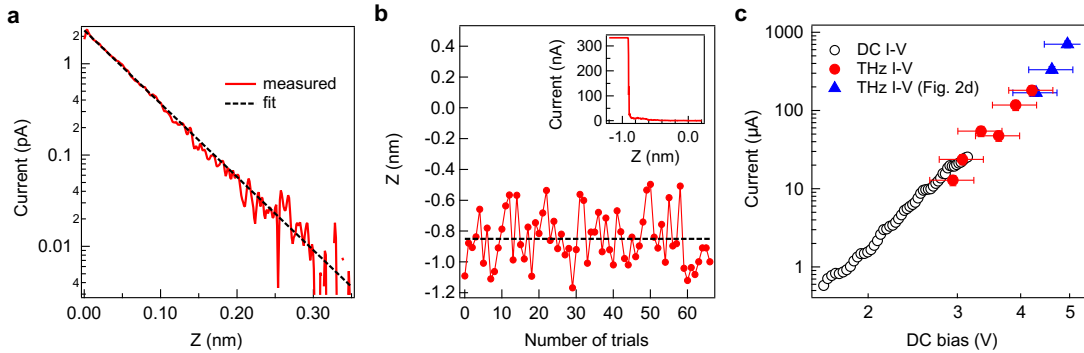
Figure 4.9 | Characterization of the tunnel junction using d.c. electric field. **(a)** Measured *I–Z* curve (setpoint: bias voltage $V_s = 1$ V, tunnel current $I_s = 2.5$ pA). The data were fitted using $I = \exp(-1.025\sqrt{\bar{\varphi}}\,Z)$ with a mean barrier height of $\bar{\varphi} = 3.3 \pm 0.1$ eV. **(b)** Gap width measured by driving the tip into the graphite ($V_s = 1$ V, $I_s = 1$ nA). The inset shows a typical *I–Z* curve. The rapid increase in the current indicates the point of contact. The gap width was determined to be 0.85 ± 0.17 nm. **(c)** Log-log plot of *I–V* data obtained from the d.c. *I–V* and THz *I–V* measurements ($V_s = 1$ V, $I_s = 1$ nA). The THz *I–V* data were reproduced from the THz-field-induced current data using the THz waveforms experimentally obtained by EOS; the field enhancement factor was estimated to be $100,000 \pm 10,000$.

tip into the HOPG sample. These values are in reasonably good agreement with those obtained from the Simmons model. Finally, we performed d.c. *I–V* measurement under a high-voltage regime in order to directly determine the field enhancement factor [30]. The upper limit of the d.c. voltage was 3.2 V because of the damage threshold of the HOPG sample [31]. The THz *I–V* measurement was also carried out under low THz electric fields (0.3–0.4 kV/cm) in order to combine the results of the two *I–V* experiments, i.e., the d.c. *I–V* experiment and the THz *I–V* experiment under high electric fields shown in Figure 4.8. Here, the THz *I–V* data were reproduced from the THz-field-induced current data (as typically shown in Figure 4.6b) using the THz waveforms experimentally obtained by EOS, yielding a field enhancement factor of 100,000 $\pm$ 10,000. As shown in Figure 4.9c, the three experimental results overlap smoothly, indicating that the obtained field enhancement factor is in fairly good agreement with that estimated from the Simmons model.

4.4.3 Electron tunneling in an extremely nonlinear regime

By further increasing the THz electric field, we can implement a new regime for electron tunneling that is not available using conventional STM. The results are shown in Figure 4.10a for three different tips: two sharp nanotips (tips 1, 2) and one blunt tip (tip 3) as shown in the inset. The curves plotting the number of rectified electrons as a function of the incident electric field exhibit different behavior for each tip. However, after converting the incident electric field into the enhanced electric field, the curves exhibit almost the same behavior (Figure 4.10b), indicating that the tip geometry affects the enhancement factor, and that the sharp tip can tightly focus the THz electric field.

The striking feature in Figure 4.10b is the strong saturation of the tunneling electrons observed above the enhanced electric field of 6 Vnm^{-1}, which was not predicted by the conventional Simmons model. A recent self-consistent calculation [32] predicted a new regime that deviates from the Simmons model at extremely high voltages, the so-called space-charge-limited regime, in which an additional space-charge potential plays an important role in limiting the current flow in the junction. In this calculation, the saturation of the tunnel currents occurred above 6 Vnm^{-1} with a work function of 4.08 eV; these values are in reasonably good agreement with our results. Note that this regime

cannot be realized with a d.c. bias voltage or near-infrared pulses because the junction is destroyed by Joule heating and high-energy photons, respectively [20].
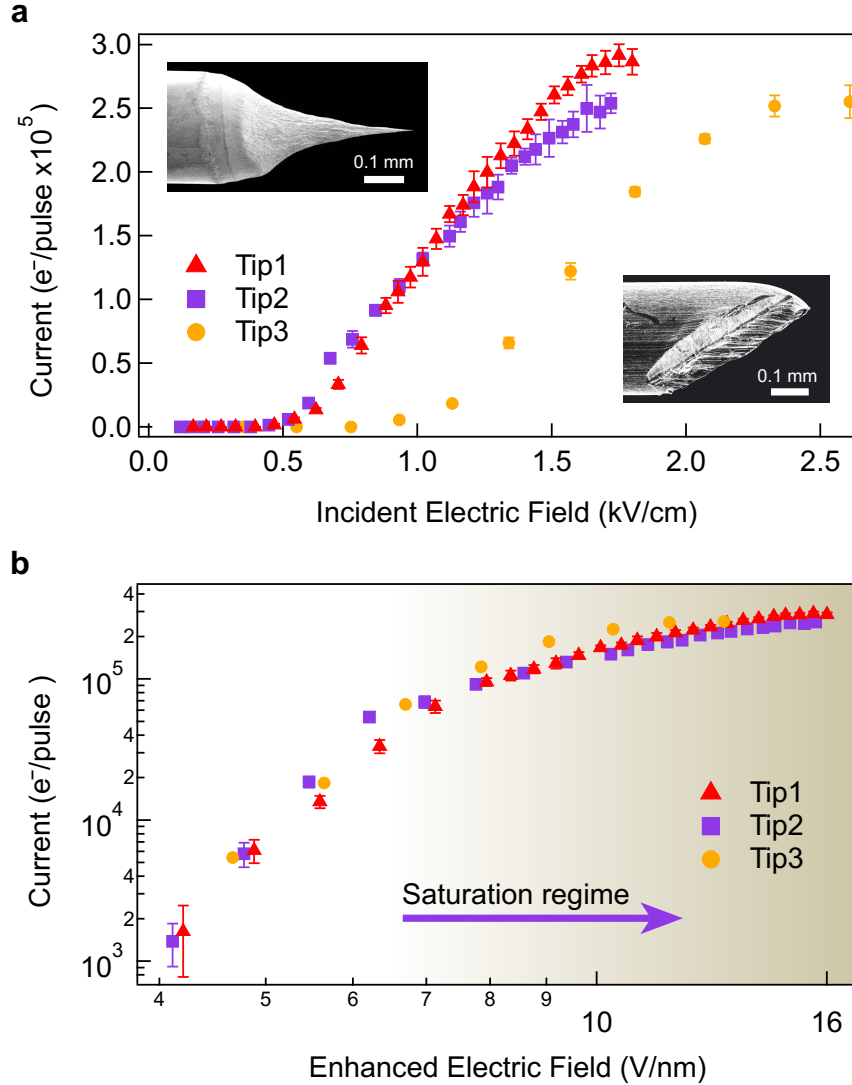
Figure 4.10 | Saturation of electron tunneling in extremely nonlinear regime. (a) Number of rectified electrons without d.c. bias as a function of incident electric field ($\phi_{\mathrm{CEP}} = 0$) for different tips ($V_{\mathrm{s}} = 1$ V, $I_{\mathrm{s}} = 1$ nA). Tips 1 and 2 (sharp) were fabricated by electrochemical etching; tip 3 (blunt) was formed by mechanical cutting. Insets: scanning electron microscopy images of the sharp (top) and blunt (bottom) tips. **(b)** Log-scale plot of number of rectified electrons as a function of the enhanced electric field at the tunnel junction. The enhancement factor of tip 3 is $50{,}000 \pm 200$, which is two times smaller than that of the sharp nanotips. Error bars correspond to 95% confidence intervals.

Finally, we stress that an enhanced THz electric field of 16 Vnm^{-1} was achieved at the junction, which is two times higher than the strongest THz field previously reported in free space [33]. This spatially confined large single-cycle THz electric field can coherently drive the motion of as many as ∼300,000 electrons on the subpicosecond timescale.

4.4.4 Imaging of Au nanostructures

Finally, we investigate the spatial resolution of our THz-STM by nanoscale imaging of Au nanostructures. Here, a topographic image of the sample and the THz-field-driven tunnel current are obtained simultaneously by scanning the sample surface using the constant-current mode of the STM. In order to detect pure THz-field-driven tunnel current by filtering out the d.c. component coming from the feedback bias, we used lock-in detection by modulating the THz pulses at 500 Hz with an optical chopper.

Figure 4.11a shows the STM topography of the Au nanostructures deposited on a HOPG substrate, whereas Figure 4.11b shows the tunnel current map
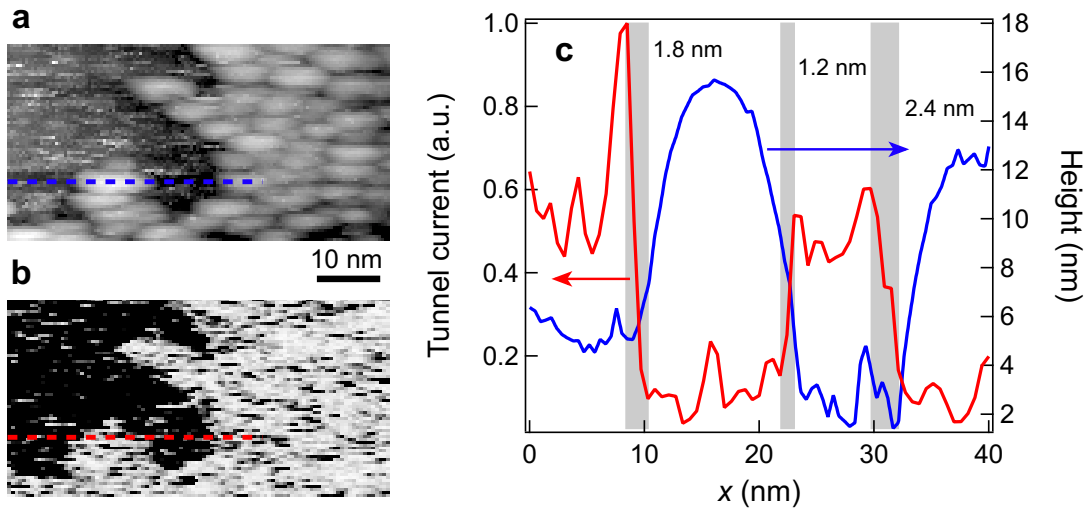
Figure 4.11 | Spatial resolution of the THz-STM. (a) STM topography of the Au nanostructures deposited on a HOPG substrate. The sample is prepared by sputtering method as described in Section 3.1. **(b)** The tunnel current map induced by a CEP-controlled THz electric field with $\phi_{CEP} = 0$ (set point: bias voltage $V_s = 50$ mV, tunnel current $I_s = 1$ nA). **(c)** line scans along the dashed lines shown in (a) and (b). The spatial resolution is estimated to be 1–2 nm by the edge definition of the Au nanostructures (grey-shaded regions).

induced by a CEP-controlled THz electric field with $\phi_{CEP} = 0$. The contrast between the Au nanostructures and HOPG area is due to the difference in their conductances at the tunnel junction. The HOPG surface is more conductive with respect to the THz electric field for the given conditions. The spatial resolution of our THz-STM is estimated to be 1–2 nm by line scans over the Au nanostructures, as shown in Figure 4.11c. Although our THz-STM is operated at ambient laboratory conditions, we could map the THz-field-induced tunnel current on a nanoscale which is far beyond the diffraction limit of THz pulses.

4.5 Discussion

Several theoretical models have been proposed to understand electron transport at a tunnel junction [12,27,34–37]. Ward *et al.* calculated electron transmission curves as a function of energy in an attempt to explain electron transport at a metal tunnel junction subjected to a CW visible laser having
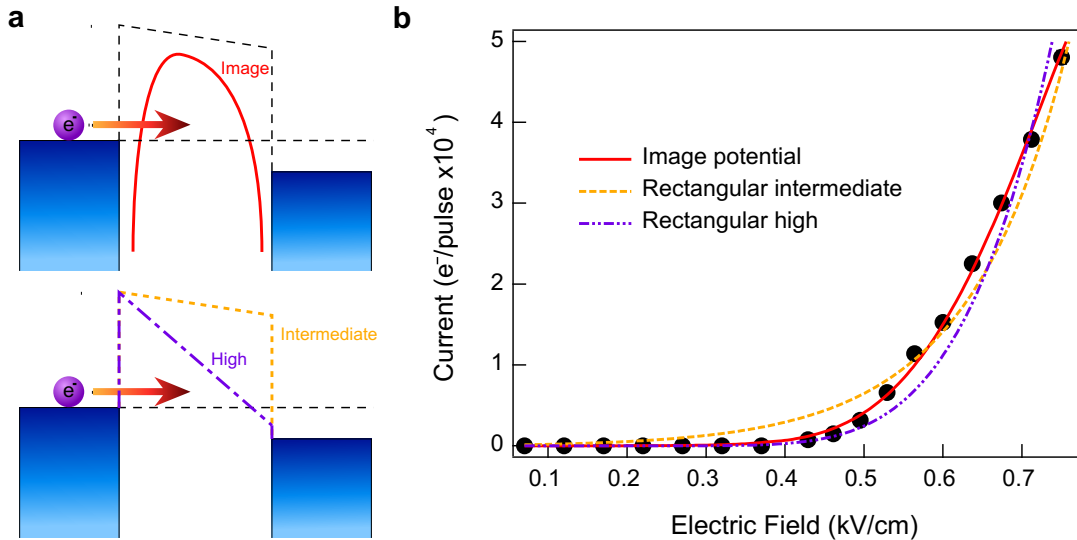
Figure 4.12 | Fitting the experimental data with different shape of potential barrier. (a) Schematic illustration of the potential barrier between a nanotip and a sample. The upper and lower images show the barrier with and without the image potential, respectively. **(b)** Number of rectified electrons induced by a single THz pulse without d.c. bias as a function of the peak electric field ($\phi_{CEP} = 0$). The solid curve shows the best fit obtained by the Simmons model with the image potential, while the dashed and dashed double-dotted curve indicate the best fit without the image potential.

high photon energy (1.58 eV) [12]. Since their calculation was based on the Landauer approach, the validity of this model is limited to the linear regime. This model is therefore not suitable for our THz-STM experiments which exhibit extremely nonlinear behaviour. The Tersoff and Humann model has been widely used to describe electron transport at a tunnel junction with 3D characteristics [34,35]. However, this model also assumes a low-voltage regime, making it inapplicable to our experiments. Another approach is the extended Simmons model [36], in which both the electrostatic and image potentials are modified to describe a STM junction with 3D characteristics. However, notational, geometrical, and electrical inconsistencies in the descriptions of the hyperboloidal electrodes and the electrostatic potential were pointed out by Ley-Koo [37].

Although the basic Simmons model is suitable for a tunnel junction with planar plates [27], we believe that this model is one of the better choices for understanding the physics underlying our THz-STM experiments with extremely nonlinear behavior, which is considerably different from that in conventional STM experiments. Because the photon-assisted tunneling is negligible owing to the low energy of the THz pulses (~ 4.2 meV), electron transmission might be accurately calculated using the WKB approximation in the Simmons model. Indeed, the results of THz-STM experiments with weak electric fields have been explained qualitatively by the Simmons model [15].

For the above reasons, we used the Simmons model [27] to analyse the motion of electrons in a tunnel junction, which is generally applicable to a d.c. condition. Because the time typically required for electron tunneling is less than 1 fs [32,38] and much shorter than the period of the driving field, the THz electric field transient acts as a quasi-static field. Therefore, the Simmons model can also be applied to our experimental results.

In order to investigate an appropriate potential barrier for THz-field-driven electrons, we fitted the experimental data with potential barriers having different shapes (Figure 4.12a), as described in Section 4.3. As shown by the solid curve in Figure 4.12b, the resulting best fit is only obtained by including an image potential with an effective work function of 3.8 ± 0.1 eV, a gap width of 1.00 ± 0.01 nm, and an enhancement factor of $100,000 \pm 10,000$. The obtained gap width is a reasonable value for a typical STM parameter. The

effective work function of 3.8 ± 0.1 eV is slightly lower than that of the nanotip and the sample [39,40] (~ 5 eV) because of the presence of adsorbates in the air [41]. The estimated enhancement factor indicates an extremely large THz electric field at the junction and is in reasonably good agreement with that at a single-molecule tunnel junction subjected to monochromatic CW-THz radiation [13], whose value is on the order of λ_{THz}/d (where λ_{THz} is the THz wavelength and d is the nm-scale gap width; 100 (µm)/ 1 (nm) = 100,000). The validity of the estimated parameters are further confirmed using two *I–Z* and d.c. *I–V* measurements, as described in Section 4.4.2, and summarized in Table 4.1.

	gap width	effective work function	enhancement factor
Simmons model	1.00 ± 0.01 nm	3.8 ± 0.1 eV	$100,000 \pm 10,000$
d.c. measurement	0.85 ± 0.17 nm	3.8 ± 0.1 eV	$100,000$

Table 4.1 | Summary of estimated parameters
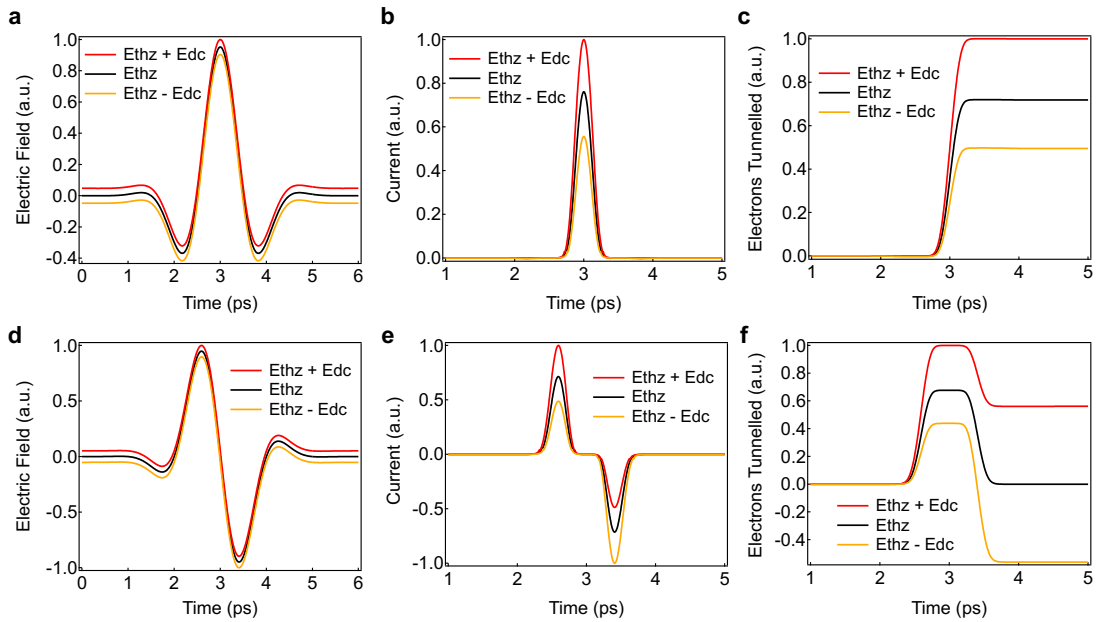
Figure 4.13 | d.c. bias dependence of the THz-induced electron tunnelling. **(a–c)**, Results of simulations with a THz electric field $\phi_{CEP} = 0$. **(a)** Calculated THz electric fields with different DC biases. **(b)** Tunnel currents obtained using the Simmons model. **(c)** Number of rectified electrons obtained by integration of the tunnel currents in (b). **(d–f)**, Corresponding results of simulations with a THz electric field $\phi_{CEP} = \pi/2$.

Using the Simmons model, we were able to obtain reasonable values for various parameters, strongly indicating that this model is satisfactory for understanding the physics underlying our experimental results. We expect that our experimental results will accelerate the establishment of elaborate theoretical models that can be used to investigate quantitatively the nonlinear transport of electrons at a junction in an extremely nonlinear regime.

We now discuss the d.c. bias dependence of THz-field-induced electron tunneling, as shown in Figure 4.7b. Under a d.c. bias, the total electric field at a tunnel junction with THz electric fields can be expressed as $E_{\text{THz}} + E_{\text{dc}}$. In order to reveal the d.c. bias dependence of the tunnel current, we performed simulations based on the Simmons model. Using the temporal profile of the THz electric fields ($\phi_{\text{CEP}} = 0$) with different d.c. biases (Figure 4.13a), the tunnel current and the number of rectified electrons at the junction were obtained as a function of time (Figures 4.13b and 4.13c). Note that the tunnel current increases nonlinearly only around the peak THz electric field ($t \sim 3$ ps) with increasing d.c. bias, leading to a rapid increase in the number of rectified electrons within a sub-picosecond time scale. The reverse polarity of the tunnel current and rectified electrons was expected when applying a THz electric field with $\phi_{\text{CEP}} = \pi$. Almost all the electrons contributed to the unidirectional
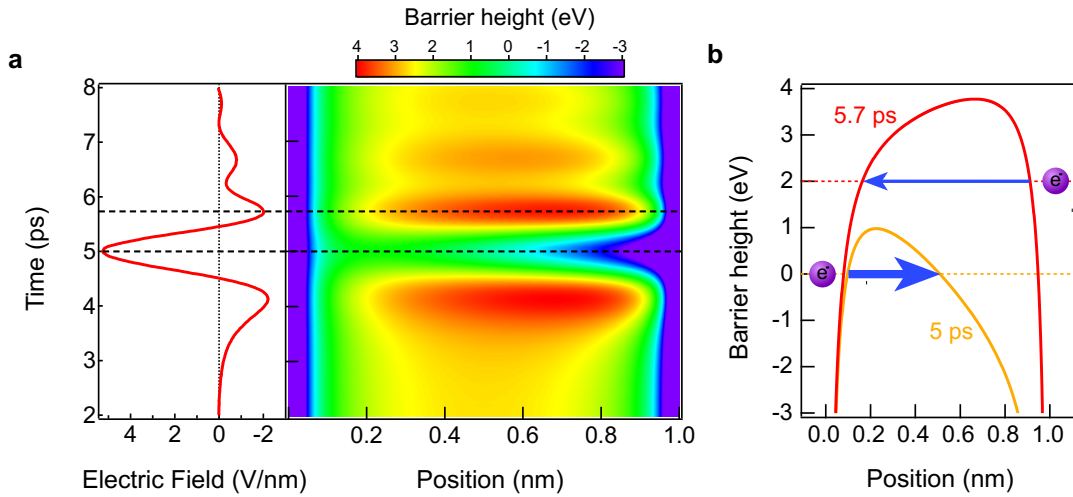
Figure 4.14 | Time-dependent modulation of the potential barrier. (a) Time dependence of potential barrier under an enhanced THz electric field. **(b)** Potential barriers at $t = 5$ and $t = 5.7$ ps, indicated by the dashed lines in (a). The electron undergoes tunneling in the smaller potential barrier at $t = 5$ ps rather than that at $t = 5.7$ ps, as shown by the thicker and thinner arrows, respectively. The thicker arrow indicates the higher probability of electron tunneling.

tunneling, reflecting the asymmetric single-cycle cosinusoidal THz waveform.

In a similar manner, the simulations were performed using the temporal profile of the THz electric field ($\phi_{\text{CEP}} = \pi/2$) with different d.c. biases (Figure 4.13d). The tunnel current flows for both polarities, reflecting the sinusoidal electric field. Upon applying a d.c. bias, however, the tunnel current becomes asymmetric owing to the strong nonlinearity of the tunnel junction (Figure 4.13e). As a result, after the THz electric field has passed through the junction ($t \sim 5$ ps), the number of rectified electrons and their direction can be tuned by the d.c. bias: electron tunneling is induced from the nanotip to the sample under a positive d.c. bias, and in the opposite direction under a negative d.c. bias. These calculations are in good agreement with the experimental results shown in Figure 4.7b.

In order to clarify the underlying physics of our experimental results, the time-dependent modulation of the potential barrier was also calculated using the Simmons model. As shown in Figure 4.13a, b, the potential barrier is coherently distorted by the enhanced THz electric field at the junction. For example, the barrier height is reduced to 0.98 eV whereas the barrier width decreases to 0.41 nm at the field strength of +5.3 V/nm. In contrast, a field strength of −2.0 V/nm causes the barrier to shrink less, with the height and width reduced to 1.78 eV and 0.75 nm, respectively. This potential asymmetry driven by the CEP-locked single-cycle THz electric field leads to unidirectional electron tunneling through the junction on the sub-picosecond timescale.

4.6   Summary and outlook

In summary, we have demonstrated real-space coherent manipulation of electrons in a single tunnel junction. CEP-controlled single-cycle THz electric fields, can be used to induce electron tunneling either from the nanotip to the sample or vice versa. The extremely large field enhancement at the junction strongly modulates the potential barrier between the nanotip and the sample, leading to the strong saturation of rectified electrons in a space-charge-limited regime. We believe that this concept provides a new platform for the ultrafast coherent control of electrons, and may lead to the design of new ultrafast lightwave nanoelectronics. Furthermore, our CEP-controlled THz-STM with an extremely high electric field is expected to be a powerful tool for exploring the ultrafast nonlinear control of matter [22] at the atomic scale.

References in chapter 4

[1]   G.G. Paulus, F. Lindner, H. Walther, A. Baltuska, E. Goulielmakis, M. Lezius, F. Krausz, Measurement of the phase of few-cycle laser pulses., Phys. Rev. Lett. 91 (2003) 253004.

[2]   P.B. Corkum, F. Krausz, Attosecond science, Nat. Phys. 3 (2007) 381–387.

[3]   A. Schiffrin, T. Paasch-Colberg, N. Karpowicz, V. Apalkov, D. Gerster, S. Mühlbrandt, M. Korbman, J. Reichert, M. Schultze, S. Holzner, J. V Barth, R. Kienberger, R. Ernstorfer, V.S. Yakovlev, M.I. Stockman, F. Krausz, Optical-field-induced current in dielectrics, Nature. 493 (2012) 70–74.

[4]   T. Paasch-Colberg, A. Schiffrin, N. Karpowicz, S. Kruchinin, Ö. Sağlam, S. Keiber, O. Razskazovskaya, S. Mühlbrandt, A. Alnaser, M. Kübel, V. Apalkov, D. Gerster, J. Reichert, T. Wittmann, J. V Barth, M.I. Stockman, R. Ernstorfer, V.S. Yakovlev, R. Kienberger, F. Krausz, Solid-state light-phase detector, Nat. Photonics. 8 (2014) 214–218.

[5]   T.T. Luu, M. Garg, S.Y. Kruchinin, A. Moulet, M.T. Hassan, E. Goulielmakis, Extreme ultraviolet high-harmonic spectroscopy of solids, Nature. 521 (2015) 498–502.

[6]   M. Hohenleutner, F. Langer, O. Schubert, M. Knorr, U. Huttner, S.W. Koch, M. Kira, R. Huber, Real-time observation of interfering crystal electrons in high-harmonic generation, Nature. 523 (2015) 572–575.

[7]   M. Krüger, M. Schenk, P. Hommelhoff, Attosecond control of electrons emitted from a nanoscale metal tip., Nature. 475 (2011) 78–81.

[8]   L. Wimmer, G. Herink, D.R. Solli, S. V Yalunin, K.E. Echternkamp, C. Ropers, Terahertz control of nanotip photoemission, Nat. Phys. 10 (2014) 432–436.

[9]   B. Piglosiewicz, S. Schmidt, D.J. Park, J. Vogelsang, P. Groß, C. Manzoni, P. Farinello, G. Cerullo, C. Lienau, Carrier-envelope phase effects on the strong-field photoemission of electrons from metallic nanostructures, Nat. Photonics. 8 (2014) 37–42.

[10]   H.J. Caulfield, S. Dolev, Why future supercomputing requires optics, Nat. Photonics. 4 (2010) 261–263.

[11] F. Krausz, M.I. Stockman, Attosecond metrology: from electron capture to future signal processing, Nat. Photonics. 8 (2014) 205–213.

[12] D.R. Ward, F. Hüser, F. Pauly, J.C. Cuevas, D. Natelson, Optical rectification and field enhancement in a plasmonic nanogap, Nat. Nanotechnol. 5 (2010) 732–736.

[13] K. Yoshida, K. Shibata, K. Hirakawa, Terahertz Field Enhancement and Photon-Assisted Tunneling in Single-Molecule Transistors, Phys. Rev. Lett. 115 (2015) 138302.

[14] Y.-M. Bahk, B.J. Kang, Y.S. Kim, J.-Y. Kim, W.T. Kim, T.Y. Kim, T. Kang, J. Rhie, S. Han, C.-H. Park, F. Rotermund, D.-S. Kim, Electromagnetic Saturation of Angstrom-Sized Quantum Barriers at Terahertz Frequencies, Phys. Rev. Lett. 115 (2015) 125501.

[15] T.L. Cocker, V. Jelic, M. Gupta, S.J. Molesky, J.A.J. Burgess, G.D.L. Reyes, L. V. Titova, Y.Y. Tsui, M.R. Freeman, F.A. Hegmann, An ultrafast terahertz scanning tunnelling microscope, Nat. Photonics. 7 (2013) 620–625.

[16] R. Vincent, S. Klyatskaya, M. Ruben, W. Wernsdorfer, F. Balestro, Electronic read-out of a single nuclear spin using a molecular spin transistor., Nature. 488 (2012) 357–60.

[17] A. Sharma, V. Singh, T.L. Bougher, B.A. Cola, A carbon nanotube optical rectenna., Nat. Nanotechnol. 10 (2015) 1027–1032.

[18] K.J. Savage, M.M. Hawkeye, R. Esteban, A.G. Borisov, J. Aizpurua, J.J. Baumberg, Revealing the quantum regime in tunnelling plasmonics., Nature. 491 (2012) 574–7.

[19] S.F. Tan, L. Wu, J.K.W. Yang, P. Bai, M. Bosman, C.A. Nijhuis, Quantum Plasmon Resonances Controlled by Molecular Tunnel Junctions, Science. 343 (2014) 1496–1499.

[20] S. Grafström, Photoassisted scanning tunneling microscopy, J. Appl. Phys. 91 (2002) 1717.

[21] H. Hirori, A. Doi, F. Blanchard, K. Tanaka, Single-cycle terahertz pulses with amplitudes exceeding 1 MV/cm generated by optical rectification in $LiNbO_3$, Appl. Phys. Lett. 98 (2011) 091106.

[22] T. Kampfrath, K. Tanaka, K.A. Nelson, Resonant and nonresonant control over matter and light by intense terahertz transients, Nat. Photonics. 7 (2013) 680–690.

[23] K. Yoshioka, Y. Minami, K. Shudo, T.D. Dao, T. Nagao, M. Kitajima, J. Takeda, I. Katayama, Terahertz-Field-Induced Nonlinear Electron Delocalization in Au Nanostructures, Nano Lett. 15 (2015) 1036–1040.

[24] Y. Terada, S. Yoshida, O. Takeuchi, H. Shigekawa, Real-space imaging of transient carrier dynamics by nanoscale pump–probe microscopy, Nat. Photonics. 4 (2010) 869–874.

[25] S. Yoshida, Y. Aizawa, Z.-H. Wang, R. Oshima, Y. Mera, E. Matsuyama, H. Oigawa, O. Takeuchi, H. Shigekawa, Probing ultrafast spin dynamics with optical pump-probe scanning tunnelling microscopy., Nat. Nanotechnol. 9 (2014) 588–593.

[26] S. Feng, H.G. Winful, Physical origin of the Gouy phase shift., Opt. Lett. 26 (2001) 485–487.

[27] J.G. Simmons, Generalized Formula for the Electric Tunnel Effect between Similar Electrodes Separated by a Thin Insulating Film, J. Appl. Phys. 34 (1963) 1793–1803.

[28] D. Bohm, Quantum Theory, (Courier Dover Publications) 1951.

[29] N.M. Miskovsky, P.H. Cutler, T.E. Feuchtwang, A.A. Lucas, The multiple-image interactions and the mean-barrier approximation in MOM and MVM tunneling junctions, Appl. Phys. A Solids Surfaces. 27 (1982) 139–147.

[30] J.-Y. Kim, B.J. Kang, J. Park, Y.-M. Bahk, W.T. Kim, J. Rhie, H. Jeon, F. Rotermund, D.-S. Kim, Terahertz Quantum Plasmonics of Nanoslot Antennas in Nonlinear Regime, Nano Lett. 15 (2015) 6683–6688.

[31] G.M. Shedd, P. Russell, The scanning tunneling microscope as a tool for nanofabrication, Nanotechnology. 1 (1990) 67–80.

[32] P. Zhang, Scaling for quantum tunneling current in nano- and subnano-scale plasmonic junctions, Sci. Rep. 5 (2015) 9826.

[33] M. Shalaby, C.P. Hauri, Demonstration of a low-frequency three-dimensional terahertz bullet with extreme brightness, Nat. Commun. 6 (2015) 5976.

[34] J. Tersoff, D. Hamann, Theory and application for the scanning tunneling microscope, Phys. Rev. Lett. 50 (1983) 1998–2001.

[35] J. Tersoff, D.R. Hamann, Theory of the scanning tunneling microscope, Phys. Rev. B. 31 (1985) 805–813.

102

[36] G. Seine, R. Coratger, A. Carladous, F. Ajustron, R. Pechou, J. Beauvillain, Tip-to-surface distance variations vs voltage in scanning tunneling microscopy, Phys. Rev. B. 60 (1999) 11045–11050.

[37] E. Ley-Koo, Comment on "Tip-to-surface distance variations vs voltage in scanning tunneling microscopy," Phys. Rev. B. 65 (2002) 077401.

[38] A.S. Landsman, U. Keller, Attosecond science and the tunnelling time problem, Phys. Rep. 547 (2015) 1–24.

[39] H.L. Skriver, N.M. Rosengaard, Surface-Energy and Work Function of Elemental Metals, Phys. Rev. B. 46 (1992) 7157–7168.

[40] S. Suzuki, C. Bower, Y. Watanabe, O. Zhou, Work functions and valence band states of pristine and Cs-intercalated single-walled carbon nanotube bundles, Appl. Phys. Lett. 76 (2000) 4007.

[41] C.J. Chen, Introduction to Scanning Tunneling Microscopy, (Oxford Univ. Press) 2008.

Chapter 5

Retrieving and Tailoring Single-Cycle THz Near Field in a Tunnel Junction

Light-field-driven processes occurring under conditions far beyond the diffraction limit of the light can be manipulated by harnessing spatiotemporally tunable near fields. A tailor-made carrier envelope phase in a tunnel junction formed between nanogap electrodes allows precisely controlled manipulation of these processes. In particular, the characterization and active control of near fields in a tunnel junction are essential for advancing elaborate manipulation of light-field-driven processes at the atomic-scale. Here, we demonstrate that desirable phase-controlled near fields can be produced in a tunnel junction via terahertz scanning tunneling microscopy (THz-STM) with a phase shifter. Measurements of the phase-resolved subcycle electron tunneling dynamics revealed an unexpected large carrier-envelope phase shift between far-field and near-field single-cycle THz waveforms. The phase shift stems from the wavelength-scale feature of the tip–sample configuration. By using a dual-phase double-pulse scheme, electron tunneling was coherently manipulated over the femtosecond time scale. Our new prescription — in-situ tailoring of single-cycle THz near fields in a tunnel junction — will offer unprecedented control of electrons for ultrafast atomic-scale electronics and metrology.

5.1 Introduction

Strong-field interactions of light with matter have recently attracted significant attention [1–9]. The strong field produced by few-cycle ultrashort laser pulses can control the motion of electrons in the nonperturbative regime. In this regime, precise control of the carrier-envelope phase (CEP) of ultrashort laser pulses enables: the steering of light-field-driven currents in solid-state systems, [1,2] high-harmonic generation of attosecond pulses [3], and the chemical reaction of molecules [4,5] at the subcycle timescale. Focusing of CEP-controlled ultrashort laser pulses beyond the diffraction limit will provide fascinating avenues for manipulating light-field-driven processes in the ultrafast and ultrasmall regime. The development of strong-field physics has been greatly facilitated by locally-enhanced near fields in nanostructures [10–18]. Near-field-mediated electron manipulations with CEP-controlled laser pulses have been demonstrated for electron emission from metal nanotips [10,11] and dielectric nanospheres [12,13]. The use of nanostructures provides the large field enhancement and nanoscale confinement of light beyond the diffraction limit. However, the laser fields employed in these studies were limited, owing to their geometry, to inducing photoemission from materials.

Light-field-driven quantum tunneling between nanogap electrodes using phase-locked single-cycle pulses has recently emerged as a new method for ultrafast coherent control of electrons at the nanoscale. CEP-dependent electron tunneling in near-infrared (NIR) [19] and terahertz (THz) [20] spectral ranges as well as atomic-resolution imaging of ultrafast dynamics via terahertz scanning tunneling microscopy (THz-STM) [21,22] have been reported. Conventional STM is applicable to any type of conducting material, such as superconductors, [23] magnetic materials, [24] and two-dimensional nanomaterials [25]. Therefore, THz-STM with CEP-controlled single-cycle THz pulses will pave the way for a new phase of ultrafast atomic-scale research, including spatiotemporal manipulations of phase transitions [26,27], coherent spin dynamics [28], and chemical reactions [29]. Precise characterization and active control of near fields in a tunnel junction with subcycle resolution are therefore crucial for advancing these next-generation light-field-driven manipulations.

Streaking spectroscopy, originally developed for atomic systems and commonly used in attosecond science [30,31], constitutes a promising means of

visualizing optical near fields in nanostructures. In fact, for both THz [15] and NIR [16] pulses, this technique has been successfully applied to the retrieval of optical near fields at the apex of a nanoscale metal tip. This retrieval relies on a dual-wavelength double-pulse scheme with different pulse durations and ponderomotive energies. The photoemitted electrons initiated by a pulse with a relatively short wavelength and pulse duration were accelerated by the near field of a long wavelength phase-locked pulse with large ponderomotive energy. However, streaking spectroscopy is inapplicable to a tunnel junction as the electron transfer occurs only between nanogap electrodes via quantum tunneling activated by the electric field of light. Electron removal from the junction is therefore impossible.

An experimental method for reconstructing single-cycle near fields remains elusive and, hence, previous studies [21,22,32] have assumed that THz far fields and near fields in a tunnel junction are identical. In the present study, we demonstrate the subcycle retrieval of THz near fields in a tunnel junction using a combination of THz-STM and a CEP shifter [33]. Regardless of the nanotip shape, we could implement in-situ tailoring of single-cycle THz near fields in the junction. We also achieved precise control of the electron tunneling over the femtosecond time scale by employing a Mach-Zehnder interferometer with a dual-phase double-pulse scheme.

5.2 Experimental setup

Figure 5.1 shows our experimental setup. Single-cycle THz electric field transients were generated using a $LiNbO_3$ prism in a tilted-pulse-front configuration [34]. The generated THz pulses were collimated by a gold-coated off-axis parabolic mirror (PM1), and then introduced into a Mach-Zehnder interferometer characterized by a dual-phase double-pulse scheme. The THz pulse was further split into two beams, using an anti-reflection coated silicon beam splitter (Si BS1), which were then used as CEP-controlled and delay-controlled THz pulses. For the CEP-controlled pulses, we used a CEP shifter (applicable to broadband THz pulses) consisting of a quarter-wave plate (THz QWP), a half-wave plate (THz HWP) and a wire grid polarizer (WG1) [33,35]. The field strength of the THz pulses was tuned using a pair of wire grid polarizers (WG2 and WG4). For the delay-controlled THz pulses, the field strength was tuned using two wire grid polarizers (WG3 and WG4) after

passing through a delay stage (DS). The CEP-controlled and delay-controlled pulses were subsequently combined using an anti-reflection coated silicon beam splitter (Si BS2). We used silicon wafers with different thicknesses (Si BS1 and Si BS2) in order to provide adequate reduction of the field strengths associated with the multi-reflection pulses (<20% of the main pulse). The waveform-controlled double THz pulses were then guided into one of two paths by either removing or inserting a removable gold-coated mirror; one path was used for characterizing the THz pulses via electro-optic sampling (EOS) and the other was used for delivering the pulses to a tunnel junction of the STM. For the EOS, we confirmed that identical waveforms occurred for 2-mm-thick ZnTe (110), 1-mm-thick ZnTe (110) and 0.4 mm-thick GaP (110) crystals. The THz pulse energy was calculated by integrating the THz intensity both temporally and spatially [36]. In order to accurately characterize the THz waveform at the junction, identical off-axis parabolic mirrors (PM2 and PM3; focal length: 4 inches, diameter: 2 inches) were used to focus the THz pulses. The resulting beam diameter at both the STM junction and the EO crystal was
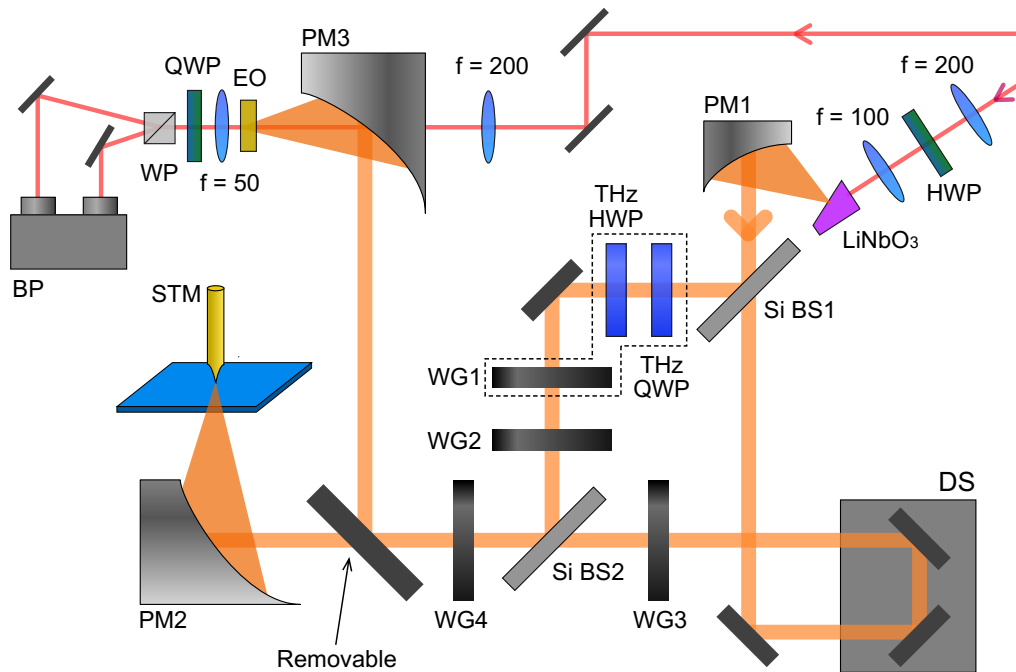

Figure 5.1 | Experimental setup for THz-STM. Si BS: silicon beam splitter, DS: delay stage, QWP: quarter-wave plate, HWP: half-wave plate, PM: parabolic mirror, WG: wire grid polarizer, EO: electro-optic crystal, WP: Wollaston prism, BP: balanced photodiode. A component of the CEP shifter is enclosed by the dotted line.

1.2 mm.

The THz tunnel current was recorded by a real-time digital oscilloscope (Tektronics DPO71254C) via the STM circuits. THz pulses were chopped at 500 Hz and the feedback loop was switched on and off at a frequency of 20 Hz. The CEP-dependent tunnel current (Figure 5.2d) was measured by rotating the THz HWP by 180°, which corresponds to a CEP shift of 2π. The data was measured within 4 seconds and the feedback loop remained off during the measurement.

5.3 Measurement and simulation results

5.3.1 Sub-cycle spectroscopy of electron tunneling

Our experimental setup is illustrated schematically in Figure 5.2a. Highly oriented pyrolytic graphite (HOPG) was used as a sample, owing to its atomically flat surface. The generated THz pulses were guided into a CEP shifter, which was composed of three optical elements (a quarter-wave plate, half-wave plate, and wire-grid polarizer) for broadband THz pulses. The CEP of the THz pulses that pass through the CEP shifter is given by $\phi_{CEP} = \phi_{CEP0} + 2\alpha$, where ϕ_{CEP} and ϕ_{CEP0} are the output and initial CEPs, respectively, and α is the azimuth angle of the half-wave plate. CEP adjustment either through the insertion of a pair of fused-silica wedges [1,2,4,11,12,19] or spherical and cylindrical lenses leads to variations in the time delay, pulse duration, and frequency component. However, the CEP shifter enables precise control of the CEP with values that change continuously from 0 to 2π without the occurrence of these variations, as shown in Figure 5.2, parts b and c. The CEP of single-cycle THz pulses tuned by the CEP shifter is highly stable, owing to the robustness of our optical setup and the steady ϕ_{CEP} value passively locked through the optical rectification. Furthermore, the CEP-controlled single-cycle THz pulses were focused onto the apex of a Pt/Ir nanotip. By irradiating a tunnel junction with these pulses while continuously tuning the CEP by 2π, we could observe a series of CEP-dependent tunnel currents using an oscilloscope (see Figure 5.2d). The time interval of each current pulse (2 ms) is equal to the repetition rate of the irradiated pulses. The time-integrated value of each current pulse at a given CEP represents the number of electrons driven by a phase-controlled single-cycle THz pulse through the junction.
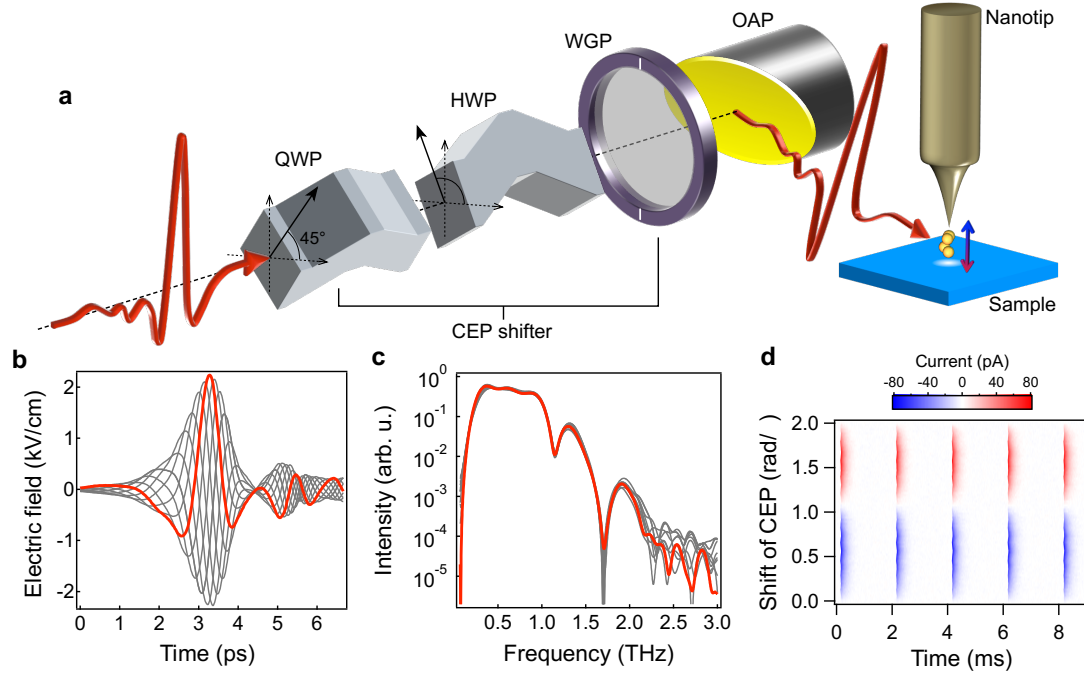
Figure 5.2 | Concept of the measurement. (a) Schematic of the experimental setup; QWP, quarter-wave plate; HWP, half-wave plate; WGP, wire grid polarizer; OAP, off-axis parabolic mirror. CEP-and polarization- controlled single-cycle THz electric fields are focused onto the apex of a Pt/Ir nanotip with an incident angle of 75°. **(b)** Far-field single-cycle THz waveforms with different CEPs measured via electro-optic sampling (EOS). The dotted gray lines show the CEP-controlled waveforms for each $(2/9)\pi$ shift. **(c)** THz frequency spectra obtained through Fourier transformation of part (b). **(d)** THz-driven tunnel currents as a function of the CEP shift of a THz electric field without a direct current (d.c.) bias. The feedback loop remained off during the measurement (set point: bias voltage $V_s = 1$ V; tunnel current $I_s = 0.1$ nA).

Figure 5.3a shows the number of electrons as a function of CEP with different THz pulse energies. The direction and number of electrons tunneling through the junction are strongly dependent on the CEP. The number of rectified electrons is maximized at 0.67π for electrons tunneling from the nanotip to the sample and at 1.67π for tunneling in the opposite direction. In these cases, the THz waveform in the junction is expected to be a single-cycle cosinusoidal near field; the near field with either positive or negative polarity induces the unidirectional tunnel current, indicating the symmetry-breaking of electric transport. In contrast, the number of rectified electrons is minimized at 0.06π,
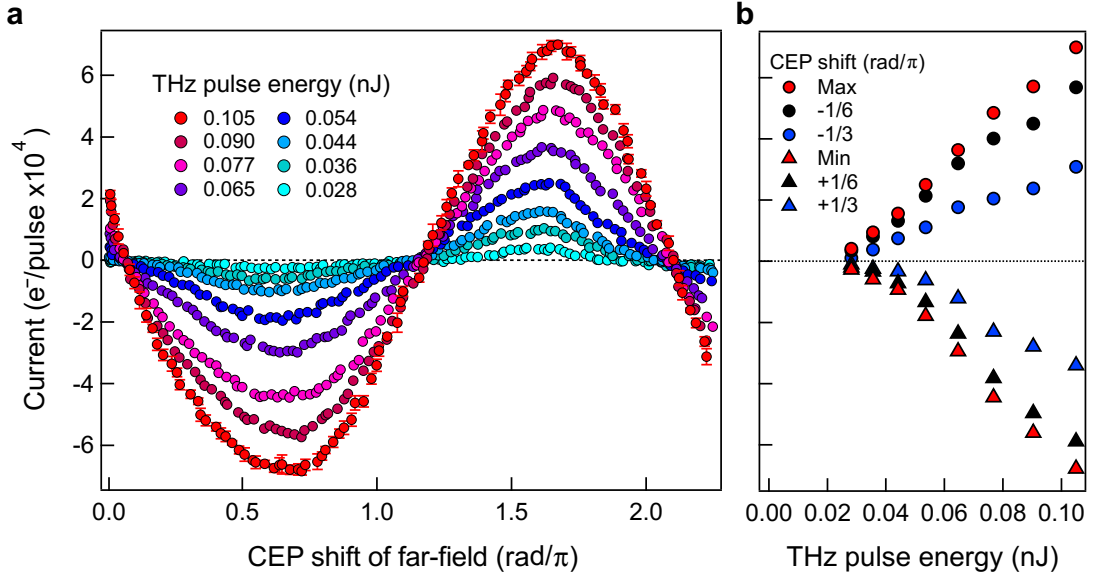
Figure 5.3 | CEP and power dependence of THz-field-induced electron tunneling. (a) Number of electrons driven by a single THz pulse as a function of the CEP with different THz pulse energies ($V_s = 1$ V; $I_s = 0.1$ nA). The electrons undergo tunneling from the nanotip to the sample with positive values, and from the sample to the nanotip for negative values. **(b)** Increase in the number of electrons with THz pulse energy associated with **(a)**. The THz pulse energy was calculated from the corresponding THz waveform by integrating the waveform intensity both temporally and spatially.

1.17π, and 2.11π, corresponding to a sinusoidal near field in the junction; the near field with symmetric positive and negative polarities drives the bidirectional tunnel current with the same number of electrons. An increase in the number of electrons with THz pulse energy exhibits threshold-like nonlinear behavior, as shown in Figure 5.3b, owing to the strong modulation of the potential barrier in the junction (as discussed in Chapter 4). This CEP-dependent nonlinear increase in the electron tunneling indicates that the electron transfer originates from the THz-field-driven process. Therefore, the tunneling current exhibits a strong dependence on the CEP of THz near fields.

5.3.2 Retrieving THz near field in a tunnel junction

We investigated the THz near fields in the junction by comparing them with their far-field waveforms. These waveforms were obtained experimentally via EOS, and the number of electrons driven by the far fields was calculated using the Simmons model [37]. During these calculations, the THz-field-induced

subcycle modulation of a potential barrier with an image potential was taken into consideration. The values of the effective work function and gap width (3.8 eV and 1.0 nm, respectively) used in the calculation were both obtained from current-distance (*I–Z*) experiments with a d.c. electric field (discussed in Chapter 4). Here, the THz electric field was treated as a quasi-static field because the *I–V* response in the THz regime is the same as that in the d.c. regime.

The results for three different nanotips (Tip 1, Tip 3, and Tip 5, see Figure
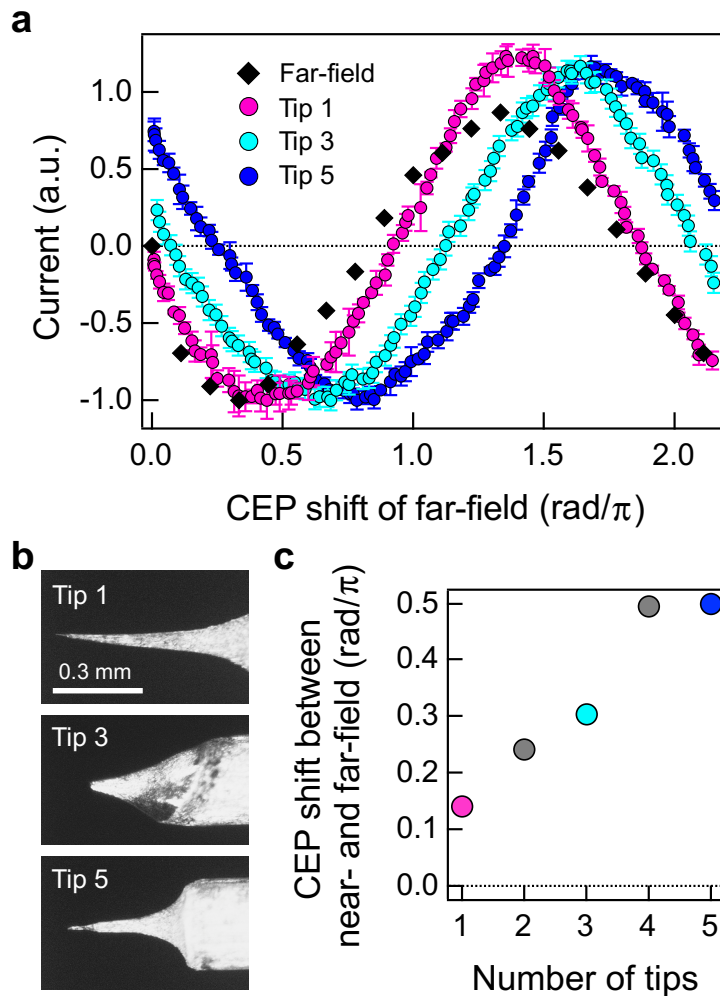
Figure 5.4 | Tip-dependent CEP shift of THz near field. (a) CEP-resolved rectified electrons with different nanotips (V_s = 1 V; I_s = 0.1 nA). The CEP-resolved rectified electrons induced by the corresponding far field, calculated using the Simmons model, is also shown. **(b)** Optical micrographs of the electrochemically etched Pt/Ir nanotips used **in** (a). **(c)** CEP shift of each THz near field for five different nanotips. The colored symbols correspond to the data shown in (a).

5.4) are shown in Figure 5.4a. As the figure shows, the CEP dependence of electrons rectified by the single-cycle THz near field of each nanotip differs completely from that rectified by the corresponding single-cycle THz far field. This dependence varies significantly with the shape of the nanotips. Measurements revealed a maximum CEP shift of $\pi/2$ between the near and far fields; this shift was ignored in previous studies [20–22,32]. The results for five different nanotips are summarized in Figure 5.4c. The large CEP shift can be
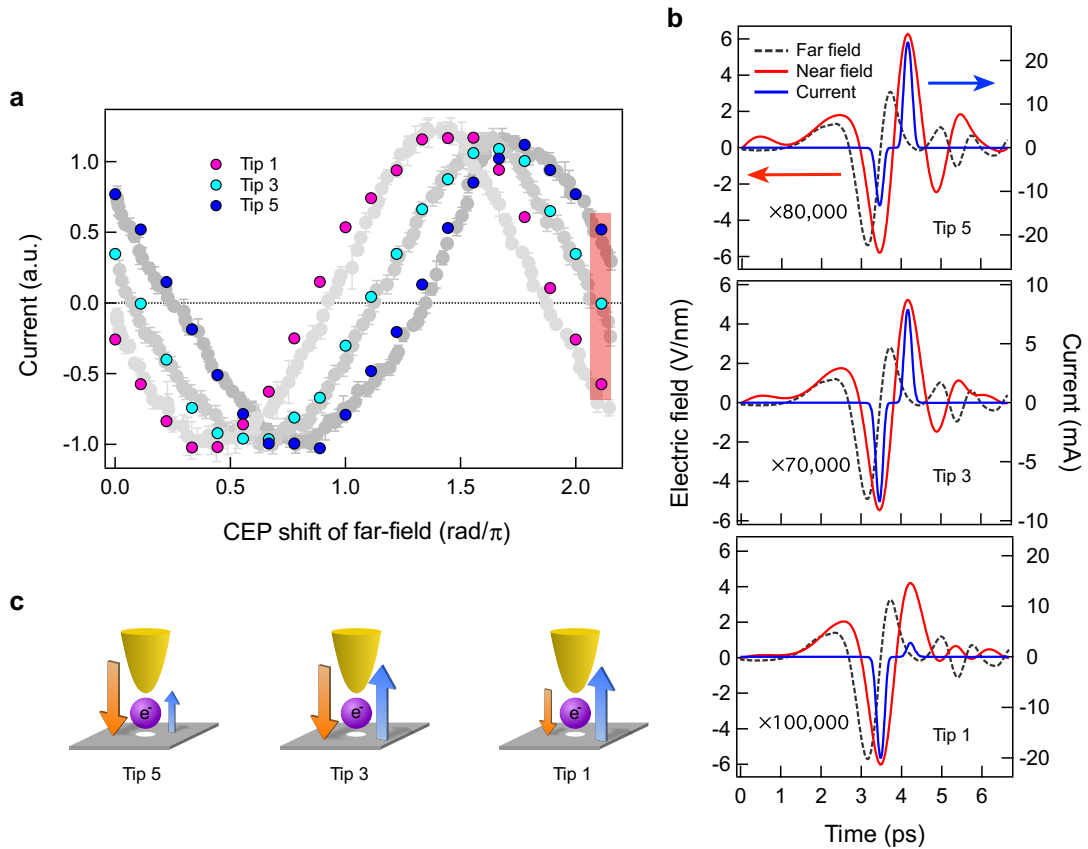
Figure 5.5 | Retrieving THz near field in the tunnel junction. (a) CEP-resolved rectified electrons calculated from the antenna model. The simulation parameters are summarized in the Section 5.4. The gray circles denote the measured CEP-resolved rectified electrons (corresponding to Figure 5.4a). **(b)** Tip dependence of far-field and near-field waveforms, and that of the resulting tunnel currents, at a CEP shift of 2.1π rad (highlighted by the red rectangle in **(a)**). For comparison with the near field, the far field was magnified by field enhancement factors ranging from 70 000 to 100 000. **(c)** Schematic illustration of the electron tunneling driven by each near-field for different nanotips. The orange and blue arrows show the tunneling direction. The bigger arrow indicates the higher probability of tunneling occurring.

113

attributed to the antenna properties induced by local fields at the apex of a nanotip [15,38,39].

We simulated the THz near field in the junction by using an antenna model that assigns an equivalent RLC circuit to the nanotip. As Figure 5.4a shows, the results correspond closely to the experimental data, which were calculated using the corresponding far-field waveform and adjustable circuit parameters depending on the nanotip. The detail of calculations will be given in Section 5.4. The difference in the CEP shift of the nanotips arises from the difference in resonance frequency and resistance, which depend primarily on the overall shape of the nanotip. Although the far-field waveform is identical for each of the nanotips, the resulting THz near field and subsequent electron current depend strongly on the nanotip (Figure 5.5b). Reproduction of the enhanced near-field waveform in the junction is difficult and requires more than simply multiplying the corresponding far-field waveform by each field enhancement factor. Consequently, the direction of electron tunneling depends on the nanotip (Figure 5.5c). In the case of Tip 1, the small CEP shift leads to electron transfer in the same direction as that expected for the far-field waveform. In the case of Tip 5, however, the transfer occurs in the opposite direction due to the large CEP shift. In the case of Tip 3, electrons flow equally in each direction, owing to the sinusoidal-shaped near field with a moderate CEP shift.

5.3.3   Finite integration simulation
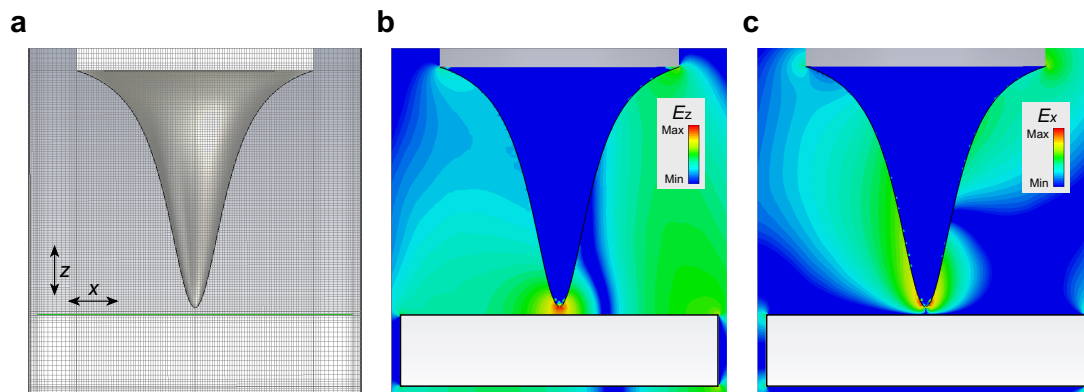
**Figure 5.6 | Setup for finite integration simulation. (a)** Finite element mesh with grid size of 2.5 μm × 2.5 μm × 2.5 μm. **(b,c)** Snapshot of *z* (b) and *x* (c) component of THz near field when the peak of THz electric field reaches the nanotip apex.

A three-dimensional (3D) finite element calculation was performed using commercially available software (CST MW STUDIO) in order to simulate the THz near-field waveform in a tunnel junction. The effect of macroscopic nanotip geometry was investigated using a Lorentzian function to model the nanotip shape. A grid size of 2.5 μm × 2.5 μm × 2.5 μm and a gap width of 10 μm were used as shown in Figure 5.6a. The *p*-polarized THz radiation was incident from a source plane with a uniform field distribution and an incident angle of 75°. The Lorentzian-shaped tip and a sample were modeled as perfect electric conductors. Snapshots of the *z* and *x* components of the THz near field
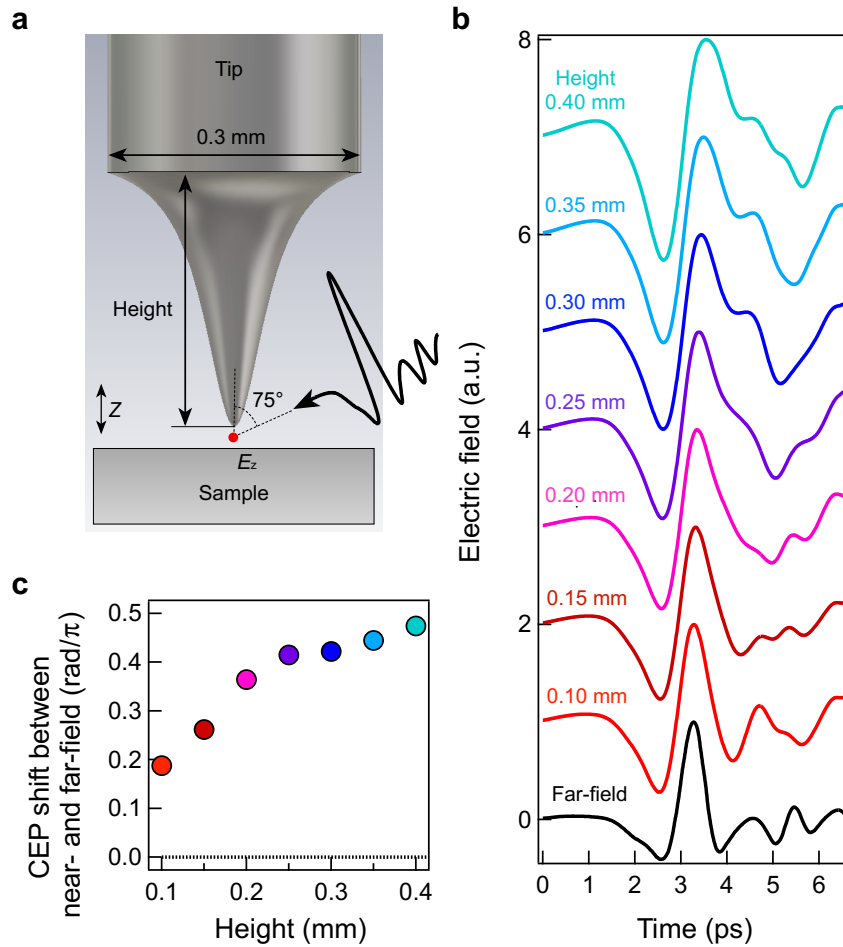
Figure 5.7 | Simulation of the tip-dependent CEP shift. (a) Tip–sample configuration with a gap width of 10 μm. The waveform of far-field THz electric fields was measured via electro-optic sampling (Figure 5.2b). **(b)** Far- and near-field waveforms with different tip heights. For clarity, each waveform was normalized at the maximum peak electric field and offset by unity. **(c)** CEP shift between each THz near field and far field as a function of the tip height.

distribution when the peak of THz electric field reaches the nanotip apex are shown in Figure 5.6b and c. The time evolution of the THz electric field was calculated at the midpoint between the nanotip and the sample. For a thorough understanding of the tip-dependent CEP shift, as shown in Figure 5.4c, we investigated the effect of the nanotip's macroscopic features.

Figure 5.7a shows the tip–sample configuration used in the simulation. The tip shape was assumed to be a Lorentzian with different heights. We confirmed that the waveform of the local electric field was insensitive to gap distances ranging from 1.0 nm to 10 μm (see the discussion in Section 5.4 for more details). Therefore, the gap distance between the tip and a sample was set to 10 μm. We used an actual THz far-field waveform measured via EOS. As shown in Figure 5.7b, the THz near-field waveform depends strongly on the tip shape, indicating that the tip-dependent CEP shift observed in the experiment results from the macroscopic shape of the tip. The tip with lower height is characterized by a cosinusoidal shape, while the tip with higher height is characterized by a sinusoidal shape. The estimated CEP shift between the far and near fields is summarized in Figure 5.7c. The CEP shift increases up to 0.47π with tip height, consistent with the observed range of the CEP shift. Roughly speaking, the tip with lower height behaves only as a scattered medium having almost no phase shift. However, the tip with the wavelength-scale height behaves as an antenna and therefore yields a large phase shift of $\sim 0.5\pi$. This indicates that the antenna effect becomes weaker when the tip geometry becomes small compared to the incident THz wavelength.

5.3.4 Dual-phase double-pulse experiment

In order to reveal the ultrafast dynamics of near-field-mediated electron tunneling with subcycle time resolution, we employed a Mach-Zehnder interferometer, with a dual-phase double-pulse scheme. This interferometer has an additional delay-controlled THz pulse with a fixed CEP (see Experimental setup, Section 5.2), as schematically illustrated in Figure 5.8a. The timing and direction of the electron tunneling were controlled and observed over a femtosecond time scale, as shown in Figure 5.8, parts b and c. Furthermore, the CEP-controlled first pulse was adjusted to yield either a sinusoidal (Figure 5.8b) or cosinusoidal (Figure 5.8c) near field, as shown in

116
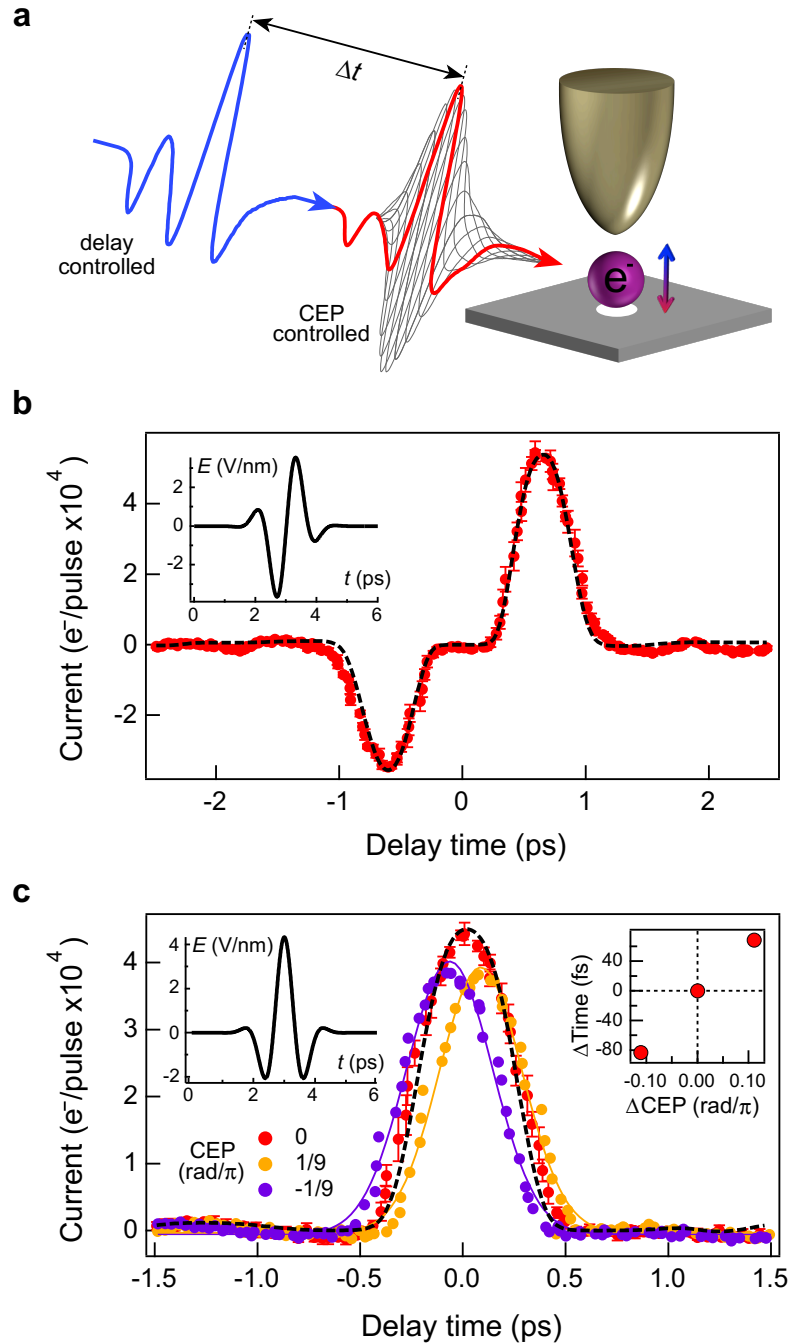
Figure 5.8 | Femtosecond control of electron tunneling with dual-phase double-pulse. (a) Schematic of the experimental concept. An additional single-cycle THz pulse with a fixed CEP was used with a given delay time from a CEP-controlled single-cycle THz pulse. **(b)** Number of electrons as a function of the delay time with sinusoidal near fields as shown in the inset waveforms ($V_s = 1$ V, $I_s = 0.1$ nA). **(c)** Number of electrons as a function of the delay time with cosinusoidal near fields as shown in the inset waveforms ($V_s = 1$ V, $I_s = 0.1$ nA). The dashed curves show the best fit obtained by the Simmons model. The inset in **(c)** shows the temporal shift of the current burst resulting from CEP tuning.

the insets. In the case of the sinusoidal near field, a bidirectional subpicosecond electron burst was generated with an interval of 1.2 ps; and in the case of the cosinusoidal near field, a unidirectional electron burst was produced with a pulse duration (full width at half-maximum) of 490 fs. These electron bursts are accurately reproduced (as indicated by the dashed lines in Figure 5.8, parts b and c) by the Simmons model (corresponding waveform shown in the insets). This ultrafast electron burst is highly sensitive to the CEP. As shown in the right inset of Figure 5.8c, the peak position of the electron burst is shifted by $+70$ and -80 fs for CEP shifts of $(1/9)\pi$ and $-(1/9)\pi$, respectively. This indicates that our method can also manipulate the near-field-mediated electron dynamics in a tunnel junction with femtosecond time resolution. In fact, this precise active control of both the near-field waveform and the resulting electron tunneling is unattainable without our stable and robust THz-STM equipped with a CEP shifter. This shifter can control the desired CEP for THz near fields without additional delay and chirp.

  We believe that our double-pulse scheme with tailor-made THz near fields will provide unique capability for future subcycle time-resolved experiments in a tunnel junction, for example, by selectively accessing specific energy levels such as HOMO and LUMO states in molecules [21] and the superconducting gap in superconductors [23].

5.4   Discussion

The CEP of near fields in the junction is strongly dependent on the shape of the nanotip (Figure 5.4). Therefore, we assume that the CEP shift results from the configurational resonance of a nanotip, as discussed in previous scanning near-field optical microscopy [38,39] and THz streaking spectroscopy investigations of a nanotip [15]. In those studies, the THz near field in the junction was phenomenologically simulated using a generic antenna-model [38], where an equivalent RLC circuit was assigned to the nanotip. The relationship between the THz near field at the tip apex $E_{\mathrm{near}}(t)$ and the current $I_{\mathrm{THz}}(t)$ in an antenna is given as follows:

$$E_{\mathrm{near}}(t) \propto \int_{-\infty}^{t} I_{\mathrm{THz}}(t')dt' . \qquad (5.1)$$

Similarly, the induced current $I_{\mathrm{THz}}(\omega)$ in the frequency domain is expressed as:

$$I_{\mathrm{THz}}(\omega) \propto \frac{E_{\mathrm{far}}(\omega)}{\left(R + j\omega L - j/(\omega C)\right)}, \tag{5.2}$$

where $E_{\mathrm{far}}(\omega)$, R, L, and C are the incident THz far field, radiation resistance, inductance, and capacitance, respectively. The resonance frequency is determined from $f_0 = 1/(2\pi\sqrt{LC})$. The THz near field in the junction can be retrieved by adjusting the three reactive parameters, thereby yielding the experimental results shown in Figure 5.5a. The simulation parameters used for Tip 1, Tip 3, and Tip 5 are summarized in Table 5.1. The results obtained correspond closely to the experimental data, as evidenced by reasonable parameter values, which are similar to those used for THz streaking spectroscopy at a nanotip [15].

	Tip 1	Tip 3	Tip 5
R	350 Ω	300 Ω	220 Ω
L	0.100 nH	0.126 nH	0.120 nH
C	0.620 fF	0.434 fF	0.448 fF

Table S1 | Simulation parameters for different nanotips.

We used different effective work functions between the sample and the nanotip to reproduce the asymmetry of the observed CEP-resolved tunnel currents. Effective work functions of 3.66 eV, 3.73 eV, and 3.74 eV were used for Tip 1, Tip 3, and Tip 5, respectively, while an effective work function of 3.80 eV was used for the HOPG sample.

To determine whether the macroscopic or nanoscopic geometrical features of nanotips have a significant effect on the shape of the THz near-field waveform, we also simulated the THz near field for the tip–sample configuration with nanoscale geometry. A gap width of 1.0 nm and the smallest grid size of 0.5 nm × 0.5 nm× 0.5 nm between the nanotip and the sample were used in the calculation. Although the gap width and the grid size of the nanoscale simulations differed by four orders of magnitude from those of the macroscale simulations, the THz near-field waveforms were almost identical (see Figure 5.9). This result indicates that the waveform of the THz near field is affected by the wavelength-scale feature of nanotips, rather than the nanoscale

geometrical configuration. We also note that the difference of the gap width only affects the field enhancement of the near field. In the case of the 1 nm gap, the enhancement factor of the peak THz electric field reaches 71,000, which is in good agreement with the experimental results, as shown in Figure 5.5b. On the other hand, in the case of the 10 μm gap, the field enhancement factor is significantly reduced to 8.6.

Our results demonstrate that although the electron transfer occurs on the nanoscale via a tunnel junction, the spatiotemporal behavior of this transfer is determined by the overall shape of the nanotip. This behavior results from the relatively long wavelength of the THz electric field. In actual experiments, control of the tip shape—tip height, curvature, and symmetry—is very difficult. Therefore, determining the CEP of a THz near field from the actual tip shape prior to the THz-STM experiment (for example, see Figure 5.4, parts b and c) is impossible. However, our scheme for THz-STM with a CEP shifter enables in-situ tailoring of the CEP-controlled single-cycle THz near field with subcycle resolution. This prescription for retrieving the THz near field in a tunnel junction holds significant promise for unprecedented control of electrons in ultrafast atomic-scale electronics and metrology.

Finally, we discuss the difference between scattering-type near-field scanning optical microscopy (s-NSOM) and our CEP-controlled THz-STM, based on their respective operating principles: s-NSOM measures a local electric field
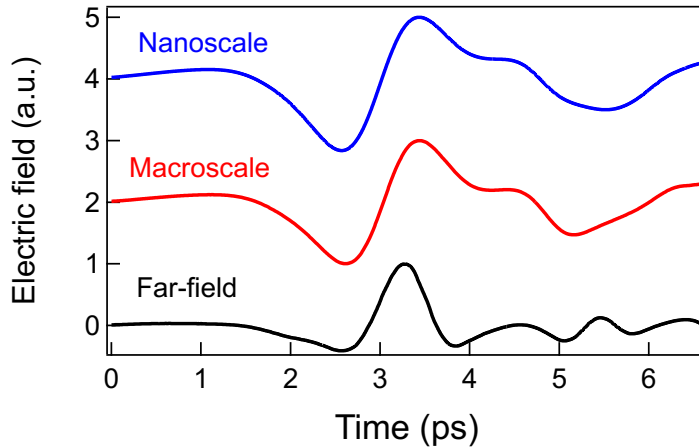

Figure 5.8 | Comparison of macroscale and nanoscale simulations. The Lorentzian tip height in each case is 0.3 mm. Macroscale and nanoscale simulations are performed with a gap width of 1.0 nm and 10 μm, respectively. For clarity, each waveform was normalized at the maximum peak electric field and offset by 2.

underneath the nanotip, whereas THz-STM measures a tunnel current at a tunnel junction. In the case of s-NSOM [38–43], the near-field signal is extracted from a relatively high far-field background by nanotip tapping and higher harmonic demodulations. In contrast, our CEP-controlled THz-STM can retrieve a near-field waveform via subcycle electron tunneling spectroscopy without isolation of the near field from its far field, because of a large enhancement factor of the near field in a tunnel junction ($\sim$100,000) [20,22,44]. On the basis of these operating principles, the spatial resolution of THz-STM is much higher than that of s-NSOM. The spatial resolution of s-NSOM is of the order of 10 nm [40,41], while that of our THz-STM is around 1–2 nm even under ambient laboratory conditions [45], which can be further reduced to 0.06 nm by using low-temperature and ultrahigh-vacuum STM [21]. However, THz-STM does have two limitations. First, the sample surface should be electrically conductive, otherwise we cannot measure the tunnel current. Second, the *I–V* curve in the junction should exhibit nonlinear behavior with respect to the THz electric field, because the operation of THz-STM relies on a nonlinear rectification process in the junction [20,32].

5.5   Summary and outlook

In summary, we have demonstrated the characterization and active control of THz near fields in a tunnel junction by precisely adjusting the CEP of a single-cycle THz electric field. Measurements of the CEP-resolved subcycle tunneling dynamics revealed a large CEP shift between single-cycle THz far and near fields. Based on the antenna model that assigns an equivalent RLC circuit to the nanotip, we could precisely retrieve the THz near field, regardless of the shape of the nanotips. Using a finite integration simulation, we found that the CEP shift is determined by the wavelength-scale features of the tip–sample configuration. Use of the active-controlled double pulses enabled coherent control of the electron transfer in the junction on the femtosecond time scale. Moreover, we could create a desirable near field in the junction, even if the CEP shift between far and near fields resulting from the tip–sample configuration was unpredictable. Our method is applicable to the THz spectral range and considerably higher-frequency ranges, such as the visible range [46,47]. In these higher-frequency ranges, we expect a higher sensitivity of the near-field waveform for smaller geometrical shapes of the nanotips (than for

larger shapes). In addition, the dispersion of the dielectric function and the penetration depth into the junction are expected to be non-negligible. The use of artificially made structures for investigating the adiabatic focusing of surface plasmons would also be interesting [48,49]. We believe that the concept presented here facilitates the development of strong-field physics and next-generation ultrafast atomic-scale electronics and metrology, which will be the building blocks of information technology in the future.

References in chapter 5

[1] A. Schiffrin, T. Paasch-Colberg, N. Karpowicz, V. Apalkov, D. Gerster, S. Mühlbrandt, M. Korbman, J. Reichert, M. Schultze, S. Holzner, J. V Barth, R. Kienberger, R. Ernstorfer, V.S. Yakovlev, M.I. Stockman, F. Krausz, Optical-field-induced current in dielectrics, Nature. 493 (2012) 70–74.

[2] T. Higuchi, C. Heide, K. Ullmann, H.B. Weber, P. Hommelhoff, Light-field-driven currents in graphene, Nature. 550 (2017) 224–228.

[3] A. Baltuška, T. Udem, M. Uiberacker, M. Hentschel, E. Goulielmakis, C. Gohle, R. Holzwarth, V.S. Yakovlev, A. Scrinzi, T.W. Hänsch, F. Krausz, Attosecond control of electronic processes by intense light fields, Nature. 421 (2003) 611–615.

[4] M.F. Kling, Control of Electron Localization in Molecular Dissociation, Science. 312 (2006) 246–248.

[5] M. Kübel, R. Siemering, C. Burger, N.G. Kling, H. Li, A.S. Alnaser, B. Bergues, S. Zherebtsov, A.M. Azzeer, I. Ben-Itzhak, R. Moshammer, R. de Vivie-Riedle, M.F. Kling, Steering Proton Migration in Hydrocarbons Using Intense Few-Cycle Laser Fields, Phys. Rev. Lett. 116 (2016) 193001.

[6] M. Schultze, E.M. Bothschafter, A. Sommer, S. Holzner, W. Schweinberger, M. Fiess, M. Hofstetter, R. Kienberger, V. Apalkov, V.S. Yakovlev, M.I. Stockman, F. Krausz, Controlling dielectrics with the electric field of light., Nature. 493 (2013) 75–8.

[7] T.T. Luu, M. Garg, S.Y. Kruchinin, A. Moulet, M.T. Hassan, E. Goulielmakis, Extreme ultraviolet high-harmonic spectroscopy of solids, Nature. 521 (2015) 498–502.

[8] M. Hohenleutner, F. Langer, O. Schubert, M. Knorr, U. Huttner, S.W. Koch, M. Kira, R. Huber, Real-time observation of interfering crystal electrons in high-harmonic generation, Nature. 523 (2015) 572–575.

[9] F. Langer, M. Hohenleutner, C.P. Schmid, C. Poellmann, P. Nagler, T. Korn, C. Schüller, M.S. Sherwin, U. Huttner, J.T. Steiner, S.W. Koch, M. Kira, R. Huber, Lightwave-driven quasiparticle collisions on a subcycle timescale, Nature. 533 (2016) 225–229.

[10] M. Krüger, M. Schenk, P. Hommelhoff, Attosecond control of electrons emitted from a nanoscale metal tip., Nature. 475 (2011) 78–81.

[11] B. Piglosiewicz, S. Schmidt, D.J. Park, J. Vogelsang, P. Groß, C. Manzoni, P. Farinello, G. Cerullo, C. Lienau, Carrier-envelope phase effects on the strong-field photoemission of electrons from metallic nanostructures, Nat. Photonics. 8 (2014) 37–42.

[12] S. Zherebtsov, T. Fennel, J. Plenge, E. Antonsson, I. Znakovskaya, A. Wirth, O. Herrwerth, F. Süßmann, C. Peltz, I. Ahmad, S.A. Trushin, V. Pervak, S. Karsch, M.J.J. Vrakking, B. Langer, C. Graf, M.I. Stockman, F. Krausz, E. Rühl, M.F. Kling, Controlled near-field enhanced electron acceleration from dielectric nanospheres with intense few-cycle laser fields, Nat. Phys. 7 (2011) 656–662.

[13] F. Süßmann, L. Seiffert, S. Zherebtsov, V. Mondes, J. Stierle, M. Arbeiter, J. Plenge, P. Rupp, C. Peltz, A. Kessel, S. A. Trushin, B. Ahn, D. Kim, C. Graf, E. Rühl, M.F. Kling, T. Fennel, Field propagation-induced directionality of carrier-envelope phase-controlled photoemission from nanospheres, Nat. Commun. 6 (2015) 7944.

[14] G. Herink, D.R. Solli, M. Gulde, C. Ropers, Field-driven photoemission from nanostructures quenches the quiver motion., Nature. 483 (2012) 190–3.

[15] L. Wimmer, G. Herink, D.R. Solli, S.V. Yalunin, K.E. Echternkamp, C. Ropers, Terahertz control of nanotip photoemission, Nat. Phys. 10 (2014) 432–436.

[16] B. Förg, J. Schötz, F. Süßmann, M. Förster, M. Krüger, B. Ahn, W.A. Okell, K. Wintersperger, S. Zherebtsov, A. Guggenmos, V. Pervak, A. Kessel, S.A. Trushin, A.M. Azzeer, M.I. Stockman, D. Kim, F. Krausz, P. Hommelhoff, M.F. Kling, Attosecond nanoscale near-field sampling, Nat. Commun. 7 (2016) 11717.

[17] D. Hoff, M. Krüger, L. Maisenbacher, A.M. Sayler, G.G. Paulus, P. Hommelhoff, Tracing the phase of focused broadband laser pulses, Nat. Phys. 13 (2017) 947–951.

[18] G. Vampa, B.G. Ghamsari, S. Siadat Mousavi, T.J. Hammond, A. Olivieri, E. Lisicka-Skrek, A.Y. Naumov, D.M. Villeneuve, A. Staudte, P. Berini, P.B. Corkum, Plasmon-enhanced high-harmonic generation from silicon, Nat. Phys. 13 (2017) 659–662.

[19] T. Rybka, M. Ludwig, M.F. Schmalz, V. Knittel, D. Brida, A. Leitenstorfer, Sub-cycle optical phase control of nanotunnelling in the single-electron regime, Nat. Photonics. 10 (2016) 667–670.

[20] K. Yoshioka, I. Katayama, Y. Minami, M. Kitajima, S. Yoshida, H. Shigekawa, J. Takeda, Real-space coherent manipulation of electrons in a single tunnel junction by single-cycle terahertz electric fields, Nat. Photonics. 10 (2016) 762–765.

[21] T.L. Cocker, D. Peller, P. Yu, J. Repp, R. Huber, Tracking the ultrafast motion of a single molecule by femtosecond orbital imaging, Nature. 539 (2016) 263–267.

[22] V. Jelic, K. Iwaszczuk, P.H. Nguyen, C. Rathje, G.J. Hornig, H.M. Sharum, J.R. Hoffman, M.R. Freeman, F.A. Hegmann, Ultrafast terahertz control of extreme tunnel currents through single atoms on a silicon surface, Nat. Phys. 13 (2017) 591–598.

[23] T. Hanaguri, S. Niitaka, K. Kuroki, H. Takagi, Unconventional s-Wave Superconductivity in Fe(Se,Te), Science. 328 (2010) 474–476.

[24] A. Wachowiak, Direct Observation of Internal Spin Structure of Magnetic Vortex Cores, Science. 298 (2002) 577–580.

[25] L. Tapasztó, G. Dobrik, P. Lambin, L.P. Biró, Tailoring the atomic structure of graphene nanoribbons by scanning tunnelling microscope lithography, Nat. Nanotechnol. 3 (2008) 397–401.

[26] M. Liu, H.Y. Hwang, H. Tao, A.C. Strikwerda, K. Fan, G.R. Keiser, A.J. Sternbach, K.G. West, S. Kittiwatanakul, J. Lu, S.A. Wolf, F.G. Omenetto, X. Zhang, K.A. Nelson, R.D. Averitt, Terahertz-field-induced insulator-to-metal transition in vanadium dioxide metamaterial, Nature. 487 (2012) 345–348.

[27] P. Zalden, M.J. Shu, F. Chen, X. Wu, Y. Zhu, H. Wen, S. Johnston, Z.-X. Shen, P. Landreman, M. Brongersma, S.W. Fong, H.-S.P. Wong, M. Sher, P. Jost, M. Kaes, M. Salinga, A. von Hoegen, M. Wuttig, A.M. Lindenberg, Picosecond Electric-Field-Induced Threshold Switching in Phase-Change Materials, Phys. Rev. Lett. 117 (2016) 067601.

[28] T. Kubacka, J.A. Johnson, M.C. Hoffmann, C. Vicario, S. de Jong, P. Beaud, S. Grubel, S.-W. Huang, L. Huber, L. Patthey, Y.-D. Chuang, J.J. Turner, G.L. Dakovski, W.-S. Lee, M.P. Minitti, W. Schlotter, R.G. Moore, C.P. Hauri, S.M. Koohpayeh, V. Scagnoli, G. Ingold, S.L. Johnson, U. Staub, Large-Amplitude Spin Dynamics Driven by a THz Pulse in Resonance with an Electromagnon, Science. 343 (2014) 1333–1336.

[29] J.L. LaRue, T. Katayama, A. Lindenberg, A.S. Fisher, H. Öström, A. Nilsson, H. Ogasawara, THz-Pulse-Induced Selective Catalytic CO Oxidation on Ru, Phys. Rev. Lett. 115 (2015) 036103.

[30] J. Itatani, F. Quéré, G.L. Yudin, M.Y. Ivanov, F. Krausz, P.B. Corkum, Attosecond Streak Camera, Phys. Rev. Lett. 88 (2002) 173903.

[31] R. Kienberger, E. Goulielmakis, M. Uiberacker, A. Baltuska, V. Yakovlev, F. Bammer, A. Scrinzi, T. Westerwalbesloh, U. Kleineberg, U. Heinzmann, M. Drescher, F. Krausz, Atomic transient recorder, Nature. 427 (2004) 817–821.

[32] T.L. Cocker, V. Jelic, M. Gupta, S.J. Molesky, J.A.J. Burgess, G.D.L. Reyes, L.V. Titova, Y.Y. Tsui, M.R. Freeman, F.A. Hegmann, An ultrafast terahertz scanning tunnelling microscope, Nat. Photonics. 7 (2013) 620–625.

[33] Y. Kawada, T. Yasuda, H. Takahashi, Carrier envelope phase shifter for broadband terahertz pulses, Opt. Lett. 41 (2016) 986.

[34] H. Hirori, A. Doi, F. Blanchard, K. Tanaka, Single-cycle terahertz pulses with amplitudes exceeding 1 MV/cm generated by optical rectification in LiNbO$_3$, Appl. Phys. Lett. 98 (2011) 091106.

[35] Y. Kawada, T. Yasuda, A. Nakanishi, K. Akiyama, K. Hakamata, H. Takahashi, Achromatic prism-type wave plate for broadband terahertz pulses, Opt. Lett. 39 (2014) 2794.

[36] M. Reid, R. Fedosejevs, Quantitative comparison of terahertz emission from (100) InAs surfaces and a GaAs large-aperture photoconductive switch at high fluences., Appl. Opt. 44 (2005) 149–153.

[37] J.G. Simmons, Generalized Formula for the Electric Tunnel Effect between Similar Electrodes Separated by a Thin Insulating Film, J. Appl. Phys. 34 (1963) 1793–1803.

[38] K. Wang, D.M. Mittleman, N.C.J. van der Valk, P.C.M. Planken, Antenna effects in terahertz apertureless near-field optical microscopy, Appl. Phys. Lett. 85 (2004) 2715.

[39] H.-T. Chen, S. Kraatz, G.C. Cho, R. Kersting, Identification of a Resonant Imaging Process in Apertureless Near-Field Microscopy, Phys. Rev. Lett. 93 (2004) 267401.

[40] J.M. Atkin, S. Berweger, A.C. Jones, M.B. Raschke, Nano-optical imaging and spectroscopy of order, phases, and domains in complex solids, Adv. Phys. 61 (2012) 745–842.

[41] M. Eisele, T.L. Cocker, M.A. Huber, M. Plankl, L. Viti, D. Ercolani, L. Sorba, M.S. Vitiello, R. Huber, Ultrafast multi-terahertz nano-spectroscopy with sub-cycle temporal resolution, Nat. Photonics. 8 (2014) 841–845.

[42] G.X. Ni, L. Wang, M.D. Goldflam, M. Wagner, Z. Fei, A.S. McLeod, M.K. Liu, F. Keilmann, B. Özyilmaz, A.H. Castro Neto, J. Hone, M.M. Fogler, D.N. Basov, Ultrafast optical switching of infrared plasmon polaritons in high-mobility graphene, Nat. Photonics. 10 (2016) 244–247.

[43] G.X. Ni, A.S. McLeod, Z. Sun, L. Wang, L. Xiong, K.W. Post, S.S. Sunku, B.Y. Jiang, J. Hone, C.R. Dean, M.M. Fogler, D.N. Basov, Fundamental limits to graphene plasmonics, Nature. 557 (2018) 530–533.

[44] K. Yoshida, K. Shibata, K. Hirakawa, Terahertz Field Enhancement and Photon-Assisted Tunneling in Single-Molecule Transistors, Phys. Rev. Lett. 115 (2015) 138302.

[45] J. Takeda, K. Yoshioka, Y. Minami, I. Katayama, Nanoscale electron manipulation in metals with intense THz electric fields, J. Phys. D. Appl. Phys. 51 (2018) 103001.

[46] K.J. Savage, M.M. Hawkeye, R. Esteban, A.G. Borisov, J. Aizpurua, J.J. Baumberg, Revealing the quantum regime in tunnelling plasmonics., Nature. 491 (2012) 574–7.

[47] J.A. Scholl, A. García-Etxarri, A.L. Koh, J.A. Dionne, Observation of Quantum Tunneling between Two Plasmonic Nanoparticles, Nano Lett. 13 (2013) 564–569.

[48] M. Stockman, Nanofocusing of Optical Energy in Tapered Plasmonic Waveguides, Phys. Rev. Lett. 93 (2004) 137404.

[49] A. Giugni, B. Torre, A. Toma, M. Francardi, M. Malerba, A. Alabastri, R. Proietti Zaccaria, M.I. Stockman, E. Di Fabrizio, Hot-electron nanoscopy using adiabatic compression of surface plasmons, Nat. Nanotechnol. 8 (2013) 845–852.

Chapter 6

Concluding Remarks

Summary of experimental results

The work presented in this thesis focuses on the ultrafast coherent control of electron tunneling in metallic nanostructures for the development of lightwave nanoelectronics. Carrier-envelope phase-controlled single-cycle intense THz pulses have been exploited to drive real-space electron tunneling in randomly distributed nanogaps of ultrathin Au film and a single tunnel junction of the scanning tunneling microscope.

  As a first step, the nonlinear response of localized electrons in percolated Au nanostructures have been investigated using THz time-domain spectroscopy [1]. We fabricate both isolated and percolated Au nanostructures on Si substrates by changing the average thickness of ultrathin Au films. By increasing the THz electric field strength, large opacity in the THz transmission occurs in the percolated nanostructures: the maximum THz-field-induced transmittance difference, more than 50%, is reached just above the percolation threshold thickness. The observed nonlinear response is due to the nonlinear increase in conductivity of Au films induced by THz-field-driven electron tunneling between Au nanostructures across nanoscale insulating bridges. Although the bulk metal acts as a perfect mirror against the THz electromagnetic field, application of intense single-cycle THz pulses to metallic nanostructures has been shown to be useful for ultrafast

lightwave control of electrons on a nanoscale.

In another set of experiments, we developed THz-STM to directly measure THz-field-driven electron tunneling by employing STM as a single tunnel junction [2]. By tuning the CEP of THz pulses to values of 0, $\pi/2$ and π via the Gouy phase shift using a lens pair, the direction of electron tunneling through a tunnel junction was coherently controlled either from a nanotip to a sample or vice versa. By analyzing the experimental data using the Simmons model, we found that this CEP-dependent ultrafast motion of electrons arises from the sub-cycle asymmetric modulation of a potential barrier in the junction. The large THz field enhancement factor of ~100,000 in the junction enables a large number of electrons to be steered in an extremely nonlinear regime, which is not possible using a conventional STM. Furthermore, because of spatial confinement of THz pulses and nonlinearity of electron tunneling, we succeeded in nanoscale imaging of the Au nanoisland on the HOPG substrate [3] which is far beyond the diffraction limit of THz pulses (i.e., a few hundred micrometers).

The last part of the thesis presents a novel method for characterizing and tailoring a THz near-field in a single tunnel junction [4]. The CEP of single-cycle THz pulse is precisely tuned to the desired value using the THz CEP shifter [5]. Measurements of the phase-resolved sub-cycle electron tunneling dynamics revealed an unexpected large CEP shift of up to $\pi/2$ between far-field and near-field single-cycle THz waveforms. With the aid of electromagnetic simulation, we found that the observed CEP shift stems from the wavelength-scale macroscopic features of the tip–sample configuration because of the antenna response. Given that accurate knowledge and control of the waveform are required for a detailed understanding of lightwave-driven phenomena, we believe this work will lead to techniques that will be the basis for ultrafast atomic-scale electronics and metrologies [6,7]. Furthermore, the double-pulse scheme with tailor-made THz near-fields will provide a unique capability for future subcycle time-resolved experiments by selectively accessing specific energy levels.

Spatial and temporal resolution

We now summarize the potential consequences of our results. By developing THz-STM, manipulation of an electrical current with simultaneous sub-picosecond (<500 fs) temporal resolution and nanometer (<2 nm) spatial

resolution becomes possible. This novel technique makes it possible to access the ultrafast and ultrasmall regime, beyond that which is possible with the latest microprocessor technology, which is currently limited to sub-nanosecond operation with circuit features around 10 nanometers [8]. Therefore, THz-STM is expected to be highly beneficial for exploring future innovations in ultrafast nanoelectronics.

The time resolution can be further improved by employing phase-locked single-cycle pulses with shorter wavelength such as mid-infrared [9,10] and near-infrared [11]. In this case, the time resolution is expected to reach a few femtoseconds. We foresee that the application of short wavelength pulses will require sophisticated modulation techniques for lock-in detection, in order to avoid thermal expansion of the nanotip caused by the large photon energy. Suitable techniques might include delay time modulation such as shaken-pulse-pair-excited STM [12,13], or CEP modulation to extract the CEP-dependent current from the background signal [14,15]. Ultimately, the time resolution will be limited by the transition from the lightwave-driven regime to the multiphoton regime [16].

On the other hand, the spatial resolution can be improved to the atomic scale using ultrahigh-vacuum STM [6,7]. Recently, ultrafast imaging of a single molecule with spatial resolution of 0.06 nm was achieved using low-temperature and ultrahigh-vacuum STM [6].

Perspectives

Our phase-controlled THz-STM enables atomically strong single-cycle THz pulses with desired waveform to be focused on a nanoscale. Therefore, spatiotemporal manipulation of ultrafast nonlinear processes is expected in a variety of systems [17]. One of the more interesting possibilities is ultrafast and ultradense information storage, by exploiting phase-change chalcogenide alloys $Ge_2Sb_2Te_5$ [18,19], which is widely used in optical recording media and phase-change random access memory.

Filming an ultrafast non-equilibrium process with atomic resolution is highly beneficial to understanding the underlying mechanism of that process. In particular, photoinduced phase transitions have long been studied in condensed matter systems, but many details still remain to be clarified [20]. Tracking the amplitude and phase dynamics of electronic structures in real space will be a powerful technique for revealing the physics of those structures,

something that is not possible with conventional ultrafast spectroscopies.

Furthermore, sophisticated techniques demonstrated in conventional STM, such as scanning tunneling spectroscopy, spin-polarized STM [21,22], STM light emission spectroscopy [23,24], and quasi-particle interference [25,26], can be incorporated into THz-STM. Such techniques will require laser sources with a high repetition rate in order to greatly improve the signal-to-noise ratio and measurement efficiency.

From a more unified point of view, using THz-STM, electrons can be injected into and extracted from a specific electronic state of the sample in a space-selective, time-selective, and energy-selective manner. Because of this unique capability, THz-STM will become an indispensable spectroscopic tool for material and optical science in the future. We believe that the concept of "lightwave nanoelectronics" presented in this thesis paves the way for the development of next-generation ultrafast atomic-scale electronics and metrology, which are the building blocks of future information technology.

References in chapter 6

[1] K. Yoshioka, Y. Minami, K. Shudo, T.D. Dao, T. Nagao, M. Kitajima, J. Takeda, I. Katayama, Terahertz-Field-Induced Nonlinear Electron Delocalization in Au Nanostructures, Nano Lett. 15 (2015) 1036–1040.

[2] K. Yoshioka, I. Katayama, Y. Minami, M. Kitajima, S. Yoshida, H. Shigekawa, J. Takeda, Real-space coherent manipulation of electrons in a single tunnel junction by single-cycle terahertz electric fields, Nat. Photonics. 10 (2016) 762–765.

[3] J. Takeda, K. Yoshioka, Y. Minami, I. Katayama, Nanoscale electron manipulation in metals with intense THz electric fields, J. Phys. D. Appl. Phys. 51 (2018) 103001.

[4] K. Yoshioka, I. Katayama, Y. Arashida, A. Ban, Y. Kawada, K. Konishi, H. Takahashi, J. Takeda, Tailoring Single-Cycle Near Field in a Tunnel Junction with Carrier-Envelope Phase-Controlled Terahertz Electric Fields, Nano Lett. 18 (2018) 5198–5204.

[5] Y. Kawada, T. Yasuda, H. Takahashi, Carrier envelope phase shifter for broadband terahertz pulses, Opt. Lett. 41 (2016) 986.

[6] T.L. Cocker, D. Peller, P. Yu, J. Repp, R. Huber, Tracking the ultrafast motion of a single molecule by femtosecond orbital imaging, Nature. 539 (2016) 263–267.

[7] V. Jelic, K. Iwaszczuk, P.H. Nguyen, C. Rathje, G.J. Hornig, H.M. Sharum, J.R. Hoffman, M.R. Freeman, F.A. Hegmann, Ultrafast terahertz control of extreme tunnel currents through single atoms on a silicon surface, Nat. Phys. 13 (2017) 591–598.

[8] M.M. Waldrop, The chips are down for Moore's law, Nature. 530 (2016) 144–147.

[9] C. Kübler, R. Huber, S. Tübel, A. Leitenstorfer, Ultrabroadband detection of multi-terahertz field transients with GaSe electro-optic sensors: Approaching the near infrared, Appl. Phys. Lett. 85 (2004) 3360–3362.

[10]   F. Junginger, A. Sell, O. Schubert, B. Mayer, D. Brida, M. Marangoni, G. Cerullo, A. Leitenstorfer, R. Huber, Single-cycle multiterahertz transients with peak fields above 10 MV/cm., Opt. Lett. 35 (2010) 2645–7.

[11]   G. Krauss, S. Lohss, T. Hanke, A. Sell, S. Eggert, R. Huber, A. Leitenstorfer, Synthesis of a single cycle of light with compact erbium-doped fibre technology, Nat. Photonics. 4 (2010) 33–36.

[12]   Y. Terada, S. Yoshida, O. Takeuchi, H. Shigekawa, Real-space imaging of transient carrier dynamics by nanoscale pump–probe microscopy, Nat. Photonics. 4 (2010) 869–874.

[13]   S. Yoshida, Y. Aizawa, Z.-H. Wang, R. Oshima, Y. Mera, E. Matsuyama, H. Oigawa, O. Takeuchi, H. Shigekawa, Probing ultrafast spin dynamics with optical pump-probe scanning tunnelling microscopy., Nat. Nanotechnol. 9 (2014) 588–593.

[14]   T. Paasch-Colberg, A. Schiffrin, N. Karpowicz, S. Kruchinin, Ö. Sağlam, S. Keiber, O. Razskazovskaya, S. Mühlbrandt, A. Alnaser, M. Kübel, V. Apalkov, D. Gerster, J. Reichert, T. Wittmann, J. V Barth, M.I. Stockman, R. Ernstorfer, V.S. Yakovlev, R. Kienberger, F. Krausz, Solid-state light-phase detector, Nat. Photonics. 8 (2014) 214–218.

[15]   T. Higuchi, C. Heide, K. Ullmann, H.B. Weber, P. Hommelhoff, Light-field-driven currents in graphene, Nature. 550 (2017) 224–228.

[16]   G. Herink, L. Wimmer, C. Ropers, Field emission at terahertz frequencies: AC-tunneling and ultrafast carrier dynamics, New J. Phys. 16 (2014) 123005.

[17]   T. Kampfrath, K. Tanaka, K.A. Nelson, Resonant and nonresonant control over matter and light by intense terahertz transients, Nat. Photonics. 7 (2013) 680–690.

[18]   J. Takeda, W. Oba, Y. Minami, T. Saiki, I. Katayama, Ultrafast crystalline-to-amorphous phase transition in Ge2Sb2Te5 chalcogenide alloy thin film using single-shot imaging spectroscopy, Appl. Phys. Lett. 104 (2014) 261903.

[19]   Y. Sanari, T. Tachizaki, Y. Saito, K. Makino, P. Fons, A. V. Kolobov, J. Tominaga, K. Tanaka, Y. Kanemitsu, M. Hase, H. Hirori, Zener Tunneling Breakdown in Phase-Change Materials Revealed by Intense Terahertz Pulses, Phys. Rev. Lett. 121 (2018) 165702.

[20] K. Nasu, Photoinduced phase transitions, World Scientific, 2004.

[21] R. Wiesendanger, H.J. Gntherodt, G. Gntherodt, R.J. Gambino, R. Ruf, Observation of vacuum tunneling of spin-polarized electrons with the scanning tunneling microscope, Phys. Rev. Lett. 65 (1990) 247–250.

[22] P. Hsu, A. Kubetzka, A. Finco, N. Romming, K. von Bergmann, R. Wiesendanger, Electric-field-driven switching of individual magnetic skyrmions, Nat. Nanotechnol. (2016) 1–11.

[23] Y. Zhang, Y. Luo, Y. Zhang, Y.-J. Yu, Y.-M. Kuang, L. Zhang, Q.-S. Meng, Y. Luo, J.-L. Yang, Z.-C. Dong, J.G. Hou, Visualizing coherent intermolecular dipole–dipole coupling in real space, Nature. 531 (2016) 623–627.

[24] H. Imada, K. Miwa, M. Imai-Imada, S. Kawahara, K. Kimura, Y. Kim, Real-space investigation of energy transfer in heterogeneous molecular dimers, Nature. 538 (2016) 364–367.

[25] Y. Hasegawa, P. Avouris, Direct observation of standing wave formation at surface steps using scanning tunneling spectroscopy, Phys. Rev. Lett. 71 (1993) 1071–1074.

[26] T. Hanaguri, S. Niitaka, K. Kuroki, H. Takagi, Unconventional s-Wave Superconductivity in Fe(Se,Te), Science. 328 (2010) 474–476.

List of Publications

Publications within this thesis

[1] <u>Katsumasa Yoshioka</u>, Yasuo Minami, Ken-ichi Shudo, Thang D. Dao, Tadaaki Nagao, Masahiro Kitajima, Jun Takeda, and Ikufumi Katayama, "Terahertz-Field-Induced Nonlinear Electron Delocalization in Au Nanostructures",
Nano Letters **15**, 1036-1040 (2015).

[2] <u>Katsumasa Yoshioka</u>, Ikufumi Katayama, Yasuo Minami, Masahiro Kitajima, Shoji Yoshida, Hidemi Shigekawa, and Jun Takeda, "Real-space coherent manipulation of electrons in a single tunnel junction by single-cycle terahertz electric fields",
Nature Photonics **10**, 762–765 (2016).

[3] Jun Takeda, <u>Katsumasa Yoshioka</u>, Yasuo Minami, and Ikufumi Katayama,
"Nanoscale electron manipulation in metals with intense THz electric fields",
Journal of Physics D: Applied Physics **51**, 103001 (2018).

[4] <u>Katsumasa Yoshioka</u>, Ikufumi Katayama, Yusuke Arashida, Atsuhiko Ban, Yoichi Kawada, Kuniaki Konishi, Hironori Takahashi, and Jun Takeda,
"Tailoring single-cycle near field in a tunnel junction with carrier-envelope phase-controlled terahertz electric fields",
Nano Letters **18**, 5198–5204 (2018).

Publications concerning other topics

[5] Xinwei Li, Motoaki Bamba, Qi Zhang, Saeed Fallahi, Geoff C. Gardner, Weilu Gao, Minhan Lou, <u>Katsumasa Yoshioka</u>, Michael J. Manfra, and Junichiro Kono
"Vacuum Bloch-Siegert Shift in Landau Polaritons with Ultrahigh Cooperativity",
Nature Photonics **12**, 324–329 (2018).

[6] Yoichi Kawada, <u>Katsumasa Yoshioka</u>, Yusuke Arashida, Ikufumi Katayama, Jun Takeda, and Hironori Takahashi,
"Simultaneous acquisition of complex transmittance and birefringence with two counter-rotating circularly polarized THz pulses",
Optics Express **26**, 30420-30434 (2018).

[7] Shoji Yoshida, Hideki Hirori, Takehiro Tachizaki, <u>Katsumasa Yoshioka</u>, Yusuke Arashida, Zi-Han Wang, Yasuyuki Sanari, Osamu Takeuchi, Yoshihiko Kanemitsu, and Hidemi Shigekawa,
"Sub-cycle transient scanning tunneling spectroscopy with visualization of enhanced terahertz near-field",
submitted

[8] <u>Katsumasa Yoshioka</u>, Ippo Igarashi, Shoji Yoshida, Yusuke Arashida, Ikufumi Katayama, Jun Takeda, and Hidemi Shigekawa,
"Generation of sub-cycle mid-infrared coherent transients and field enhancement in a tunnel junction",
in preparation

Presentations at international conference

[1] "Nonlinear Response of Au Nanostructures Observed with Intense THz Pulses", 39th International Conference on Infrared and Millimeter and Terahertz Waves (IRMMW-THz 2014), Paper T5-P16.4, Tucson, USA, Sep. 2014. (Poster and Oral presentation), **Best Student Paper/Presentation Award (2nd place)**

[2] "Real-Space Control of the Electron Transfer in a Tunnel Junction with Single-Cycle THz Electric Field", Ultrafast Dynamics at the Nanoscale 2016, Okinawa, July. 2016. (Oral presentation)

[3] "Coherent Control of the Motion of Electrons in a Tunnel Junction via Single-Cycle THz Electric Field", 41th International Conference on Infrared and Millimeter and Terahertz Waves (IRMMW-THz 2016), Copenhagen, Denmark, Sep. 2016. (Oral presentation)

[4] "Ultrafast Manipulation of Electron Transfer in a Tunnel Junction using Carrier-Envelope Phase Controlled THz-STM", 24th International Colloquium on Scanning Probe Microscopy (ICSPM24), Hawaii, USA, Dec. 2016. (Oral presentation)

[5] "Real-Space Coherent Manipulation of Electrons in a Single Tunnel Junction by Single-Cycle Terahertz Electric Fields", The 2nd international symposium on Recent Trends in Analysis Techniques for Functional Materials and Devices, Osaka, Japan, Jan. 2017. (**Invited talk**)

[6] "Coherent Manipulation of Electrons in a Tunnel Junction with Carrier-Envelope Phase Controlled THz Electric Fields", 2017 Nonlinear Optics (2017 NLO), Hawaii, USA, Jul. 2017 (Oral presentation)

[7] "Sub-cycle THz control of electrons in a tunnel junction with a carrier-envelope phase shifter", 8th International Symposium on Terahertz Nanoscience (TeraNano 8), Okayama, Japan, Nov. 2017 (Oral presentation)

[8] "Sub-cycle control of THz near-field and electrons in a single tunnel junction", Gordon Research Conference and Seminar (GRC/S) Ultrafast Phenomena in Cooperative Systems, Texas, USA, Feb. 2018 (Poster presentation), **Discussion leader in GRS**

[9] "Sub-cycle Manipulation of Electrons in a Tunnel Junction with Phase-controlled Single-cycle THz Near-fields", 21st International Conference on Ultrafast Phenomena (UP2018), Hamburg, Germany, Jul. 2018 (Oral presentation)

[10] "In-situ Tailoring of Single-cycle Near Field in a Tunnel Junction Using Phase-controlled THz-STM", 14th International Conference on Atomically Controlled Surfaces, Interfaces and Nanostructures (ACSIN-14) in conjunction with 26th International Colloquium on Scanning Probe Microscopy (ICSPM26), Sendai, Japan, Nov. 2018 (Oral presentation)